Aix*Marseille université
Socialement engagée

NNT/NL : 2021AIXM0001/001ED352

THÈSE DE DOCTORAT

Soutenue à Aix-Marseille Université
le 30 septembre 2021 par

Md RASEDUJJAMAN

Titre de la thèse :
3D optical microscopy for label free characterization of immunological cells

Discipline
Physique et Sciences de la Matière

Spécialité
Optique, photonique et traitment d'image

École doctorale
ED 352 Physique et Sciences de la Matière

Laboratoire/Partenaires de recherche
Institut Fresnel, équipe S.E.M.O
et Laboratoire adhésion et Inflammation(LAI)

Composition du jury

Arnaud DUBOIS Professeur Université Paris-Saclay	Rapporteur
Françoise ARGOUL Directeur de recherche CNRS Université de Bordeaux	Examinatrice
Olivier HAEBERLÉ Professeur Université de Haute-Alsace	Président du jury
Philippe ROBERT Maitre de conferences Universite d'Aix Marseille	Co-Directeur de thèse
Guillaume MAIRE Maitre de conferences Universite d'Aix Marseille	Directeur de thèse

INSTITUT FRESNEL

LAI

Affidavit

I, undersigned, Md Rasedujjaman, hereby declare that the work presented in this manuscript is my own work, carried out under the scientific direction of Guillaume Maire and co-direction of Philippe Robert, in accordance with the principles of honesty, integrity and responsibility inherent to the research mission. The research work and the writing of this manuscript have been carried out in compliance with both the french national charter for Research Integrity and the Aix-Marseille University charter on the fight against plagiarism.

This work has not been submitted previously either in this country or in another country in the same or in a similar version to any other examination body.

Marseille, October 14, 2021

Résumé

Généralités

L'innovation du microscope optique a révolutionné l'étude de la microbiologie. Le microscope optique conventionnel fournit des images où le contraste est obtenu en raison de la diffusion de la lumière par la distribution de permittivité de l'échantillon. Cependant, ce vaste champ la microscopie optique n'apporte aucune information quantitative sur la permittivité de l'échantillon. En effet, reconstruire une distribution de permittivité 3D à partir de mesures de champs dispersés, c'est-à-dire la résolution du problème de diffusion inverse, nécessite idéalement que l'amplitude et la phase de le champ est connu. La structure de l'objet peut être reconstruite à partir de la dispersion en appliquant l'algorithme de reconstruction approprié. D'un point de vue expérimental, le le champ diffusé contenant à la fois l'amplitude et la phase peut être collecté par une technique appelée Microscopie diffractive tomographique (TDM) dont le principe est basé sur l'holographie numérique microscopie (DHM). La GDT consiste généralement à éclairer l'échantillon de plusieurs différentes directions avec une lumière collimée cohérente et l'enregistrement de l'hologramme numérique qui est formé en raison de l'interférence entre le champ de référence et le champ dispersé par la cible objet. À partir de l'hologramme, l'amplitude et la phase du champ diffusé sont filtrées et est fourni à l'algorithme de reconstruction et donc la reconstruction 3D de l'échantillon est Obtenu.

Jusqu'à présent, seule la TDM en géométrie de transmission a été utilisée, et cette configuration souffre de une résolution axiale médiocre par rapport à la résolution transversale. Dans ce travail, nous présentons au meilleur de nos connaissances pour la première fois la caractérisation de cellules avec TDM en géométrie de réflexion. Cette configuration est plus difficile à mettre en œuvre en raison du niveau inférieur de signal diffusé et de la normalisation de phase plus complexe de l'ensemble de données Obligatoire. Après avoir résolu ces problèmes, nous montrons qu'il fournit la meilleure résolution si le contour la reconstruction des cellules est ciblée. Nous validons expérimentalement cette technique sur différents cellules immunologiques, avec une application potentielle pour détecter des processus importants comme immunologique formation de synapses ou phagocytose.

Quelques mots sur la résolution

Le pouvoir de résolution d'un microscope est défini comme la capacité de distinguer les détails. Dans d'autres, c'est la distance minimale à laquelle deux points distincts

d'un échantillon peuvent encore être considérés comme entités distinctes lorsqu'ils sont observés par la caméra du microscope ou par l'observateur. La résolution du microscope est étroitement liée à l'ouverture numérique (NA). La résolution n'est pas seulement dépendant de l'AN d'un objectif, mais de l'AN de l'ensemble du système, compte tenu de le NA du condensateur du microscope. La résolution est également liée à la longueur d'onde de la lumière qui est utilisée pour imager un spécimen, la lumière de longueurs d'onde plus courtes peut résoudre de plus grands détails que les longueurs d'onde plus longues. Il y a trois concepts mathématiques qui doivent être pris en considération lorsque traitant de la résolution: " Airy Discs ", " Abbe's Diffraction Limit ", et le " Rayleigh Criterion ". Pour la première fois, la limite de diffraction du microscope optique, qui est liée à la résolution du microscope, est formulée par Ernst Abbe et est donnée par

$$d_{lateral} = \frac{\lambda}{2 * NA} \tag{0.1}$$

Une variation de la formule ci-dessus est donnée par

$$d_{lateral} = \frac{1.22\lambda}{2sin(\alpha)} \tag{0.2}$$

où d est la plus petite distance pour laquelle deux objets peuvent être séparés, et α l'angle de collection de l'objectif. Au mieux, $\alpha = \pi/2$, soit un pouvoir de séparation de 0.61λ. Dans le domaine visible pour les microscopes optiques à transmission, la résolution est donc typiquement de 300 nm. Notons que dans le cadre de la microscopie tomographique par diffraction(TDM), il est d'usage de dire que son pouvoir de résolution est largement inférieur au critère de Rayleigh, puisque les objets séparés de quelques dizaines de nanomètres sont discernables. Mais nous étudions des objets qui ne sont plus ponctuels, et qui sont fortement couplés par la distance qui les sépare. Il est alors difficile dans ces conditions de définir un critère de résolution, celui-ci variant en fonction des diffusions multiples entre les objets.

Microscopie diffractive tomographique (TDM)

Théorie du TDM

La théorie de la microscopie tomographique diffractive (TDM) a été proposée pour la première fois et sa formulation mathématique a été dérivée par Emil Wolf. La formulation mathématique a été dérivée par Emil Wolf. Elle repose essentiellement sur la résolution du problème de diffusion de l'équation suivante équation d'onde scalaire.

Avec l'hypothèse du champ scalaire, la propagation du champ électromagnétique, $U(\vec{r})$, ,à travers le milieu de diffusion peut être décrite par l'équation de Helmholtz comme suit:

$$\nabla^2 U(\vec{r}) + k_o^2 n(\vec{r})^2 U(\vec{r}) = 0 \tag{0.3}$$

Le champ électromagnétique peut être vu comme la décomposition de la composante du champ incident $U_o(\vec{r})$ et la composante du champ diffusé $U_s(\vec{r})$, alors nous pouvons écrire:

$$U(\vec{r}) = U_o(\vec{r}) + U_s(\vec{r}) \tag{0.4}$$

Maintenant, si nous considérons $\delta_n(\vec{r}) \neq 0$ dans l'Eq.0.3, le milieu est inhomogène, ce qui signifie qu'il y a des diffusions à l'intérieur du milieu. C'est le cas qui se produit dans la tomographie par diffraction. L'équation de Helmholtz peut maintenant être écrite comme suit

$$(\nabla^2 + k(\vec{r})^2) U(\vec{r}) = 0 \tag{0.5}$$

En utilisant l'équation.0.3, nous pouvons réécrire l'équation.0.5 comme suit

$$(\nabla^2 + k_m^2) U(\vec{r}) = -f(\vec{r}) U(\vec{r}) \tag{0.6}$$

Où $f(\vec{r})$ est appelé potentiel de diffusion ou encore fonction objet.

$$f(\vec{r}) = k_m^2 \left[\left(\frac{n(\vec{r})}{n_m} \right)^2 - 1 \right] \tag{0.7}$$

À l'aide de l'équation.0.4 et de l'équation.0.3, nous pouvons réécrire l'équation.0.6 en termes de composante diffusée U_s.

$$(\nabla^2 + k_m^2) U_s(\vec{r}) = -f(\vec{r}) U(\vec{r}) \tag{0.8}$$

L'équation.0.8 est connue sous le nom d'équation de Helmholtz scalaire pour un milieu inhomogène. En TDM, nous résolvons mathématiquement U_s(ř) et il n'est pas simple de la trouver. Il existe un moyen d'écrire une solution pour $U_s(\vec{r})$ à l'aide de la fonction de Green. La fonction de Green, qui est une solution de l'équation différentielle

$$(\nabla^2 + k_m^2) g(\vec{r} - \vec{r}') = -\delta(\vec{r} - \vec{r}') \tag{0.9}$$

Où $g(\vec{r} - \vec{r}')$ est appelée fonction de Green et dans l'espace libre elle est donnée par

$$g(\vec{r} - \vec{r}') = \frac{exp(i k_m(\vec{r} - \vec{r}'))}{4\pi(\vec{r} - \vec{r}')} \tag{0.10}$$

Lorsque l'opérateur différentiel, $(\nabla^2 + k_m^2)$, est appliqué sur la fonction de Green comme indiqué dans l'eq.0.10, la solution est une fonction delta. Inversement, on peut dire que la fonction de Green est la réponse pour une diffusion en un seul point (c'est-à-dire une fonction delta unique). En imposant le principe de linéarité, il est possible d'écrire la fonction de forçage indiquée à droite de l'équation.0.8 comme une somme d'impulsions.

$$f(\vec{r})U(\vec{r}) = \int f(\vec{r}')U(\vec{r}')\delta(\vec{r} - \vec{r}')d\vec{r}' \tag{0.11}$$

La fonction de Green étant la solution de l'équation d'onde pour une seule fonction delta et le côté gauche de l'équation 0.8 étant linéaire, nous pouvons écrire une solution pourU_s en additionnant le champ diffusé individuel dû au diffuseur ponctuel individuel correspondant. En utilisant cet argument, le champ diffusé dû à la fonction de forçage $f(\vec{r}')U(\check{r}')$ s'écrit comme une somme de versions mises à l'échelle et décalées de la réponse impulsionnelle, $g(\vec{r})$. Ensuite, le champ total diffusé U_s dû à toutes les sources ponctuelles individuelles du côté droit de l'équation.0.8 s'écrit comme suit

$$U_s(\vec{r}) = \int g(\vec{r} - \vec{r}')f(\vec{r}')U(\vec{r}')d\vec{r}' \tag{0.12}$$

L'eq.0.12 est connue sous le nom d'intégrale de convolution. Cette équation semble être la solution pour U_s mais ce n'est pas le cas car sur le côté droit il y a le champ total qui contient à nouveau U_s, c'est-à-dire($U = U_o + U_s$). Par conséquent, nous devons résoudre l'éq.0.12 uniquement pour U_s. Comme la solution analytique n'est pas possible, nous nous appuyons sur des méthodes d'approximation pour trouver la solution. Les deux méthodes d'approximation les plus connues sont l'approximation de Born et l'approximation de Rytov.

A l'aide de l'approximation de Born et en termes de transformée de Fourier, le champ diffusé peut être écrit comme suit

$$U_s(\vec{k}, \vec{k_i}) \propto \tilde{f}(\vec{k} - \vec{k_i}) \tag{0.13}$$

L'équation Eq. 0.13 indique que le champ diffusé en champ lointain le long de la direction de $\vec{k}$ pour un éclairement le long de, $\vec{k_i}$ est proportionnel à la transformée de Fourier de la fonction de l'objet, c'est-à-dire le contraste de permittivité de l'objet. Cette relation est linéaire et constitue la formule la plus importante pour le microscope tomographique à diffraction sous approximation de Born. Pour un objet 2D, le champ diffusé est enregistré par un capteur 1D (c'est-à-dire le long d'une ligne) et les données correspondantes de l'espace k se situent sur un demi-cercle. Mais dans toutes les situations pratiques, l'échantillon est en 3D et le champ diffusé est mesuré par un capteur 2D dans l'espace image. La transformée de Fourier du champ mesuré par le capteur 2D donnerait les valeurs de la transformée 3D de l'objet sur une surface sphérique, la sphère d'Ewald.

Configuration expérimentale

Le schéma du TDM en configuration de réflexion est présenté à la Fig. 0.1. L'architecture de la configuration est basée sur le principe de l'holographie numérique d'axe et est construite par l'assemblage de composants optiques discrets. Les principaux composants sont la source lumineuse, le miroir rotatif, la caméra, les séparateurs de faisceau, l'objectif, la lentille et les miroirs, etc. La source lumineuse est un laser

super-continuum (SuperK Extreme EXW-12, NKT Photonics). Le faisceau de sortie du laser est filtré à 475 nm avec une largeur spectrale de 10 nm en utilisant un filtre passe-bande variable (SuperK vaira, NKT Photonics). Le polariseur linéaire LP polarise linéairement le faisceau et la direction de polarisation est verticale, le long de l'axe y (convention d'axe, encart : table optique, Fig. 0.1). Le faisceau polarisé linéairement est ensuite divisé par le séparateur de faisceau polarisant (PBS) en un faisceau de référence et un faisceau objet qui est dirigé vers l'échantillon. Dans le schéma, le faisceau de référence et le faisceau objet sont représentés dans des couleurs différentes afin de les différencier, mais ils ont tous deux la même longueur d'onde. Le rapport de puissance du faisceau de référence et du faisceau objet dépend de la direction de polarisation du faisceau d'entrée au PBS. La direction de polarisation du faisceau objet est similaire à celle du faisceau d'entrée tandis que le faisceau de référence est polarisé horizontalement.

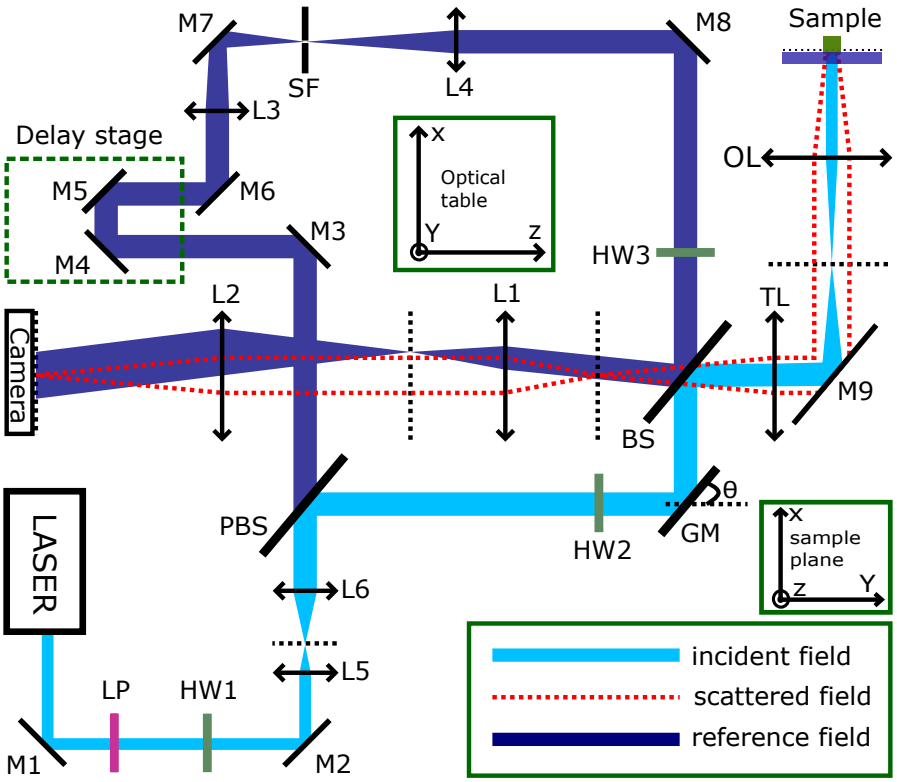

Figure 0.1 – The schematic of the experimental setup: GM, rotating mirror; OL, objective lens; TL, tube lens; L_{1-6}, lens; PBS, polarizing beam splitter; BS, beam splitter; SP, spatial filter; M_{1-9}, steering mirror; LP, linear polarizer; HW_{1-3}, half-wave plate.

Puisque la plaque demi-onde peut faire tourner la direction de polarisation (la rotation de la polarisation est double de celle de la rotation physique de la plaque demi-onde) de la lumière polarisée linéairement, donc selon l'angle de rotation de $HW1$ (monté sur un support de type rotatif), nous pouvons ajuster le rapport

de puissance entre le faisceau objet et le faisceau de référence. La plaque demi-onde $HW2$ située sur le trajet de l'objet permet de choisir la direction de polarisation du faisceau. Mais dans notre expérience, nous gardons $HW2$ le long de l'axe y, ce qui signifie que la direction de polarisation avant et après la plaque demi-onde reste la même. Le miroir de galvano(GM),(FS–300, Newport) permet la déviation du faisceau objet pour illuminer l'échantillon. Le centre du miroir de galvano est conjugué avec l'échantillon à travers la lentille du tube TL et la lentille de l'objectif OL. Par conséquent, en faisant tourner le miroir, on peut faire varier l'angle d'illumination sans déplacer le faisceau latéralement sur l'objet. L'angle polaire de l'illumination peut être modifié sur toute l'ouverture numérique, NA, de l'objectif. Le champ diffusé (ligne pointillée rouge dans le schéma) par l'objectif est collecté par l'objectif (Nikon Apo TIRF, immersion dans l'huile, 100X, NA = 1.49) et est imagé par une sCMOS caméra (Andor Zyla) avec un grossissement global d'environ 200. D'autre part, pour rendre la longueur du chemin optique du faisceau de référence similaire à celle du faisceau objet, une ligne à retard est utilisée (Miroir, $M4$ et $M5$ sont montés sur l'étage à retard). Le filtre spatial SP aide à nettoyer le faisceau de référence. En ajustant le miroir, $M8$, on permet au faisceau de référence d'arriver à la caméra avec un angle de cisaillement. La longueur du chemin optique du faisceau de référence est ajustée de manière à ce que le signal diffusé par l'objet et le faisceau de référence puisse produire des franges d'interférence, ce que nous appelons l'hologramme hors axe, et cet hologramme est enregistré par la caméra. Le rôle de la plaque demi-onde $HW3$ est de rendre la direction de polarisation du faisceau de référence similaire à celle du faisceau objet. Sinon, aucune interférence n'aura lieu entre le faisceau de référence et le faisceau diffusé.

Principes de la microscopie confocale synthétique

Dans la section précédente, nous avons établi (sous l'approximation de Born) le lien entre le champ diffusé mesuré et la fonction objet, c'est-à-dire le contraste de prémitivité en tant que

$$\tilde{\Delta\epsilon}(\vec{k}-\vec{k_i}) \propto U_s(\vec{k},\vec{k_i}) \tag{0.14}$$

où $\tilde{\Delta\epsilon}$ est la transformée de Fourier 3D du contraste de permittivité de l'échantillon (équivalent de la fonction objet). Le contraste de permittivité reconstruit peut être obtenu directement à partir de la transformée de Fourier inverse 3D des données mesurées en champ lointain, à savoir

$$\Delta\epsilon(\vec{r}) = \sum_{\vec{k_i}}\sum_{\vec{k}} U_s(\vec{k},\vec{k_i}) exp(i(\vec{k}-\vec{k_i})\cdot\vec{r}) \tag{0.15}$$

L'équation 0.15 indique que si l'on combine le champ diffusé pour tous les angles d'illumination, on obtient le contraste de permittivité de l'échantillon. Dans TDM, l'échantillon est éclairé par une onde plane incidente avec différents angles d'illumination et les signaux diffusés réfléchis sont collectés. Chaque angle d'illumination permet d'accéder à la détection de différentes régions des fréquences spatiales dans l'espace

k.

En fait, l'équation 0.15 peut également être considérée comme le champ diffusé fourni par un microscope confocal. Lorsque l'idée d'ouverture synthétique est combinée au principe de la microscopie confocale, la modalité d'imagerie résultante est appelée microscopie confocale synthétique (SyCM) ou microscopie confocale à ouverture synthétique 3D. Dans la microscopie confocale conventionnelle, l'échantillon ou le faisceau lui-même est déplacé dans la direction xyz pour balayer l'échantillon point par point. Ces images ponctuelles sont combinées par ordinateur et nous obtenons ainsi une image 3D de l'échantillon avec des détails plus fins. Mais dans notre cas, nous balayons l'angle d'illumination pendant la mesure, ils sont combinés numériquement pour effectuer le balayage de position 3D pendant le processus de reconstruction, ceci est possible parce que dans notre mesure au plan focal nous avons accès à la fois à l'amplitude et à la phase du champ diffusé.

Cette imagerie confocale synthétique est basée sur le fait que la diffusion est un processus linéaire. Le champ diffusé par un échantillon éclairé par un faisceau constitué d'une somme d'ondes planes est égal à la somme des champs diffusés pour chaque onde plane. Par conséquent, en supposant que la phase de toutes les ondes planes incidentes est nulle au point focal de l'objectif, correspondant à l'origine du système de coordonnées, c'est-à-dire $\vec{r} = 0$.

$$\tilde{u}(\vec{k}, \vec{r}) = \sum_{\vec{k_i}} U_s(\vec{k}, \vec{k_i}) exp(-i\vec{k_i} \cdot \vec{r}) \tag{0.16}$$

représente le champ lointain diffusé le long de la direction de $\vec{k}$ telle qu'obtenue alors que l'échantillon est éclairé par un faisceau composé d'ondes planes interférant de manière constructive à $\vec{r}$. Ensuite, le champ dans le domaine de l'image du microscope obtenu à partir du champ lointain $\tilde{u}$ peut être écrit comme suit

$$U(\vec{r}) = \sum_{\vec{k}} \tilde{u}(\vec{k}, \vec{r}) exp(i\vec{k} \cdot \vec{r}) \tag{0.17}$$

Le champ tel qu'indiqué dans l'Eq. eq:measuredFieldatImagePlane correspond au champ complexe qui serait mesuré au centre du trou d'épingle d'un microscope confocal.

En combinant les deux équations ci-dessus, nous pouvons dire que le champ complexe, U est proportionnel au contraste de permittivité sous l'approximation de Born,

$$U(\vec{r}) = \sum_{\vec{k_i}} \sum_{\vec{k}} U_s(\vec{k}, \vec{k_i}) exp(i(\vec{k} - \vec{k_i}) \cdot \vec{r}) \propto \Delta\epsilon(\vec{r}) \tag{0.18}$$

L'équation (0.18) est équivalente à une ouverture synthétique 3D pour obtenir les cartes d'indice de réfraction et d'absorption des échantillons. En fait, le calcul de son intensité et de sa phase est également significatif, car ils représentent le module au carré et l'argument de la réflectance (ou de la transmittance) d'un faisceau focalisé balayant l'échantillon. De plus, cette approche offre une certaine flexibilité pour optimiser numériquement les termes de phase ou d'amplitude tels qu'ils apparaissent

dans l'équation (0.16) et l'équation (0.17) afin de remodeler l'éclairage et la détection du microscope, comme cela est fait avec le modulateur spatial de lumière (SLM) dans l'optique adaptative et le smart OCT. En particulier, cette approche computationnelle permet de corriger facilement les aberrations de focalisation induites par le décalage d'indice à l'interface verre-eau de notre configuration expérimentale, où un objectif de microscope à immersion d'huile de NA = 1.49 est utilisé pour maximiser la résolution axiale et transversale.

Reconstruction expérimentale sur un échantillon de référence

nous considérons un échantillon de référence : une bille de silice de référence pour comparer les résultats simulés et expérimentaux. Les billes de diamètre moyen 4,98 µm et d'indice de réfraction 1.46 (Cat : SS05003, Bangs laboratories, Inc.) sont déposées sur une lamelle de verre et sont immergées dans l'eau. Pour que la perle soit fixée sur le substrat, on a utilisé une fine couche de Polylysine dont l'indice de réfraction est similaire à celui de l'eau. Nous avons obtenu le jeu de données expérimentales à partir de la bille de référence, puis nous avons reconstruit la bille. Avant de présenter la reconstruction, nous allons discuter de la normalisation de la phase de l'ensemble des données expérimentales.

Normalisation de la phase de l'ensemble des données expérimentales

Toutes les procédures de reconstruction en microscopie diffractive tomographique (TDM) considèrent que les différentes ondes planes incidentes utilisées pour illuminer l'échantillon ont la même phase zéro à l'origine choisie du système de coordonnées. Cette origine est généralement prise au point focal de l'objectif. Mais les dérives mécaniques et thermiques entre les illuminations successives introduisent des déphasages aléatoires à chaque onde plane incidente. Une procédure de normalisation de phase est donc cruciale pour corriger les données afin que les phases de chaque onde plane d'illumination puissent être considérées comme nulles à l'origine. Ensuite, la formation d'un faisceau synthétique qui se focalise à n'importe quelle position est une simple opération d'algèbre. Cette normalisation est basée sur l'amplitude complexe du champ lointain dans la direction de la réflexion spéculaire pour chaque hologramme. Elle correspond à la réflexion du faisceau incident à l'interface verre-eau et apparaît comme un pic de type Dirac dans le plan de Fourier du microscope. Nous supposons que cette réflexion n'est pas affectée par l'échantillon. L'ensemble du signal est corrigé pour que la réflexion spéculaire expérimentale corresponde à sa valeur théorique. Contrairement au coefficient de transmission, qui est généralement toujours proche de l'unité, le coefficient de réflexion théorique ne peut être facilement calculé que si l'interface verre-eau est placée dans le plan focal de l'objet (conjugué au plan de la caméra) : il sera alors égal à la formule de Fresnel. Cependant, c'est rarement le cas, surtout si l'échantillon est épais. Dans ce cas, le chemin optique de la réflexion spéculaire vers la caméra, et donc la phase du coefficient de réflexion

théorique, dépendra fortement de la distance inconnue d entre le plan de mesure et l'interface verre–eau et aussi de l'angle d'illumination. Pour éviter ce problème, nous propageons numériquement les champs pour atteindre l'interface verre-eau, dans ce cas nous considérons le schéma de reconstruction incohérente du champ lumineux tel que donné dans l'équation 0.19. et cette reconstruction est insensible aux erreurs de phase d'illumination.

$$I(\vec{r}) = \sum_{\vec{k}_i} \left| \sum_{\vec{k}} U_s(\vec{k}, \vec{k}_i) e^{i\vec{k}\cdot\vec{r}} \right|^2 \tag{0.19}$$

Au niveau du plan de mesure, l'image incohérente de la perle en champ clair est représentée sur la Fig. 0.2(a). Après une propagation de $1.1\mu m$ à partir du plan de mesure, nous observons quelques caractéristiques nettes qui sont dues à des rayures ou à de la poussière, comme le montre la figure 0.2(b). Ce plan est essentiellement l'interface verre-eau. De cette manière, nous estimons la distance, d entre le plan de mesure et l'interface verre–eau. Avec cette valeur d, le champ mesuré est propagé jusqu'à l'interface, puis nous déphasons le champ pour qu'il soit égal à l'argument du coefficient de réflexion à la position spéculaire.

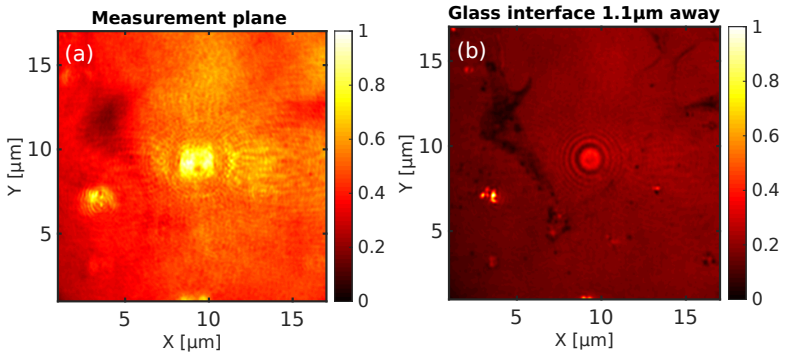

Figure 0.2 – Estimation of the distance between plane of measurement and glass-water interface: (a) Bright field incoherent reconstruction of the bead at the plane of measurement, (b) Bright field incoherent reconstruction of the bead at the glass-water interface

Reconstitution de la bille

Les images reconstruites sont présentées dans la Fig. 0.3(a) et la Fig. 0.3(b) telles qu'obtenues à partir de l'ensemble de données simulées et expérimentales respectivement. La perle reconstruite à partir de l'ensemble de données expérimentales ne correspond pas à celle obtenue à partir de l'ensemble de données synthétiques. Il pourrait y avoir un problème avec l'ensemble de données expérimentales. Il a été démontré que la normalisation de la phase des données expérimentales est très importante car elle permet de se concentrer à l'intérieur de l'eau sans être perturbé par les aberrations à l'interface verre-eau, contrairement à un microscope confocal

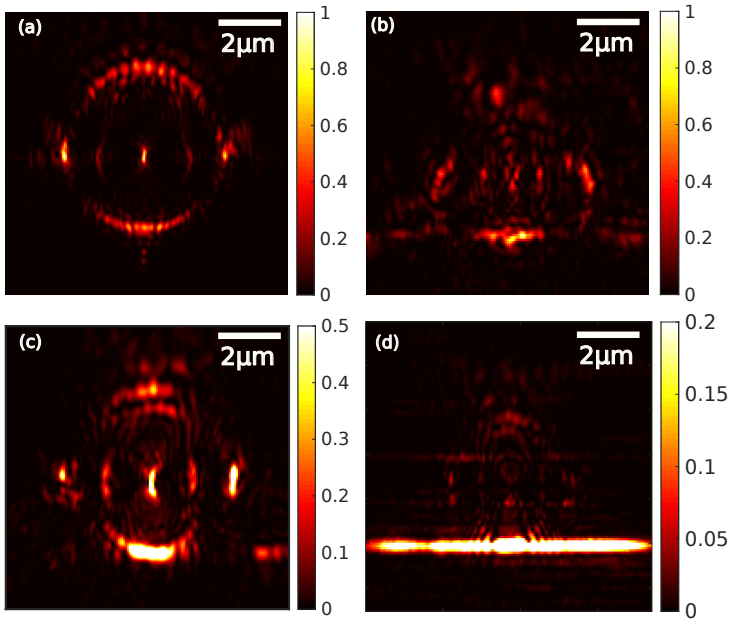

Figure 0.3 – (a) Axial cuts of SyCM intensity reconstructions for a glass bead immersed in water: (a) simulated data, (b) experimental data without the correct phase normalization, (c) experimental data with the correct phase normalization. Color scale has been readjusted on (c) for visualization purpose and (d) Bright field SyCM reconstruction of the bead: here we only see the bright interface, not the bead

standard. Une fois la normalisation de phase effectuée dans l'ensemble des données expérimentales de la perle de référence, nous effectuons à nouveau la reconstruction de l'image et la perle reconstruite est maintenant montrée dans la Fig. 0.3(c). Cette image correspond maintenant mieux à l'image obtenue à partir des données synthétiques (voir Fig. 0.3(a)).

Reconstruction d'un lymphocyte effecteur

Nous avons examiné la capacité de SyCM à imager une cellule biologique. Nous avons considéré des lymphocytes T effecteurs humains, déposés sur une lamelle de verre recouverte de molécules d'adhésion ICAM-1, puis fixés par un traitement au paraformaldéhyde à 4%. Les cellules T effectrices migrent sur les substrats ICAM-1 avec une forme fortement polarisée. Leurs parties centrale et antérieure sont fortement adhérentes et étalées, tandis que leur partie arrière forme une queue partiellement détachée, appelée uropode.

La coupe transversale et axiale de la reconstruction incohérente en champ clair et en champ sombre de la cellule T est représentée sur la Fig. 0.4. La Fig. 0.5 montre la reconstruction 3D cohérente obtenue sur une de ces cellules T : le corps central à droite et l'uropode à gauche peuvent être clairement identifiés. Le corps central apparaît rempli de nombreuses inhomogénéités par rapport à l'uropode. Cela peut

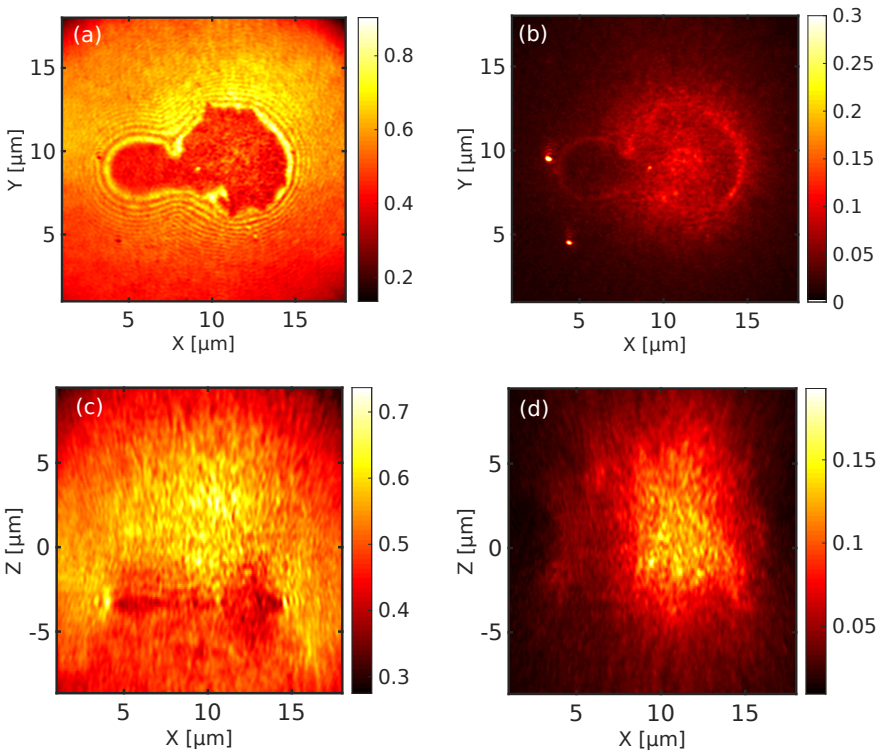

Figure 0.4 – Reflection intensity incoherent reconstruction of a human effector T lymphocyte: (a) Transverse cut (bright field). (b) Transverse cut (dark field), (c) Axial cut (bright field) and (d) Axial cut (dark field). Along the axial direction, the glass-water interface is at (z axis), z = −3 µm.

s'expliquer par le fait que le corps central contient le noyau où de l'ADN très compacté est lié pour produire des changements d'indice de réfraction plus forts que partout ailleurs dans la cellule. Les membranes inférieures et supérieures de la cellule sont aussi clairement retrouvées sur la coupe axiale de la Fig. 0.5(a), montrant la grande capacité de sectionnement de la réflexion SyCM. Une résolution axiale d'environ 400 nm peut être évaluée à partir de la pleine largeur à demi-maximum du profil du signal Fig. 0.5(b) lors de la traversée de ces membranes, proche de la longueur d'onde effective d'illumination de 357 nm dans l'eau.

Reconstruction des billes phagocytées

D'après le résultat de la cellule T effectrice, nous avons vu que la limite de la cellule est clairement visible sur l'image transversale (Fig. 0.5(c) et que les limites supérieure et inférieure de la cellule semblent également être détectables. Dans l'étape suivante, avec des complexités supplémentaires de l'échantillon, nous allons présenter le résultat pour distinguer le processus de phagocytose. La phagocytose est l'un des processus clés de la réponse immunitaire naturelle. En bref, on peut dire que l'agent pathogène est d'abord mangé par le phagocyte, puis présenté aux cellules T pour

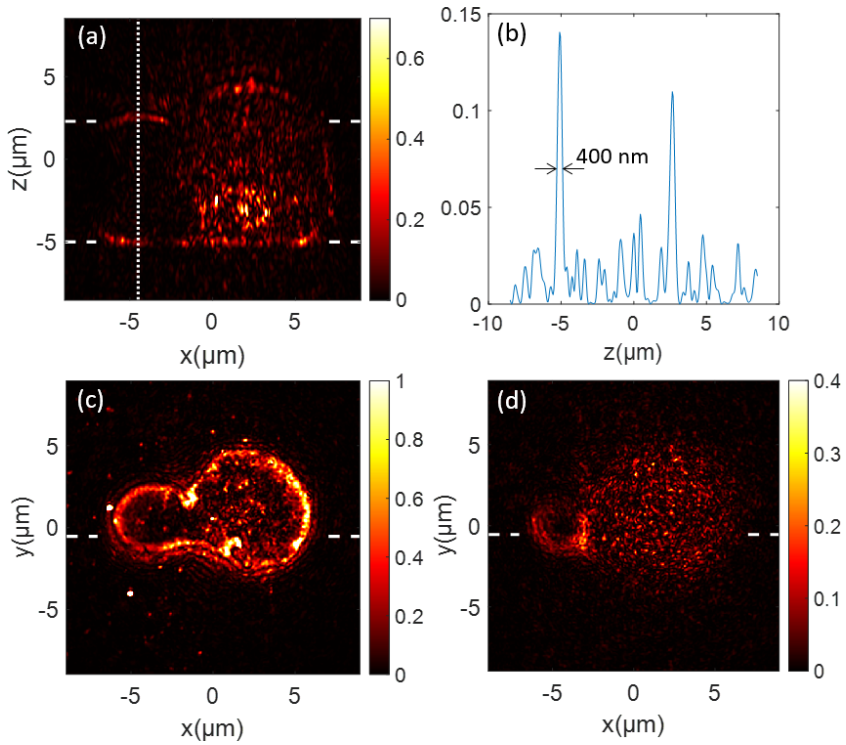

Figure 0.5 – Reflection SyCM intensity reconstruction of a human effector T lymphocyte: (a) axial cut along dashed white segments of (c); (b) intensity profile along vertical dotted white line of (a); (c) and (d) transverse cuts along white dashed segments of (a) at z = −5 µm (glass interface position), and at z = −2,3 µm , respectively. Color scale has been readjusted on (a) and (d) for visualization purpose.

déclencher la réponse immunitaire. Afin d'identifier ce phénomène de phagocytose, nous avons considéré des microsphères recouvertes d'antigènes comme un modèle de pathogène. La raison en est que la bille est très contrastée et pourrait être plus facile à identifier à l'intérieur de la cellule si la bille est phagocytée.

Une image standard à champ clair en transmission de la cellule est représentée sur la Fig. 0.6(a). L'image de transmission en champ clair a été obtenue dans notre TDM supérieur en éclairant l'échantillon par le haut avec une source lumineuse à lampe halogène (Illuminateurs) (Fort imaging system, GLI-154). Dans l'image, un objet de forme ronde est visible, suggérant l'emplacement possible de la perle. Bien qu'il s'agisse de la perle, l'image en champ clair ne nous permet pas de dire si la perle est à l'intérieur de la cellule ou si elle se trouve juste au-dessus de la cellule. Maintenant, si nous regardons la section transversale de la reconstruction des SyCM comme dans la Fig. 0.6(b), nous voyons un espace vide de forme ronde d'environ 5 µm qui indique qu'il s'agit clairement de la perle. Lorsque nous regardons la coupe axiale comme indiqué dans la Fig. 0.6(c) et la Fig. 0.6(d) dans le plan xz et le plan yz respectivement, l'espace vide est également présent, ce qui confirme que la perle a vraiment été phagocytée par la cellule.

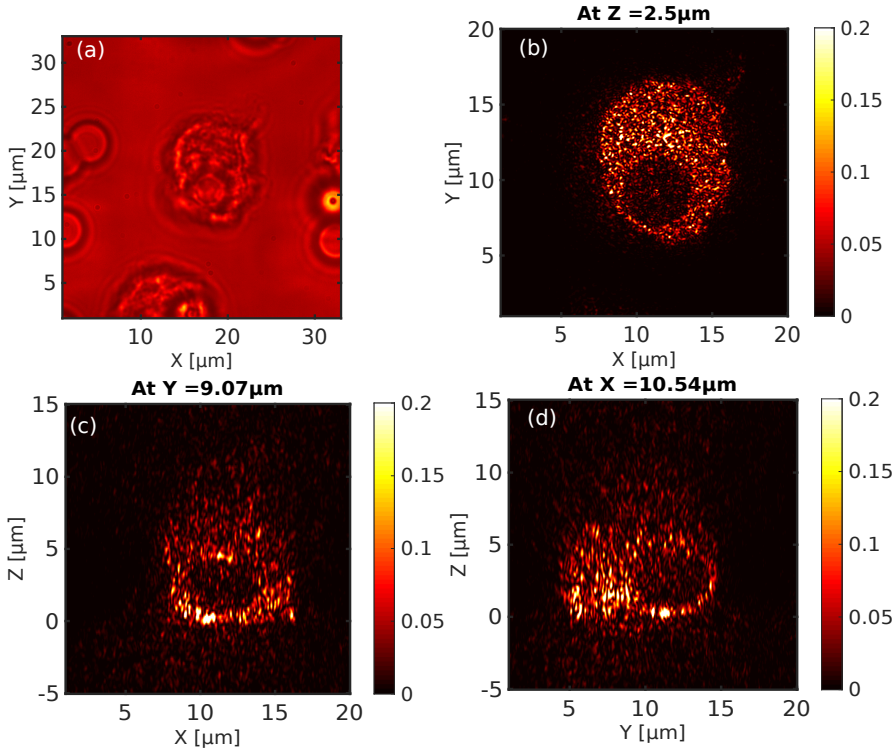

Figure 0.6 – Reflection SyCM intensity reconstruction of a bead phagocyted cell:(a)Bright field transmission intensity image as reference,(b) Transverse cut of the reconstruction (c)xz axial cut, (d)yz axial cut. z = 0 µm corresponds to G-W interface

Abstract

Imaging of biological cells is dominated by fluorescence microscopy, as it provides the best contrast and resolution. However, tagging the samples with fluorophores also have some drawbacks, like phototoxicity (processes involving the cells can be altered by the presence of the fluorophores) and photobleaching (long time measurement is not possible). Moreover, it usually requires an additional sample preparation step. On the other hand, label free microscopy techniques are less resolved but do not suffer from these drawbacks, which make them particularly attractive for biomedical applications. Numerous immunological processes involving cells in solution would highly benefit from a label free characterization technique to develop new quick diagnosis tools. In this context, presently best resolved label free modality based on the detection of scattered light is tomographic diffractive microscopy (TDM). It consists in shining a coherent beam on the sample with different successive illumination angles, detecting the complex (amplitude and phase) scattered field, and reconstructing in 3D the sample from this data set. It has up to now only been used in transmission geometry, and suffers from a poor axial resolution compared to the transverse one. In this work, we present to our knowledge for the first time the characterization of cells with TDM in reflection geometry. This configuration is more difficult to implement due to the lower level of scattered signal and the more complex phase normalization of the data set is required. Having solved these issues, we show that it provides the best resolution if the contour reconstruction of the cells is targeted. We validate experimentally the technique on different immunological cells, with potential application to detect important processes like immunological synapse formation or phagocytosis.

Keywords: Tomographic diffractive microscopy, Synthetic aperture, Synthetic confocal microscopy, Immunological cells

Acknowledgments

First of all, I would like to convey my sincere thanks to **Dr. Guillaume MAIRE** for continuous support that I received from him during this thesis work. His guidance and valuable advises throughout this period have helped me in all aspects. Little by little he introduced me different elements for conducting an independent research. The experiences that I gained in working with him will greatly benefit me in the next stage of my academic endeavors.
I am also grateful to **Dr. Philippe ROBERT** who spend lots of time for preparing the all the sample during the research work. I am thankful for his consideration and express my sincerest appreciation for his assistance in any way that I may have asked for. Special thanks to Anne SENTENAC, Patrick CHAUMET, Kamal BELKEBIR for nice and vivid discussion about different numerical aspect of direct and inverse scattering problems.

Prof. Hugues GIOVANNINI is a man of pleasant personality. During my master study at Karlsruhe Institute of Technology, Germany, I came across to an enticing presentation about Institute Fresnel(IF) delivered by H. GIOVANNINI, that lured me to chose IF for my master thesis and subsequently I spend whole four years in Marseille.
I also extend my sincere appreciation to all the funding agencies in realizing this thesis work. The whole Doc2Amu team and the Protisvalor people and the Fresneleans are very supportive in all aspects. I also remember Francois BRYGO from Bertin Technologies. I would like to remember Kevin, Mahmood, Amir, Debnath, Huicheng Meng, Asif and Remon for their assistance during my stay in Marseille.

Finally, I want to convey my gratitude and appreciation to all of my family members, relatives and friends for their relentless encouragement and mental supports during my stay in France.

Table of contents

List of figures

List of tables

Introduction

With the innovative design of single lens microscope by Antoni van Leeuwenhoek, a new field of study and research namely microbiology was initiated. Even though this microscope is primitive as compared to today's standard, it could produce a magnification of up to 270 times and with this microscope he examined blood, yeast and different insects, cells or bacteria [1]. After that numerous efforts were made in the subsequent centuries to improve the design of microscope for achieving enhanced resolution, magnification and contrast. During this time, not only the light microscope was improved greatly, other form of imaging tools were evolved as for example scanning tunneling microscope [2, 3], scanning electron microscope [4], atomic force microscope [5] etc. Without any doubt these are great tools and immensely helped to examine materials and structural details with nanometric scale but light microscope is the indispensable tools for cell biology due to non invasive properties of light and its ability to produce colorful image. The innovation of classical light microscope was stagnated when the abbe diffraction limit was reached. The imaging tools with this limitation is known as diffraction limited microscope. The quest to overcome Abbe diffraction limit in light microscopy was intensified after the innovation of Laser and fluorescent dye. Employing these Laser and fluorescent dye super-resolution imaging tools [6] like Photo-activated Localization Microscopy(PALM) [7, 8], Stochastic Optical Reconstruction Microscopy (STORM) [9, 10], Structured Illumination Microscopy(SIM) [11], Stimulated emission depletion(STED) [12–14] etc were invented defying the classical diffraction limit and modern cell biology is now unthinkable without these super-resolution form of imaging devices. In all these super-resolution imaging techniques, the biological samples are tagged with specific fluorescent molecules. This labeling is invasive and might change the native state of the biological sample. There are some situations where it is necessary to observe the sample at its native state. Here comes the label free microscopy and might be useful in biomedical applications. As for example optical coherence tomography [15–17] which is a low-coherence based imaging technology. OCT is being regularly used to in vivo imaging of biological tissue, especially of the human eye [18]. Coherent Raman scattering (CRS) microscopy (stimulated Raman scattering (SRS) and coherent anti-Stokes Raman scattering (CARS)) is a label free method of imaging which can be used in histology [19]. The images as obtained from CRS are similar to that obtained from H&E staining [20, 21]. The added advantage of CRS imaging is that it can be done on live and fresh tissue and does not require any fixation or staining. Both OCT and CRS provides resolution in micrometer scale (sub-cellular resolution). These are used to investigate the morphology of highly scattering medium as for example biological tissue. Here we will investigate a label free imaging device to obtain

sub-micrometer resolution of biological cells in solution.

The conventional optical microscope provides images where the contrast is obtained due to the scattering of light by the permittivity distribution of the sample. However, this wide-field light microscopy does not bring any quantitatively information of the permittivity of the sample. Indeed, reconstructing a 3D permittivity distribution from the measurement of scattered fields, i.e. solving the inverse scattering problem, requires ideally that both the amplitude and phase of the field are known [22]. The structure of the object can be reconstructed from the scattered field by applying proper reconstruction algorithm. From experimental point of view, the scattered field containing both amplitude and phase can be collected by a technique called Tomographic diffractive microscopy (TDM) [23–25] whose principle is based on digital holographic microscopy (DHM) [26, 27]. TDM generally consists of illuminating the sample from various directions with coherent collimated light and recording the digital hologram which is formed due to the interference between the reference field and the field scattered by the target object. From the hologram the amplitude and phase of the scattered field are filtered out and is supplied to the reconstruction algorithm and thereby the 3D reconstruction of the sample is obtained.

A short overview of the chapters

In the **first chapter** we will briefly recall the basic parameters of an imaging system and discuss about label free imaging methods of biological cells. The underlying mathematics that governs 3D marker free imaging tools (i.e Tomographic diffractive microscopy, TDM) will be explained. A relationship between the measurement data and the permittivity contrast of the sample is established. The formation of synthetic aperture which is an integral part of TDM has been explained and finally a brief review on TDM is presented.

In the **second chapter** the tomographic diffractive microscopy(TDM) in reflection configuration that has been utilized to perform the experimental work for the manuscript is presented. The detailed working principle of the experimental setup, interfacing software, data acquisition techniques are also included. The 3D reconstruction of the sample from the experimental data-set is discussed in details. Simulation on a simplified object mimicking the immunological synapse and non synapse cases are carried out. A comparison is made among different 3D reconstructions from the simulated data of the phantom object representing the immunological synapse. By considering a reference sample, i.e glass micro sphere the performance of the TDM setup is validated by comparing the reconstruction of the reference micro sphere as obtained from the experiment and the simulation.

Finally, in the **third chapter** the 3D intensity reconstruction of biological cells from the data as obtained by reflection TDM are presented. First we have demonstrated the reconstruction of the contour of a single effector T-cell (key player in steering the

immune responses). The effectiveness of TDM in reflection for identifying phagocytosis phenomenon is presented where an antigen coated glass bead was allowed to be phagocyted by a monocyte. Efforts were also made to detect the immunological synapse. A brief discussion and experiment on mirror assisted TDM on a bead sample were also carried out targeting to enhance the resolution of the 3D reconstruction.

1 Microscopy techniques for 3D label free imaging of biological cells

In this chapter we will briefly discuss the basics of microscopy, the associated parameters that qualify and quantify the goodness of the images obtained from the microscope. We will also explain the label free microscopic techniques and finally present the theory on tomographic diffractive microscopy.

1.1 Basics of microscopy

The origin of the word microscope comes from microscopium. From Gk. micro- meaning “small” and -skopion meaning “to look at”. Therefore microscope is an instrument for viewing tiny objects. In general, we can say a microscope is an imaging system whose purpose is to magnify a small object so that we can see the object without any strain. There are many variations of microscopes. In order to understand the working principle of microscope and the parameters that quantify the goodness of a microscope, here we will consider a light microscope.

A microscope is an optical device that provides an enlarged image of a sample that we can not see with bare eye. A schematic of a microscopic system is shown in Fig. 1.1. A typical light microscope can be viewed as a combination of three basic subsystems. First, an illumination system that shines the sample uniformly with a light source (most modern light microscope use Köhler illumination [28]). Then, an imaging system that collects and magnifies the light scattered by the sample and casts it on an image plane. Finally, a detector is placed on the image plane for recording the scattered light intensity. The detector is usually an electronic camera allowing quantitative measurement of the received field intensity. These three parts altogether act in such way that the light intensity is modulated spatially on the detector which provides a magnified information about the sample.

1.1.1 Important parameters related to an imaging systems

Numerical aperture

The numerical aperture of a microscope objective is a measure of its ability to gather light. It is dependent on two parameters: the angle between the optic axis of objective lens and the edges of the incoming light and the refractive index of the medium

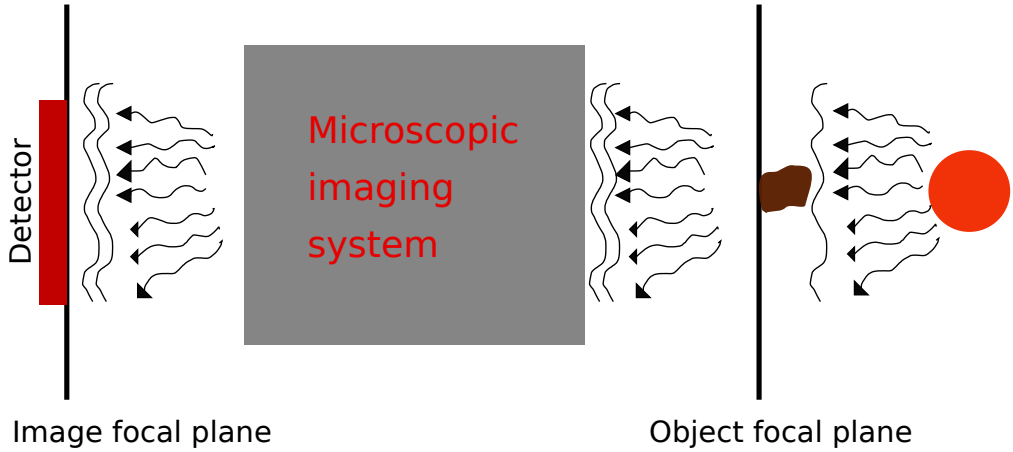

Figure 1.1 – A schematic of microscopic imaging system

through which light is traveling. Mathematically numerical aperture, NA is defined as

$$NA = nsin(\theta) \tag{1.1}$$

with n being the refractive index between the sample and the objective lens and θ being half of the solid cone seen by the objective while light is collected from the sample. The variation of θ is shown in Fig. 1.2. It is obvious that higher the amount of light collected by the objective, better will the quality of the image of the specimen. Therefore, we always desire to have an imaging system with higher NA. From Eq. 1.1, we can control the value of NA by adjusting the value of solid angle and the refractive index as shown in Fig. 1.2. NA is limited between 0 and 1 if air is used as the imaging medium. In air medium NA can never ideally be unity but values of around 0.95 can be achieved. Higher NA can be achieved by increasing the refractive index of the imaging medium (i.e medium between the specimen and the front lens of the objective) as in Fig. 1.2(b) where the NA = 1.33. Today's objective lens of microscope are available that allow imaging in alternative media such as water (refractive index = 1.33), glycerin (refractive index = 1.47), or immersion oil (refractive index = 1.51).

Resolving power

The resolving power of a microscope is defined as the ability to distinguish detail. In other words, this is the minimum distance at which two distinct points of a sample can still be seen as separate entities while observed by the microscope camera or by the observer. The resolution of the microscope is closely linked to the numerical aperture (NA). The resolution is not solely dependent on the NA of an objective, but the NA of the whole system, taking into account the NA of the microscope condenser. Resolution is also related to the wavelength of light that is used to image a specimen, light of shorter wavelengths are capable of resolving greater detail than longer wavelengths [29].

There are three mathematical concepts which need to be taken into consideration

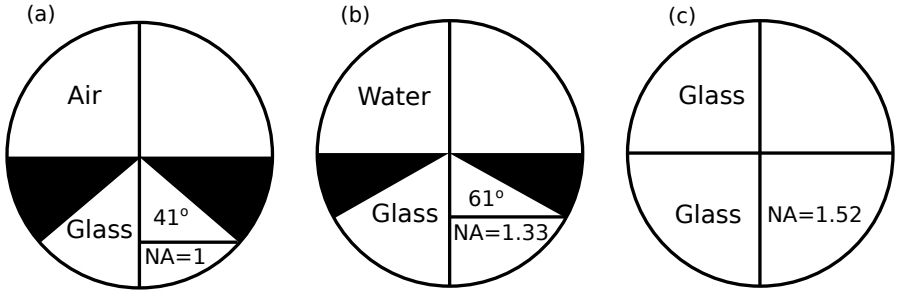

Figure 1.2 – The sketch showing the angle and numerical aperture of the light in glass to fill the top hemisphere overlaying the media of Air (a), Water (b) and homogeneous liquid (c)

when dealing with resolution: "Airy Discs", "Abbe's Diffraction Limit" and the "Rayleigh Criterion". Each of these are discussed below in chronological order.

The diffraction pattern of a circular aperture [30]. i.e., lens is first reported by G.B Airy and is linked to the wavelength of light and the size of the aperture through which the light passes. As viewed the diffraction pattern from the Fig. 1.3, this appears as a bright point of light around which are concentric rings or ripples. This pattern is known as an Airy Pattern. The central point of the Airy Disc contains approximately 84% of the luminous intensity with the remaining 16% in the diffraction pattern around this point. There are of course many points of light in a specimen when viewed with a microscope, and it is more appropriate to think in terms of numerous Airy Patterns as opposed to a single point of light as described by the term "Airy Disc".

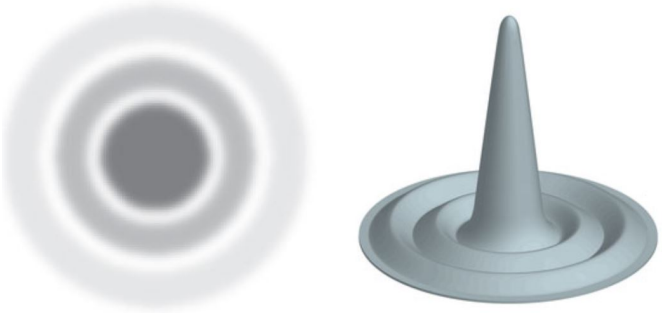

Figure 1.3 – Typical phenomenon of an Airy Pattern, also known as Airy Disc, with its central maximum point of light and the encircling diffraction rings.

In 1873, Ernst Abbe published his theory and formula which explained the diffraction limits of the microscope. This formula links the diffraction limit with the numerical aperture and the wavelength of the light used in the imaging. Abbe recognized that specimen images are composed of a multitude of overlapping, multi-intensity, diffraction-limited points (or Airy Discs). Abbe's diffraction formula for lateral (i.e. XY) resolution is given by:

$$d_{lateral} = \frac{\lambda}{2 * NA} \tag{1.2}$$

and the Abbe's diffraction formula for axial (i.e. Z) resolution is:

$$d_{axial} = \frac{2\lambda}{NA^2} \tag{1.3}$$

Rayleigh built upon and expanded the work of George Airy and invented the theory of the "Rayleigh Criterion" in 1896. The Rayleigh Criterion, which is based on Airy diffraction pattern is basically a refined formula of Abbe's diffraction limits. The Rayleigh Criterion as seen in Fig. 1.4 defines the limit of resolution in a diffraction–limited system, in other words, when two points of light are distinguishable or resolved from each other. Using the theory of Airy Discs, if the diffraction patterns from two single Airy Discs do not overlap, then they are easily distinguishable, "well resolved" and are said to meet the Rayleigh Criterion, Fig. 1.4(a). When the center of one Airy Disc is directly overlapped by the first minimum of the diffraction pattern of another, they can be considered to be "just resolved" and still distinguishable as two separate points of light, Fig. 1.4(b). If the Airy Discs are closer than this, then they do not meet the Rayleigh Criterion and are "not resolved" as two distinct points of light (or separate details within a specimen image, Fig. 1.4(c)). The resolution limit given by the Rayleigh criterion is :

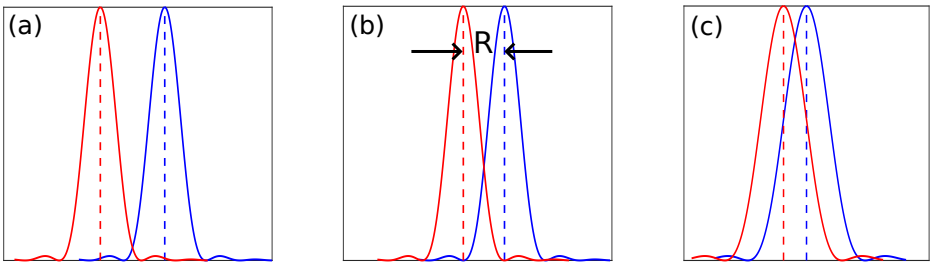

Figure 1.4 – The limit of resolution (defined by the Rayleigh Criterion) shown by the overlapping diffraction patterns of two single Airy Disks: (a): Well resolved, (b): Just resolved, (c): Not resolved

$$R = 1.22 * {}^{\lambda}/_{(NA_{obj} + NA_{cond})} \tag{1.4}$$

where NA_{obj} and NA_{cond} being the numerical aperture of the objective lens and the condenser respectively.

Magnification

Magnification of a microscope is the ability to enlarge an image of an object through a series of lenses to a size multiple times larger than the actual size of the object.

Magnification is the primary purpose of a microscope. When our eye perceives an image through a lens, light is refracted that passes through the lens and projects a kind of virtual image that has the effect of enlarging the object under inspection. This means that when we are looking through a light microscope we are not seeing the "real" specimen rather we see a reproduced and enlarged image of the specimen. The factor that determines the amount of image magnification is the magnifying power of the objective, which is predetermined during construction of the objective optical elements. Typically, objectives have magnifying powers that range from 1:1 (1X) to 100:1 (100X), with the most common powers being 4X (or 5X), 10X, 20X, 40X (or 50X), and 100X. An important feature of microscope objectives is that they have very short focal lengths which in turn allow increased magnification at a given distance when compared to an ordinary lens.

Abbe sine condition

The Abbe sine condition is a condition that must be fulfilled by a lens or other optical system in order to produce sharp images of off-axis as well as on-axis objects. It was first formulated by Ernst Abbe in the context of microscopes. Consider a simplified imaging system as shown in Fig. 1.5 where two rays leaving the object make angles α_o and β_o with the optical axis and (α_i, β_i) be the counterpart of (α_o, β_o) at the image plane. Therefore, the Abbe sine condition can be expressed as

$$\frac{sin(\alpha_o)}{sin(\alpha_i)} = \frac{sin(\beta_o)}{sin(\beta_i)} \tag{1.5}$$

Here, (β_o, β_i) might represent a paraxial ray (i.e., a ray nearly parallel with the optic axis), and (α_o, α_i) might represent a marginal ray (i.e., a ray with the largest angle admitted by the system aperture). An optical imaging system for which this is true for all rays is said to obey the Abbe sine condition.

4F optical system

The 4F imaging system consists of two lenses. A schematic of a 4F imaging system is shown in Fig. 1.6. The input plane is one focal length in front of the objective lens, L_1 while the output plane is located one focal length after L_2, the collector lens. In between the two lenses, we have the Fourier plane. The objective lens, L_1 performs the Fourier transform of the object wave in the Fourier plane where we have the decomposition of all spatial frequencies that makes up the object wave. Whereas the collector lens, L_2 performs a new Fourier transform and produces a magnified image of the object wave at the output focal plane.

If we have a point source at the input, the image is also a point source (Fig. 1.6(a)). Likewise a collimated beam at the input also produces a collimated beam at the image plane of the 4F system (Fig. 1.6(b).

At the Fourier plane, we can place masks of different shapes and opaque object that can filter-out unwanted components from the original image. The Fourier transformation of an image is very similar to a diffraction pattern, where low frequency

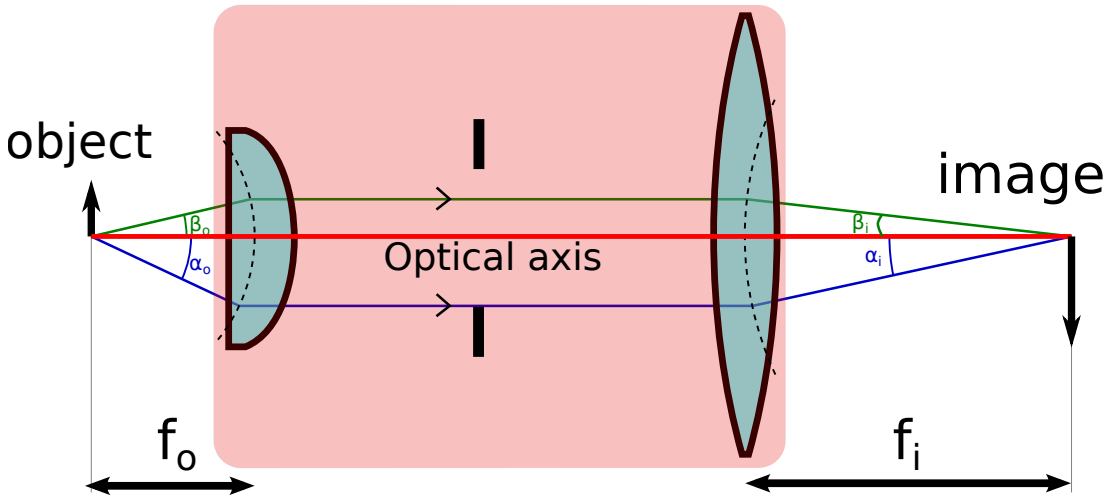

Figure 1.5 – The entrance and exit angles of each ray that passes through an imaging system (shaded box) are related. When the imaging system obeys the Abbe sine condition, the ratio of the sines of these angles equal the (lateral absolute) magnification of the system.

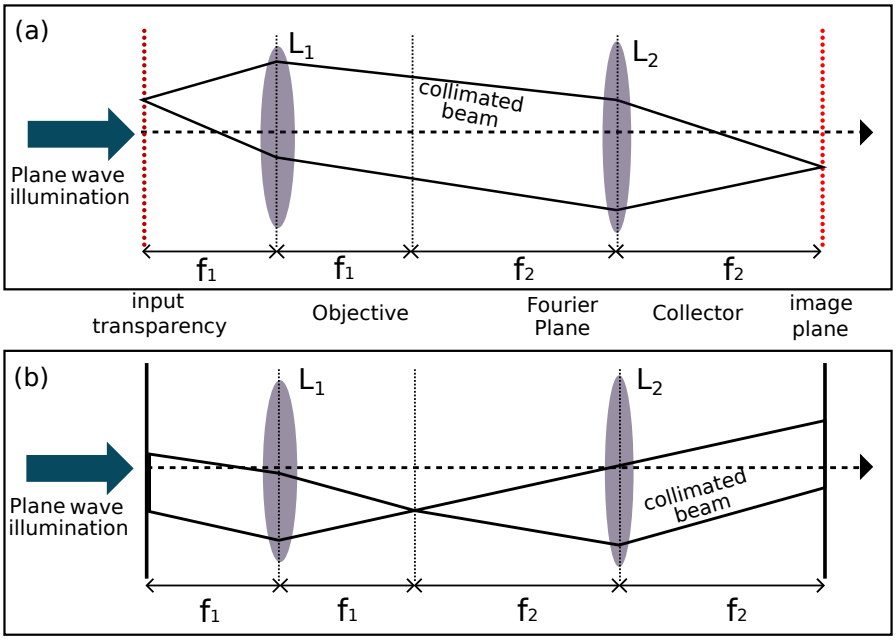

Figure 1.6 – The schematic of a 4F imaging system.

components are located close to the optical axis and the higher frequency components are placed further away from the origin. The shape of the mask varies depending on the application. If we want to remove the low spatial frequency components, the mask can be as simple as a circular disk. Due to this disk the low spatial frequency

components close to the optical axis will be blocked, in essence removing the low spatial frequencies components from the overall contribution to image formation. As we know, the high spatial frequencies components enhance the edges of the object in the image plane, the high pass filtering would allow us to study the contour of a cell or cell-cell interface. The 4F optical system is an ideal example to observe the Fourier optics in action.

Point spread function (PSF)

The point spread function of an imaging system is the image of an infinitely small point source (in practice it is a small fluorescent bead with diameter in the range of nano meter (nm)). Mathematically speaking, point spread function of an imaging system is the response of a 3D impulse function. An ideal imaging system would produce the same image as of the point source. But a practical imaging system produces three-dimensional diffraction pattern of light emitted from an infinitely small point source while transmitted to the image plane via a high numerical aperture objective lens. Due to the diffraction and interference phenomenon, the image of a point like source is bigger than it would ideally be. Fig. 1.7 shows the point spread function obtained from theoretical model. A representation of a point source is given in Fig. 1.7. The lateral and axial image of the point source is given in Fig. 1.7(b) and Fig. 1.7(c) respectively. The axial image of the PSF is larger than the lateral image which indicates that the axial resolution of an optical microscope is less good than the transverse resolution. The degree of spreading gives the indication about how better is the imaging system. Smaller the spreading better the image quality and higher the resolution of the microscope.

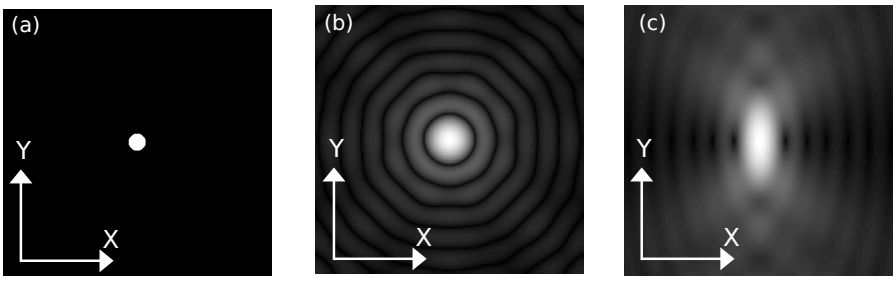

Figure 1.7 – Theoretical depiction of PSF: (a) a point source, (b)image of the point source (lateral section) and (c) image of the point source (axial section)

According to the linearity principle, the object can be decomposed into infinitely many point sources. While imaged, all the point source produces individual diffraction pattern and therefore the final image is blurred. We can write the blurred image as the convolution between the object and the PSF. This is shown in Fig. 1.8.

So if we know the PSF of the imaging system, the blurred image can be deconvoluted to restore the image quality.

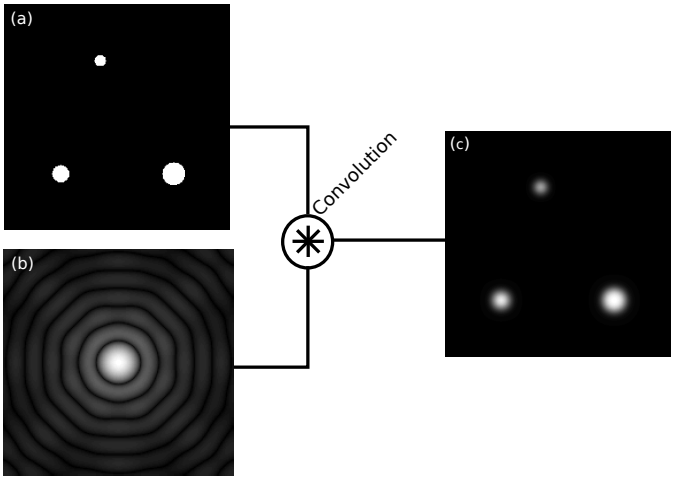

Figure 1.8 – When the object is illuminated with light source, the acquired image of the object arises from the convolution of the object with the PSF.

Optical transfer function (OTF)

The optical transfer function (OTF) [31] of an optical system such as a camera, microscope, human eye, specifies how different spatial frequencies are handled by the system. OTF is a complex-valued function describing the response of an imaging system as a function of spatial frequency. Mathematically, the OTF is defined as the Fourier transform of the point spread function. The magnitude of the complex OTF is called the modulation transfer function (MTF) and the phase of the complex OTF is known as phase transfer function (PTF). Optical transfer function is different for coherent and incoherent light. In diffraction tomography, OTF is calculated by considering coherent light while in fluorescence microscopy OTF is estimated by considering incoherent light. The 2D coherent transfer function [32], $H_{co}(k_x, k_y)$ is shown in Fig. 1.9(a) The incoherent transfer function can be found by the auto-correlation of coherent transfer function as shown in Fig. 1.9(c). For 2D transfer function the auto-correlation operation is shown in Fig. 1.9(b). Fig. 1.9(d-f) represents the corresponding cases for 1D transfer function.

$$H_{inc}(k_x, k_y) = H_{co}(k_x, k_y) * H_{co}(k_x, k_y) \tag{1.6}$$

MTF tells us the magnitude of the weight factor by which the Fourier component of the field at any given spatial frequencies is transferred from the object to the image,

$$E_{im} = FT[FT[E_{obj}] \cdot OTF] = E_{obj} * PSF \tag{1.7}$$

The optical transfer function (OTF) is the central concept in Fourier optics. For each component of spatial frequency in the object intensity, it determines the strength and phase of the corresponding component in the image. The OTF is a property of the

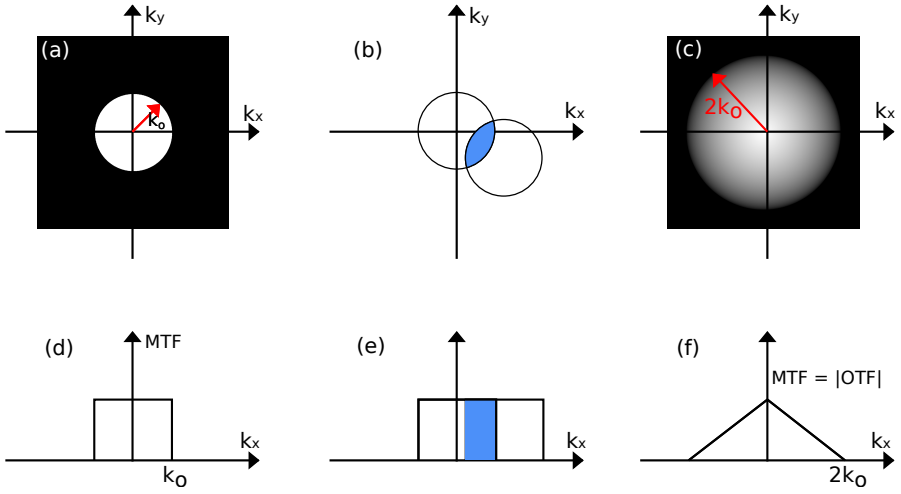

Figure 1.9 – Depiction of Optical transfer function for coherent and incoherent illumination [33]. k_x and k_y are the transverse spatial frequencies, and $k_o = 2\pi/\lambda$. A numerical aperture of 1 is assumed.

optical system alone, and once calculated, can be used to model the image formation process for different objects. It can also be used to compare different optical systems, because in order to achieve high resolution, the cut-off spatial frequency must be as high as possible, and to achieve good contrast the OTF should have a large magnitude. PSF and OTF are applied here on the field, we will show how to apply these concepts on the object contrast in the case of Tomographic diffractive microscopy (TDM).

1.1.2 3D Label free imaging

The biological cells are mostly transparent. When seen through microscope the obtained image is poorly contrasted. To obtain well contrasted images of transparent biological cell, the most commonly used imaging tool is fluorescence microscopy [34–37]. In this technique of imaging, the samples are labeled with certain type of fluorescent dyes, namely fluorochromes or fluorophores, that absorb light in a specific wavelength range, and emit the light with lower energy, that is, shifted to a longer wavelength. The principal advantages of this approach are a very high contrast, sensitivity, specificity, and selectivity [34]. Even though the fluorescence microscopy provides fine details of the transparent biological cell, it also pose some inherent problems. The labeling of fluorescence dye to the cell is invasive which means the labeling process modifies the intrinsic molecular mechanism and moreover the lasers used in fluorescence imaging can be toxic to cells. There is another potential problem known as photobleaching [38]. Photobleaching is the process whereby a fluorophore is converted to a non-fluorescent species, for instance in the presence of oxygen or the use of high intensity laser light. Due to these difficulties it can be difficult to do live cell imaging with fluorescence staining.

A non-invasive and non-toxic alternative to fluorescent microscopy is label-free imaging [39]. From the name, a label free imaging system can be defined as a method for visualizing cells that have not been labeled or altered in any way. To visualize label-free cells, phase contrast microscopy [40] and differential interference contrast (DIC) microscopy [41] are most commonly used. Both techniques use the principle of interference to enhance the contrast. Optical interferometry, converts the phase changes of the transmitted wave induced by the heterogeneous refractive index distribution within the cell into intensity variation. Out of these label free imaging methods we get the qualitative variation of refractive index map but not the quantitative index variation of the phase change. Digital holographic based microscopy [42] can provide the quantitative information of refractive index map. In this case, the recorded complex field image can be numerically propagated to a different depth, hence the name 3D imaging even though in true sens the recorded field data is a 2D image. By recording multiple 2D images for different illumination angles coupled with image processing algorithm, we can reconstruct the intensity map or refractive index map of the sample out of the measured holographic data. The theoretical basis for 3D label free imaging is discussed in the next section. This 3D label free imaging is generally called optical diffraction tomography (ODT), sometimes they are also called as Tomographic diffraction microscopy (TDM) or Tomographic phase microscopy (TPM). In the subsequent discussion we will use the acronym TDM.

1.2 Theory of Tomographic diffractive microscopy

The theory of Tomographic diffractive microscopy (TDM) was first proposed and derived the mathematical formulation by Wolf [22]. It is basically based on solving the scattering problem of scalar wave equation.

1.2.1 Volume integral method of scattered field

With scalar field assumption, the propagation of electromagnetic field, $U(\vec{r})$, through the scattering medium can be described by the Helmholtz equation as follows:

$$\nabla^2 U(\vec{r}) + k_o^2 n(\vec{r})^2 U(\vec{r}) = 0 \tag{1.8}$$

The electromagnetic field can be viewed as the decomposition of incident field component $U_o(\vec{r})$ and scattered field component$U_s(\vec{r})$, then we can write

$$U(\vec{r}) = U_o(\vec{r}) + U_s(\vec{r}) \tag{1.9}$$

In Eq. 1.8, $k_o = 2\pi/\lambda_o$ is the wave number in free space with λ_o being the free space wavelength. The term, $n(\vec{r})$ is known as the complex refractive index of the medium. Sometimes, it is also refereed as the spatial refractive index distribution of the medium and this can be written as:

$$n(\vec{r}) = n_m + \delta_n(\vec{r}) \tag{1.10}$$

Here n_m being the dc component of the index of the medium and $\delta_n(\vec{r})$ is variation index inside the medium which in fact equivalent to the ac component of the index distribution $n(\vec{r})$. With the help of Eq. 1.10, we can write the general equation for wave number which is useful and will be used in the wave equation. The wave number $k(\vec{r})$ is related with $n(\vec{r})$ by the following relation

$$k(\vec{r}) = k_o n(\vec{r}) \tag{1.11}$$

Using the relation $k_m = k_o n_m$ and Eq. 1.10, we can write

$$k(\vec{r}) = k_m \left(1 + \frac{\delta_n(\vec{r})}{n_m}\right) \tag{1.12}$$

With k_m is the wave number inside the medium if it is assumed that there is no variation of index inside the sample. From Eq. 1.12, we can have two different situations. If $\delta_n(\vec{r}) = 0$, i.e. there is no spatial variation of refractive index(i.e, electrical permittivity) we call the medium is homogeneous meaning there is no scatter inside the medium and therefore there will be no scattered component of field (i.e. $U_s(\vec{r}) = 0$). Now the Helmholtz equation as presented in Eq. 1.8 can be written as

$$(\nabla^2 + k_m^2) U_o(\vec{r}) = 0 \tag{1.13}$$

Eq. 1.13 is a second order ordinary differential equation and can be solved analytically. The most common solution of this type of differential equation is plane wave.

Now if we consider $\delta_n(\vec{r}) \neq 0$ in Eq. 1.12, the medium is inhomogeneous meaning there are scatters inside the medium. This is the case that take places in diffraction tomography. The Helmholtz equation can now be written as

$$(\nabla^2 + k(\vec{r})^2) U(\vec{r}) = 0 \tag{1.14}$$

Using Eq. 1.12, we can rewrite Eq. 1.14 as shown below

$$(\nabla^2 + k_m^2) U(\vec{r}) = -f(\vec{r}) U(\vec{r}) \tag{1.15}$$

Where $f(\vec{r})$ is called scattering potential or alternatively it is also known as object function.

$$f(\vec{r}) = k_m^2 \left[\left(\frac{n(\vec{r})}{n_m} \right)^2 - 1 \right] \tag{1.16}$$

With the help of Eq. 1.9 and Eq. 1.13, we can rewrite Eq. 1.15 in terms of the scattered component U_s.

$$(\nabla^2 + k_m^2) U_s(\vec{r}) = -f(\vec{r}) U(\vec{r}) \tag{1.17}$$

The Eq. 1.17 is known as scalar Helmholtz equation for inhomogeneous medium. In TDM, mathematically we basically solve for $U_s(\vec{r})$ and it is not straightforward to find it. There is a way to write a solution for $U_s(\vec{r})$ by the help of Green's function. The

Green's function, which is a solution of differential equation

$$(\nabla^2 + k_m^2) g(\vec{r} - \vec{r}') = -\delta(\vec{r} - \vec{r}') \tag{1.18}$$

Where $g(\vec{r} - \vec{r}')$ is called Green's function and in free space it is given by

$$g(\vec{r} - \vec{r}') = \frac{exp(ik_m(\vec{r} - \vec{r}'))}{4\pi(\vec{r} - \vec{r}')} \tag{1.19}$$

When the differential operator, $(\nabla^2 + k_m^2)$, is applied on the Green's function as indicated in Eq. 1.19, the solution is a delta function. Conversely, we can say that Green's function is the response for a single point scatter (i.e. single delta function). By imposing the principle of linearity, it is possible to write the forcing function shown at the right hand side of Eq. 1.17 as a summation of impulses.

$$f(\vec{r})U(\vec{r}) = \int f(\vec{r}')U(\vec{r}')\delta(\vec{r} - \vec{r}')d\vec{r}' \tag{1.20}$$

Since the Green's function being the solution of the wave equation for a single delta function and because the left hand side of Eq. 1.17 is linear, we can write a solution for U_s by summing up the individual scattered field due to corresponding individual point scatterer. Using this argument, the scattered field due to the forcing function $f(\vec{r}')U(\vec{r}')$ is written as a summation of scaled and shifted versions of the impulse response, $g(\vec{r})$. Then the total scattered field U_s due to all the individual point sources on the right hand side of Eq. 1.17 is written as

$$U_s(\vec{r}) = \int g(\vec{r} - \vec{r}')f(\vec{r}')U(\vec{r}')d\vec{r}' \tag{1.21}$$

The Eq. 1.21 is known as convolution integral. This equation seems the solution for U_s but it is not the case as on the right hand side there is total field which again contains U_s, i.e($U = U_o + U_s$). Therefore we need to solve Eq. 1.21 only for U_s. As analytic solution is not possible we relies on approximation methods for finding the solution. The two most well-known approximation methods are namely Born approximation and Rytov approximation [43]. The Born approximation is discussed in the next section.

1.2.2 Born approximation

According to the first Born approximation, it is assumed that $U_s << U_o$,i.e the scattering field is much lower than the incident field. With this assumption, the scattering field in Eq. 1.21 can now be written as

$$U_s(\vec{r}) \simeq \int g(\vec{r} - \vec{r}')f(\vec{r}')U_o(\vec{r}')d\vec{r}' \tag{1.22}$$

Assume a simplified scattering sample as shown in Fig. 1.10 of varying refractive

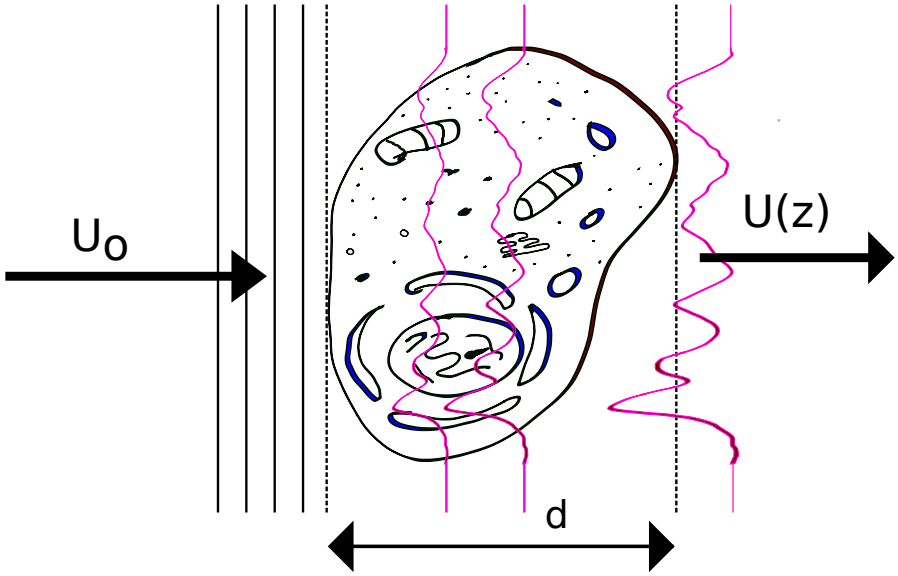

Figure 1.10 – A simplified object: The deformation of the plane wave at the output side, as it passes through the cell

index $n(r)$ inside a homogeneous medium of index n_m. The illumination is a plane wave and the typical phase change, $\Delta\Psi$ between the incident and the outgoing wave induced by the sample is given by

$$\Delta\Psi = \frac{2\pi}{\lambda}(< n > - n_m)d \tag{1.23}$$

With $< n >$ being the average index inside the sample. A necessary condition to be valid for the Born approximation is that, $\Delta\Psi$ less than π [43]. With this we can write

$$(< n > - n_m)d \leq \frac{\lambda}{2} \tag{1.24}$$

The total optical path difference along the sample has to be less than half of the wavelength in order to utilize the first Born approximation.

1.2.3 Relation between the measured data and the object

In the previous sections, we have established the mathematical basis for tomographic diffraction microscopy. From the experimental point of view, what we measure is the scattered field which is possible by using a digital holographic set-up as described in the next chapter. From the measured data we reconstruct the sample. Therefore there must have a link between the measured data and the structure of the object under investigation [44]. In this section we will figure out this relationship. The biological samples are weak scatterer and we assume that First Born approximation is still valid for calculating the scatted field. With this Eq. 1.22 at far field can be written

as

$$U_s(\vec{r}) = \int G(\vec{r} - \vec{r}')f(\vec{r}')U_o(\vec{r}')d\vec{r}' \tag{1.25}$$

where $G(\vec{r} - \vec{r}')$ is Green's function at far field and can be approximated as [43],

$$G(\vec{r} - \vec{r}') \simeq \frac{exp(ik_o r)}{4\pi r} exp(-i\vec{k} \cdot \vec{r}') \tag{1.26}$$

where $\vec{k} = k_o \frac{\vec{r}}{r}$ and $r = |\vec{r}|$. The incident field $U_o(\vec{r}')$ can be written as

$$U_o(\vec{r}') = exp(i\vec{k_i} \cdot \vec{r}') \tag{1.27}$$

With Eq. 1.26 and Eq. 1.27 the far field scattered signal can be written as

$$U_s(\vec{r}) = \frac{exp(ik_o r)}{4\pi r} \int f(\vec{r}')e^{-i(\vec{k}-\vec{k_i})\cdot\vec{r}'} d\vec{r}' \tag{1.28}$$

The integral at right side of Eq. 1.28 is the 3D Fourier transform of the object function $f(\vec{r}')$. i.e,

$$\tilde{f}(\vec{k} - \vec{k_i}) = \int f(\vec{r}')e^{-i(\vec{k}-\vec{k_i})\cdot\vec{r}'} d\vec{r}' \tag{1.29}$$

In terms of Fourier transform Eq. 1.29 can be written as

$$U_s(\vec{k}, \vec{k_i}) \propto \tilde{f}(\vec{k} - \vec{k_i}) \tag{1.30}$$

The equation Eq. 1.30 tells that the field scattered in far field along the direction of $\vec{k}$ for an illumination along, $\vec{k_i}$ is proportional to the Fourier transform of the object function, that is the permittivity contrast of the object [24]. This relationship is linear and is the most important formula for tomographic diffraction microscope under Born approximation. For a 2D object, the scattered field is recorded by 1D sensor (i.e along a line) and the corresponding k-space data lies on a semicircle as indicated in Fig. 1.11. But all practical situation, the sample is 3D and the scattered field is measured by a 2D sensor in image space. The Fourier transform of the measured field by 2D sensor would give the values of the 3D transform of the object over a spherical surface, the Ewald sphere [22, 45, 46].

Using different successive illuminations is the basis towards the formation of synthetic numerical aperture for Tomographic diffraction microscopy. This will be discussed in the next section.

1.3 Synthetic numerical aperture

The concept of synthetic aperture is first used in Radar technology. A Synthetic Aperture Radar [47–49] is an imaging radar mounted on a moving platform. Like a conventional radar, here also the electromagnetic waves are sequentially transmitted and the backscattered echoes are collected by the radar antenna. In the case of SAR the

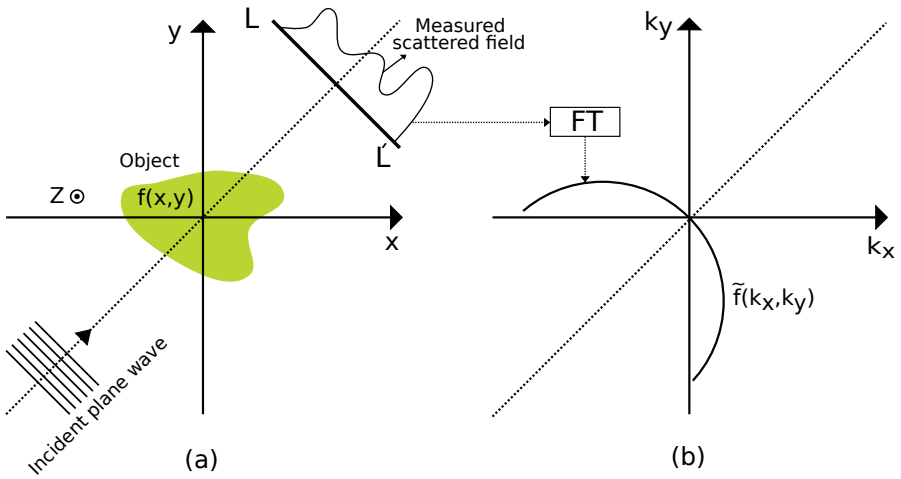

Figure 1.11 – Relationship between the measured scattered field and the object function for 2D object: (a) Real space domain (object space), (b) Spatial frequency domain (k-space)

consecutive time of transmission/reception corresponds to different positions due to the movement of the platform. By using computer, the received signals are coherently added which thereby allows the construction of a virtual aperture that is much longer than the physical antenna length. This basic attribute of SAR is the origin of its name "synthetic aperture", giving it the property of being an imaging radar. In the case of SAR the radar image results from processing the raw data (i.e., after forming the synthetic aperture) and represents a measure of the target object. This same idea can be applied to diffractive tomography to generate a synthetic numerical aperture for enhancing the spatial resolution. The improvement is different if the microscope is in transmission or reflection geometry, as described hereafter.

1.3.1 Formation of synthetic numerical aperture: Transmission Case

According to Eq. 1.30, the accessible Fourier components lie on a section of a sphere and the position of the cap of sphere is dependent on the direction of illumination wave vector. Fig. 1.12(a) shows the location of the cap of sphere for normal incident angle. With other incident angles the position changes accordingly as in Fig. 1.12(b) and Fig. 1.12(c) respectively. While combined together we obtain a larger coverage of the accessible spatial frequencies as in Fig. 1.12(d). This is how a virtual aperture is constructed for Tomographic diffraction imaging.

With a continuum of illumination wavevector in all possible directions, the axial section of the synthetic aperture is shown in Fig. 1.13. The 3D synthetic aperture is invariant by rotation around the z axis. The white region indicates the accessible frequency components of the object. The synthetic aperture is therefore the OTF for the object spatial frequencies K_x, K_y and K_z

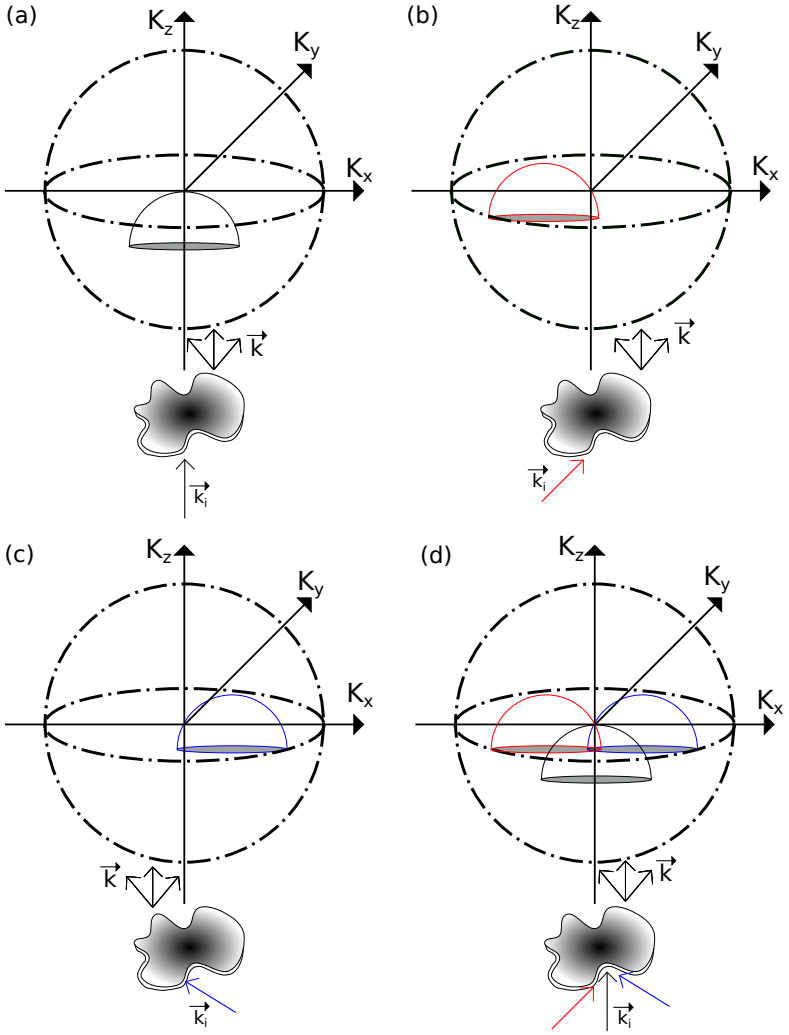

Figure 1.12 – The accessible spatial frequencies in transmission TDM (a) Illumination at normal incident, (b-c) With other illumination angles (d) Synthetic aperture for three illumination angles

In TDM, the transverse resolution is typically twice better in comparison to the standard digital holographic microscopy or wide field microscopy. But in transmission TDM, the axial resolution is around three times worse than its traverse resolution.

1.3.2 Formation of synthetic numerical aperture: Reflection Case

If the illumination to the sample and the detection of the scattered signal from the sample are carried out from the same sample side, in principle, the formation of synthetic aperture is same as in the transmission configuration (Fig. 1.12), here the only change is the spherical caps are flipped upside down along the axial direction as shown in Fig. 1.14 for three different illumination angles. Now if we assume that the

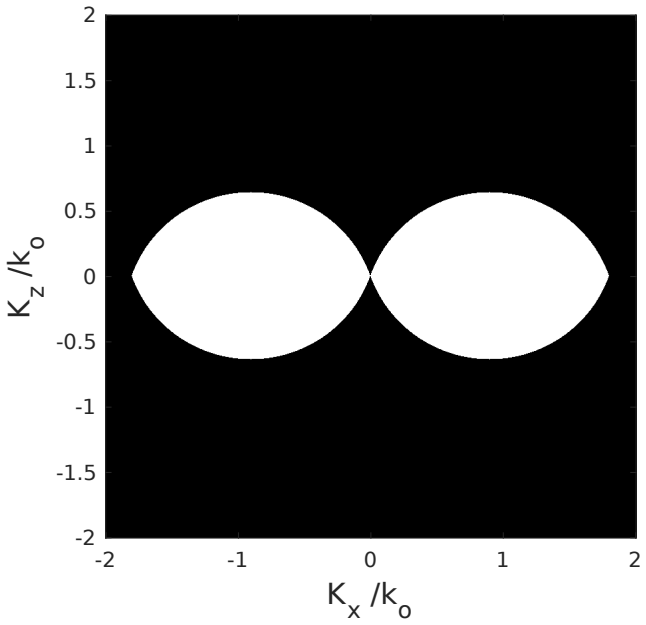

Figure 1.13 – The axial section,(k_x, k_z) plane, of a 3D synthetic aperture (optical transfer function) for transmission configuration with all possible illuminations. The white region represents the detectable spatial frequencies for a given numerical aperture, NA = 0.95

sample is illuminated with all possible direction, i.e with continuum of illumination wave-vector, the resultant axial section of the synthetic aperture is shown in Fig. 1.15.

As we see in Fig. 1.15, detectable frequencies along the axial direction, K_z is relatively higher in comparison to the transmission TDM. As we know the lower spatial frequencies mainly carries the overall volume information of the object while the higher frequencies are responsible for the edge information of the given object. Therefore, TDM in transmission provides mainly the volume information of the sample while the reflection configuration might be suitable for detecting the contour of a biological cell, cell-cell interfaces.

1.4 State of art of TDM

In the previous section we have seen the basic theory of Tomographic Diffractive Microscopy (TDM) along with the variation of TDM namely transmission type and reflection type TDM. Much studies have been conducted on transmission type TDM. Due to the continuous advancement of faster data acquisition devices, computing power and efficient inversion algorithm, the research and development in the domain of tomographic diffractive microscopy has been gaining momentum in recent years and the studies are focused mainly on the TDM in transmission. Several architectures are for example sample rotation [50–52], beam rotation [53–57] or combined [58].

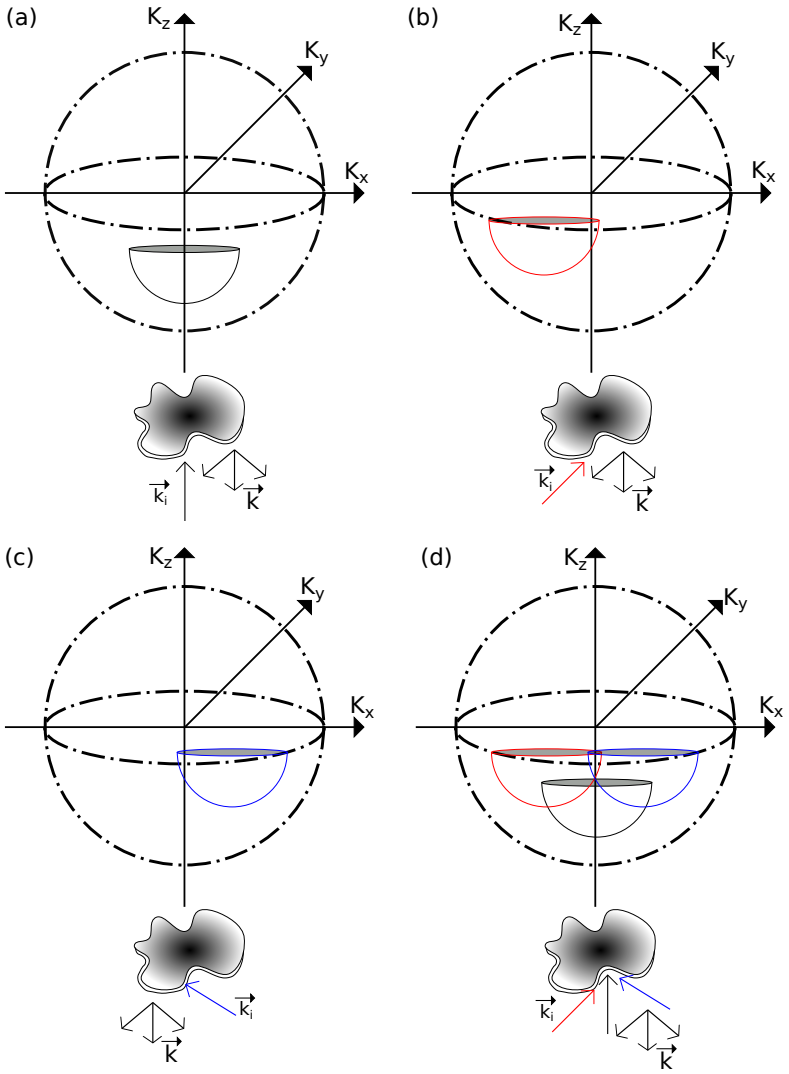

Figure 1.14 – The accessible spatial frequencies in reflection TDM (a) Illumination at normal incident, (b-c) With other illumination angles (d) Synthetic aperture for three illumination angles

A schematic of sample rotation TDM architecture is shown in Fig. 1.16.

The system primarily consists of an off- axis holographic setup of the modified Mach–Zehnder interferometric architecture with a full angle rotational mechanism. The motorized rotational stage holding the sample rotates with an angle separation of 1 degree per step and the digital hologram in each step is recorded and from the hologram the the object is reconstructed. Sample rotation or the combined architecture of TDM provides quasi isotropic resolution while its suffers stability issue of the sample which is very critical for live cell imaging. The beam scanning architecture as shown in Fig. 1.17 has better stability as compared to the sample rotation schematic. Here the galvanomirror (GM) is used to rotate the incident beam and therefor illuminate the sample with different illumination angle. A potential

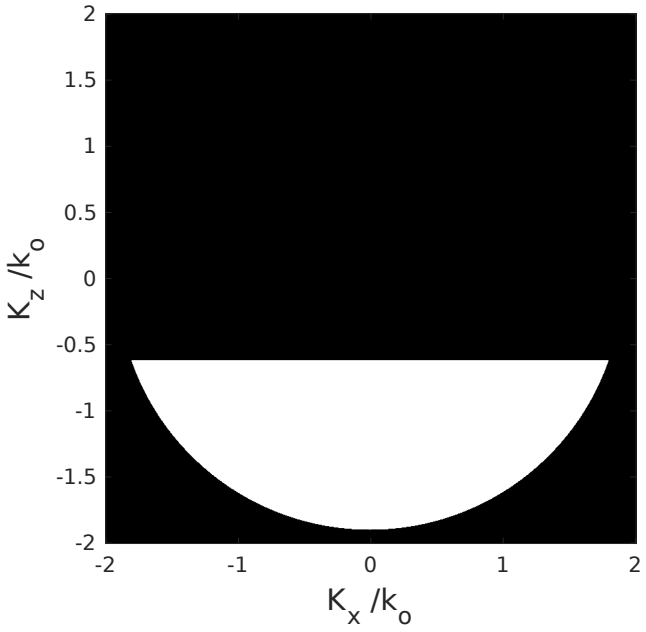

Figure 1.15 – The axial section,(k_y, k_z) plane, of a 3D synthetic aperture (optical transfer function) for reflection configuration with numerical aperture, NA = 0.95. The white region resembles a section of a solid sphere and indicates the detectable spatial frequencies for this particular configuration

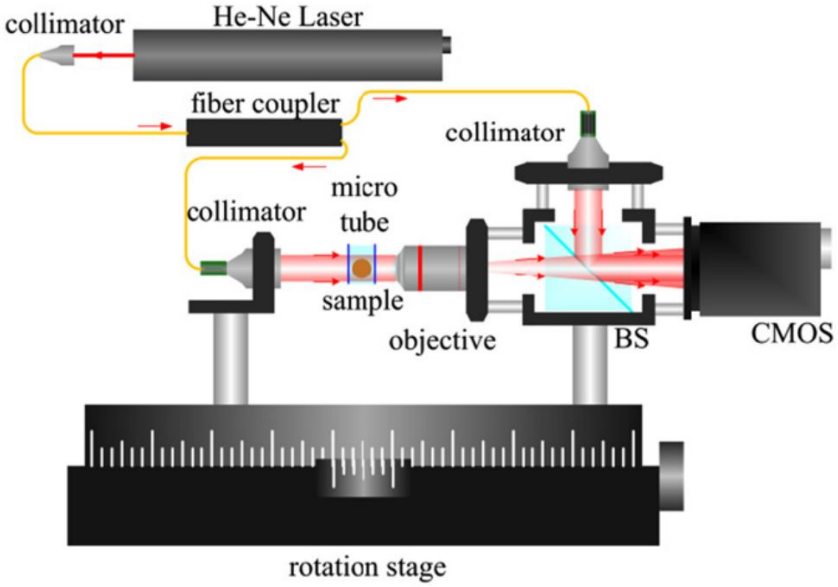

Figure 1.16 – A schematic of TDM with sample rotation architecture [52]

drawback of this type of architecture is that it provides anisotropic resolution due to

the fact of missing cone problem as seen in Fig. 1.13.

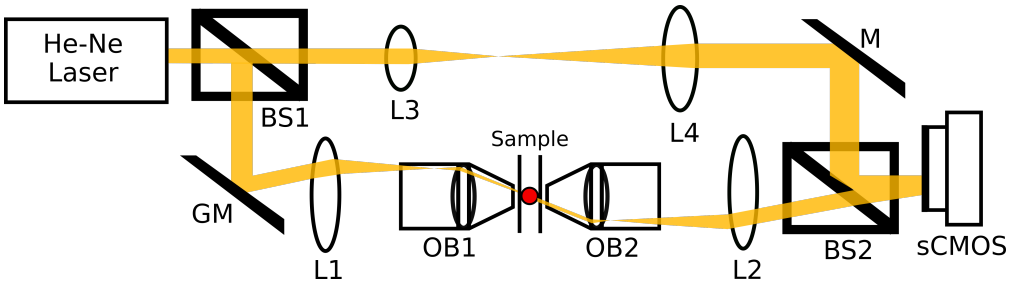

Figure 1.17 – A schematic of TDM with beam rotation architecture [59]

The reconstruction as shown in Fig. 1.18 is obtained with TDM in beam rotation architecture. Here we see that with one illumination angle(the holographic case, the three images from the left column), both the axial resolution and the transverse resolution are not good. While with 1000 illumination angles (the three images from the right column) the structure of the diatomes are well resolved along the transverse direction but sill the axial resolution is less good. This beam rotation TDM architecture which is in transmission mode provides asymmetric resolution.

Numerous models, as for example Born, Rytov, Beam propagation method, Lippmann-Schwinger etc. are explored for reconstructing the sample from the TDM dataset. The Born approximation is the simplest approximation which considers that the total phase change of the field does not exceeds $\pi/2$. Born approximation can provide good reconstruction while working with TDM data (both reflection and transmission) as obtained from the sample [23, 56, 61, 62]. But Born approximation is limited to small size and weakly diffracting sample. The Rytov approximation method which does not depends on the size of the sample. It is based on the fact that the total field is represented as a complex phase [43, 63]. This approximation model is well adapted for the TDM in transmission data but does not work for TDM in reflection [64]. The beam propagation method (BPM) is the approximation technique for solving light scattering problem for slowly varying medium. One major drawback of BPM is that it does not consider the back scattered signal. When there is a discontinuity of refractive index in the sample as for example in cell-cell interface, BPM can not be utilized [65]. The theory of scalar diffraction recognizes the Lippmann-Schwinger (LS) model to be the most faithful. LS model accounts for multiple scatterings, both in transmission and reflection TDM. Iterative forward models that solve the LS equation have been successfully used to reconstruct two-dimensional [66], or three-dimensional samples from the data acquired in the radio frequency regime [67].

Despite the variations to the architecture of the experimental setup and the reconstruction algorithms used, TDM in transmission in general facilitates high accuracy retrieval of various physiological parameters and their internal organelles, including biophysical (Refractive index (RI) distribution, dry mass, dry mass density) and morphological (shape, volume, sphericity) parameters [68]. The sphreicity and the RI distribution of non activated T-lymphocyte of human is presented by Yoon et al [69].

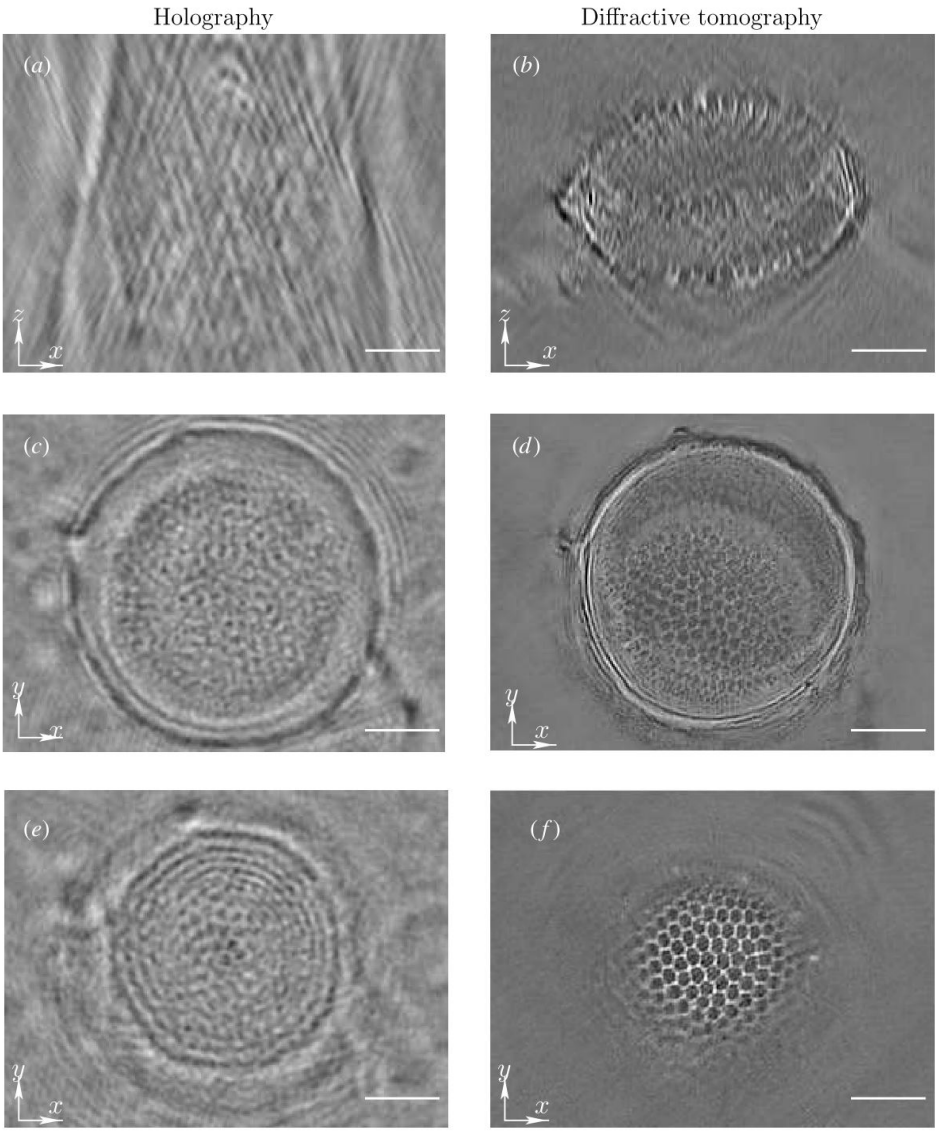

Figure 1.18 – Holography versus tomography. On the left side, three slices extracted from the holographic reconstruction are shown: (a) shows a(x–z) plane and (c), (e) a(x–y) plane. On the right side, the same object is shown in the tomographic case (1000 angles): (b) shows a (x–z) plane and (d), (f) show a (x–y) plane corresponding to (c), (e). The scale bar represents 5 µm. [60]

Sub-cellular structures ware also studied with TDM in transmission. Schürmann et al. observed inversion in the chromatin arrangement in the nuclei of mouse retina cells [70] and physio-chemical changes of the nucleoli in HeLa cells was observed by Kim et al [71] a super resolution phase image of diatom cells (T. pseudonana frustule) is presented at Y. Cotte et al. [72]. Here the lateral resolution of 100 nm and an axial resolution of 150 nm was claimed to be achieved. A single isolated cell nu-

clei was reconstructed with tomographic method by M. Fauver et al. [73] with the spatial resolution of 0,9 µm of the 3D reconstructed image. Several biological cells from a 3D cluster and sub-cellular organelles inside the cells are well detected by self-interference tomographic phase microscopy [50] with isotropic spatial resolution and reconstructing the refractive index map of the sample.

To the best of my knowledge, the first commercial products of TDM in transmission were released by Nanolive [74] in Switzerland in 2015 and Tomocube [75] in Korea at 2017 with 3D reconstructions of live cells with transverse resolutions of 200 nm and axial resolutions of 400 nm [76]. The reconstructed image from Nanolive devices also utilize the concept of digital staining [77], where different organelles inside the cell are given different color digitally and thereby obtaining better contrasted image.

Unlike transmission TDM, the reflection configuration has not been explored extensively. So far it has been utilized to study nano structures [78], like resin stars or nano rods deposited on silicon substrate. A lateral resolution of 50 nm and axial resolution of 200 nm on a sample of resin stars was obtained in the work of T. Zhang et al. [62, 79]. Nano rods on silicon substrate are reconstructed with axial and transverse resolution of 100 nm. [61]. Like TDM in transmission, the reflection configuration has some important feature as for example the ability to collect the high spatial axial frequencies [80] and higher sectioning capabilities [81]. Until now TDM in reflection has been used to study non biological sample like resin star as shown in Fig. 1.19(a). With dark field microscopic modality the branches of the star are not visible as in Fig. 1.19(b). But from TDM in reflection along with proper reconstruction algorithm the branches of the resin star can be identified with high fidelity as depicted in Fig. 1.19(d)[62, 79].

In the next chapter we will explore and optimize the TDM in reflection setup to study the morphology of biological cells and also the interface between cells as for example immunological synapse [82]

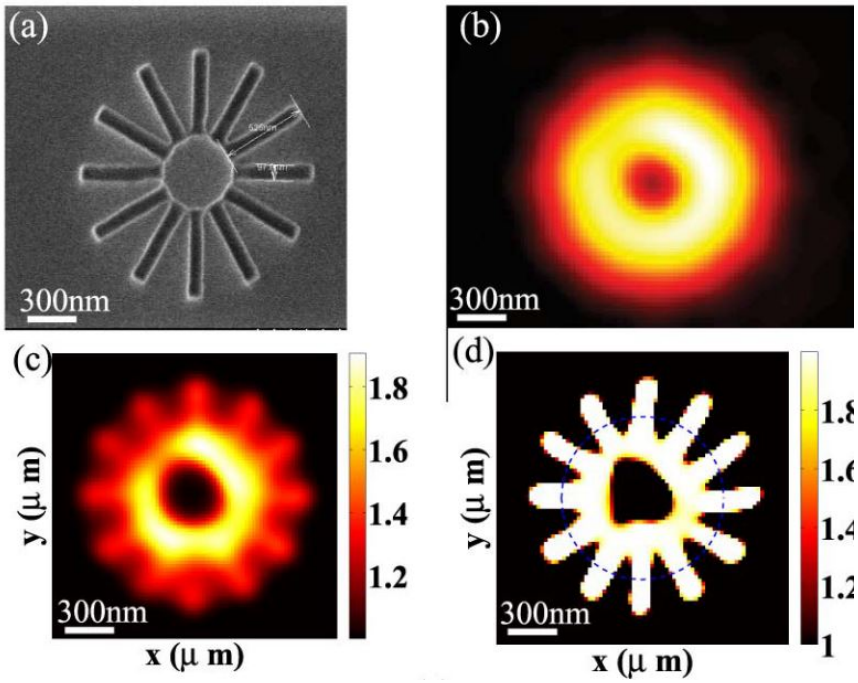

Figure 1.19 – Images of a resin star sample of 97 nm wide rods of length 520 nm and height 140 nm on a Si substrate. (a) Scanning electron image (b) Dark-field microscopy image with NA = 0.95 (c) Permittivity reconstruction obtained from tomographic diffraction microscope image. (d) Permittivity reconstruction obtained with the knowledge of the resin permittivity from the same data as (c). The color code indicates the level of relative permittivity in (c) and (d). [79]

2 Our approach : TDM used as a synthetic confocal microscope in reflection geometry

In this chapter we will elaborate the experimental setup of reflection type tomographic diffractive microscopy (TDM). We will also shed light on some of the main components used in the setup, the mechanical stability of the setup and also the MATLAB interfacing for driving the setup and data acquisition. The role of coherence length of the laser source for suppressing parasitic reflection will be explained. The formation of synthetic aperture will be investigated. Finally, the 3D reconstruction of the specimen from the experimental data will be explained. Both coherent and incoherent reconstruction for a simplified model of immunological synapse from the simulation data will be discussed in details along with the experimental reconstruction of a reference sample: a glass micro-sphere.

2.1 The experimental setup

The most commonly used tomographic diffractive microscopy (TDM) is the transmission type configuration [23, 56, 59, 60, 83–85]. In our experiment, we have developed TDM in reflection to exploit its capability of providing higher axial spatial resolution for studying the contour of a sample or interface between two different objects. Here we are going to discuss the working principle based on which the setup is constructed, then the architecture of the actual setup will be presented and finally a brief description of some of the main components will be explained.

2.1.1 The working principle

The tomographic diffractive microscopy (TDM) is a variation of holographic microscopy [26, 86, 87]. In holographic microscopy, only one illumination is used while in TDM, multiple holograms obtained from different directions of illumination are used to reconstruct the specimen. In principle, holographic microscopy are two types namely in-line holographic microscopy [88] and off–axis type holographic microscopy [89–92].

In our experimental TDM, we use off-axis type digital holography which is based on a Mach–Zehnder interferometer [93]. The schematic of off-axis holography is shown in Fig. 2.1. The input laser beam is split into two parts, one segment called object beam is used to illuminate the sample and the other half is known as reference beam. The object beam interacts with the sample and the signal scattered by the sample is collected by the objective lens. At the camera sensor, the scattered light from the sample and the reference beam interfere and produce interference fringes. Here the reference beam arrives to the camera with a tilted angle ϕ with respect to the scattered signal, hence the name off-axis. The interference fringes as in Fig. 2.2(a) are recorded by the camera and after post processing with computer, the phase and amplitude of the scattered field in the image plane are retrieved.

Let's consider the field scattered by the sample is U_s and the reference wave being U_{ref}, therefore according to the principle of interference, the measured intensity I is :

$$\begin{aligned} &\Rightarrow \quad I = |U_s + U_{ref}|^2 \\ &\Rightarrow \quad I = |U_s|^2 + |U_{ref}|^2 + U_s U_{ref}^* + U_s^* U_{ref} \end{aligned} \tag{2.1}$$

The term $|U_s|^2 + |U_{ref}|^2$ in Eq. 2.1 contains only the intensity. This can be easily seen in the k-space image, i.e the zero order (enclosed by red circle) in Fig. 2.2(c). While the term $U_s U_{ref}^*$ and $U_s^* U_{ref}$ contains both intensity and phase information of the object. These two terms correspond to the small circles enclosed by green color in Fig. 2.2(c). As they contains both amplitude and phase information of the signal scattered by the sample, we filter out one of the ± 1 orders and from this the object is reconstructed by using the reconstruction algorithm as discussed in section 2.3.

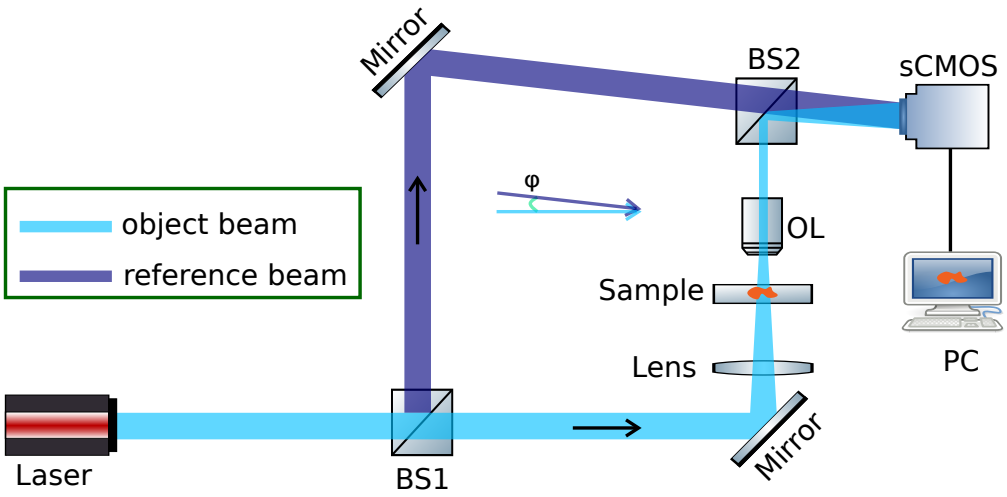

Figure 2.1 – The schematic of an off-axis digital holography

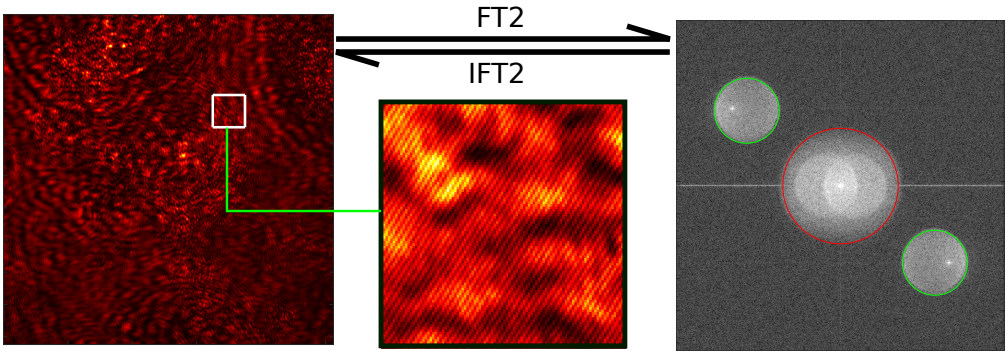

Figure 2.2 – (a) The interference fringes as obtained from a typical off-axis digital holography setup with a biological sample(Monocytes), (b) Magnified view of the fringes, (c) The spatial frequency domain where the zero order which is enclosed by red circle and the ±1 orders are enclosed by green circle. Both the central order and the ±1 orders are well recognized. FT2 and IFT2 are 2D Fourier Transform and Inverse Fourier Transform respectively.

2.1.2 Architecture of the setup

The schematic of TDM in reflection configuration is shown in Fig. 2.3. This architecture of the setup is based on the principle as described in section 2.1.1 and is constructed by assembling discrete optical components.

The main components are light source, rotating mirror, camera, beam splitters, objective lens, lens and mirrors etc. The light source is a super-continuum laser (SuperK Extreme EXW–12, NKT Photonics). The output beam of the laser is filtered at 475 nm with a spectral width of 10 nm by using a variable band-pass filter (SuperK vaira, NKT Photonics). The linear polarizer, *LP* makes the beam linearly polarized

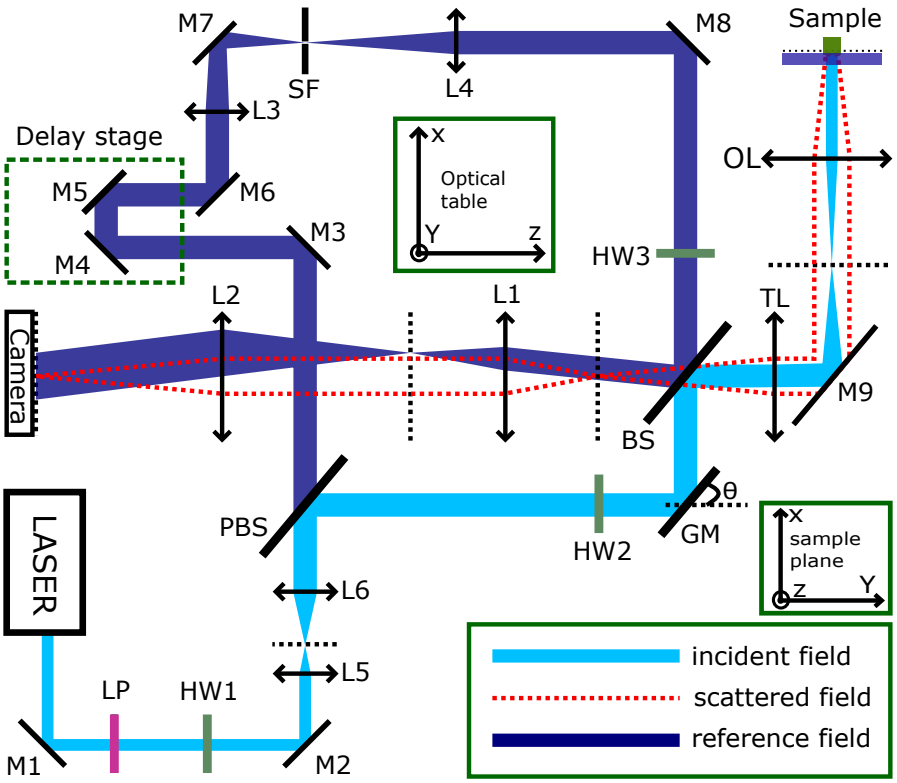

Figure 2.3 – The schematic of the experimental setup: GM, rotating mirror; OL, objective lens; TL, tube lens; L_{1-6}, lens; PBS, polarizing beam splitter; BS, beam splitter; SP, spatial filter; M_{1-9}, steering mirror; LP, linear polarizer; HW_{1-3}, half-wave plate.

and the direction of polarization is vertical, along y-axis (axis convention, inset: optical table, Fig. 2.3). The linearly polarized beam is then divided by polarizing beam splitter (PBS) into a reference beam and an objec beam which is directed towards the sample. In the schematic, the reference beam and the object beam are depicted in different color merely to differentiate them but they both are in same wavelength. The power ratio of reference beam and object beam depends on the polarization direction of the input beam at PBS. The polarization direction of object beam is similar to that of the input beam while the reference beam is polarized horizontally. Since half wave plate can rotate the polarization direction (rotation of polarization is double to that of the physical rotation of the half wave plate) of linearly polarized light, therefore depending on the angle of rotation of $HW1$ (mounted on rotary type mount), we can adjust the power ratio between the object beam and the reference beam. The half wave plate $HW2$ at the object path provides the flexibility to chose the polarization direction of the beam. But in our experiment we keep $HW2$ along y-axis, meaning the polarization direction before and after the half wave plate remains the same.

The galvano mirror(GM),(FS–300, Newport) allows the deflection of the object beam to illuminate the sample. The center of the galvano mirror is conjugated with the

sample through the tube lens TL and the objective lens OL. Therefore by rotating the mirror, the illumination angle is varied without shifting the beam laterally onto the object. The polar angle of the illumination can be varied over the whole numerical aperture, NA of the objective lens.

The scattered field (red dotted line in the schematic) by the sample is collected by the objective lens (Nikon Apo TIRF, oil immersion, 100X, NA = 1.49) and is imaged by a sCMOS camera (Andor Zyla). From image formation point of view, the schematic of the setup has two 4F imaging systems. One which consists the objective lens, OL and the tube lens, TL and the other 4F system is composed of the lens L_1 and L_2. The sample is imaged at the back focal plane of the tube lens and this image is then relayed to the camera by the lens L_1 and L_2. This 4F system provides a magnification factor of 2 and therefor the global magnification is about 200 is achieved. Due to this higher magnification the ± orders as shown in Fig. 2.1(c) in the Fourier space is well separated.

In order to make the optical path length of the reference beam similar to that of the object beam, a delay line is used (Mirror, $M4$ and $M5$ are mounted on the delay stage). The spatial filter SP helps to clean the reference beam. By adjusting Mirror, $M8$, reference beam is allowed to arrive to the camera with a shear angle. In order to obtain the interference fringes, the optical path length of the reference beam ($PBS \rightarrow M_3 \rightarrow M_8 \rightarrow BS$) and the object beam ($PBS \rightarrow GM \rightarrow BS \rightarrow Sample + Sample \rightarrow BS$) should be the same. Therefore the delayline placed at the reference path is adjusted in such a way so that the total optical path length of object beam is almost equal to the optical path length of the reference arm, due to the low coherence length of our laser source(see next section). Now the interference fringes can be produced what we call the off-axis hologram and this hologram is recorded by the camera. The role of half wave plate $HW3$ is to make the polarization direction of the reference beam similar to that of the object beam. Otherwise no interference will take place between the reference beam and the scattered beam.

2.1.3 Laser source

In our experiment we have used the supercontinuum white light laser (SuperK EXTREME EXW-12, NKT photonics). This supercontinuum white light lasers combines the facilities of both a conventional lamp providing broad spectrum and a laser providing intense light [94]. This supercontinuum source can deliver high brightness diffraction limited light in the entire 400 nm to 2400 nm region. This light source is coupled with a spectral filter, it can function as an ultra tunable single line laser. The spectral filter, SuperK VARIA is like a monochromator that effectively tune the SuperK supercontinuum laser into a powerful single–line laser with a 440 nm tuning range and variable bandwidth [95]. The center wavelength of the pass band can be tuned anywhere between 400 nm and 840 nm and the bandwidth can be varied between 10 nm and 100 nm. Increasing the bandwidth of the filter has the added advantages of higher power throughput and reduced speckle in imaging applications.

The SuperK VARIA is compatible with our SuperK CONNECT, a high performance fiber delivery system that comes complete with broadband fibers and a range of termination options such as FC/PC connectors or high quality collimators. Interfacing is handled by the CONNECT fiber coupling block that ensure easy and stable single-mode coupling that can be disconnected and reconnected without alignment.

2.1.4 Objective lens

In our TDM setup we have used Nikon's 100X Apochromat TIRF oil objective (MRD01995) [96]. The working distance of this objective lens is WD = 0,1 mm to 0,16 mm. Nikon's CFI Apochromat TIRF Series Objective Lenses have the highest numerical aperture(NA = 1.49) while using with a standard coverslip and immersion oil. Thanks to high Numerical Aperture, when used in TIRF, they provide the most shallow evanescent field possible with oil immersion lenses. Apochromat TIRF objectives provide chromatic correction from 435 nm to 1064 nm which is well suited for the wavelength, λ = 475 nm that we use in our experiment. Nikon 100X Apochromat TIRF oil objective is also equipped with a temperature-change correction ring. With this ring we can easily correct the temperature induced changes from 23 °C (room temperature) to 37 °C (physiological temperature) – in the refractive index of the immersion oil that might cause spherical aberration.

2.1.5 Role of spatial coherence

For samples like biological cells in water, the back-scattered signal is very weak. To probe these faint signals care must be taken to reduce any source of noise as maximum as possible. Multiple back reflection between the optical components in the experimental setup has significant role to the overall signal to noise ratio. These unwanted reflections cause "parasitic interference" also referred to as "coherent noise" and decrease the quality of the useful signal. The utilization of light sources with small coherent length reduces such disturbing effects [97], but requires a precisely adjusted microscopic setup with exactly matched optical path lengths of both object beam and reference beam. This makes the microscopic setup difficult to build. The use of a partially coherence source for the off–axis holography permits to wash away parasitic reflections. Here, for our laser source, the coherence length is about 100 µm, much shorter than the distance between the sample and the parasitic reflective surfaces and enough to reconstruct object like biological cells. The coherence length of the light source should of course be longer than the maximum occurring path-length difference between the object beam and the reference beam.

2.1.6 Optimization of mechanical path

For optical microscopy, mechanical drift between the sample and the objective lens is a major issue to address. This drift potentially limits the resolution of the microscope [98]. Likewise for holographic microscopy, a small drift of the specimen

with respect to the objective lens is detrimental for the interference fringes and might ruin the measurement. As our sample is immersed in water in a petri dish, we are forced to make a vertical arrangement (vertical to the optical table) for the objective lens as indicated in Fig. 2.4, depicting the mechanical link between the objective lens and the sample. In Fig. 2.4(a), the objective lens is fixed by two support and the sample is hold by a third pillar. The mechanical path between the sample and the objective lens is via the optical table as indicated by red line. With this particular configuration, we observed that the position of a test bead is drifting while seen with small Region of Interest (ROI) of the camera sensor. Then we moved to the configuration shown in Fig. 2.4(b). Here both the sample holder and the objective lens are supported by a common pillar and this effectively reduces the mechanical path length between the sample and the objective as indicated in blue line. This particular configuration demonstrates good stability while observing the same test bead with same ROI of the camera sensor.

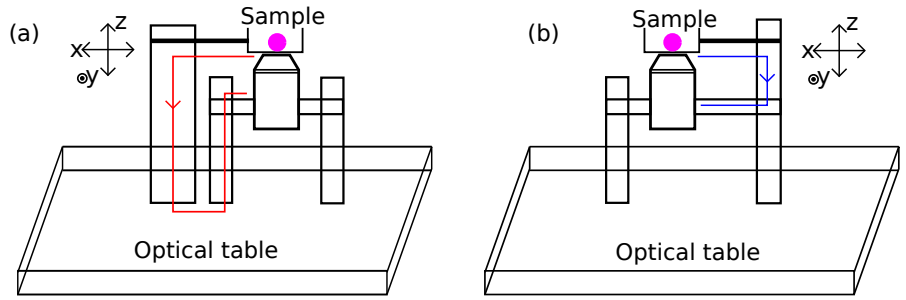

Figure 2.4 – Two different configuration showing the link between the sample holder and the objective lens: (a) The common mechanical path between the objective lens and the sample holder is via the optical table. (b) The common path is reduced as both the sample and the objective lens are fixed on a single support

A photograph of the sample support is presented in Fig. 2.5

2.1.7 Driving the setup

To drive the setup a custom made Graphical user interface has been developed using MATLAB app designer. The main window is shown in Fig. 2.6. From this window, we can control the parameters of the camera like ROI, integration time etc, and also a high speed digital to analog converter (USB DAQ, DT9853). The output from two different channels of the USB DAQ (one for controlling X-position and other for controlling Y-position) are fed to the corresponding input of the galvanomirror controller (FSM CD300B). The voltage of both channels determines the coordinates to specular position of the beam within the numerical aperture in Fourier space. The specular are clearly visible (yellow dots) in Fig. 2.7. The hologram and its Fourier transform are displayed side by side. As our setup is off–axis type, the first order and its conjugate are well separated from the central one. As we record interference fringes,

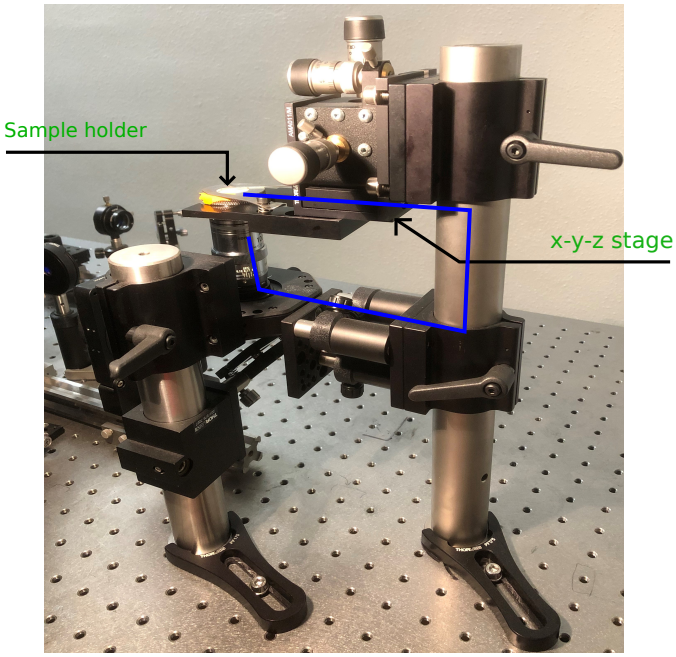

Figure 2.5 – The mechanical path(shown in blue color) is reduced as both the sample and the objective lens are fixed on a single support

sometimes it's become very difficult to optimize the beam power and beam path for obtaining well contrasted fringes. The live feed of the k-space help us greatly to optimize the optical path of the reference beam by adjusting the delay line as indicated in Fig. 2.3, only by looking the k-space image. Once we obtain well contrasted k-space image by playing with the beam power and delay line of the reference path, which in turn also indicates that we have well contrasted interference fringes in the hologram.
Scan pattern: From the drop down menu of the main window we can select the pattern of movement of the object beam as projected to the sample plane. Typically we have several choices like raster scan type, snake movement type, concentric circular or spiral pattern as seen in Fig. 2.7. The raster scan and snake movement are in fact equivalent but the way we send the controlling voltage to the Galvanomirror are different. In raster scan type each horizontal line always start from the left side. In this case, there is a big jump of voltage between the end of a line and the beginning of next line. Large movement of the mirror takes more time to become stabilized and this might cause instability to the beam. In snake movement type scanning pattern, there is no big change of voltage. In both of these scheme, only one channel receives voltage at a time. Whereas in circular and spiral pattern, we have to apply voltage to both X and Y controller simultaneously nor for small mirror movement between to consecutive positions.

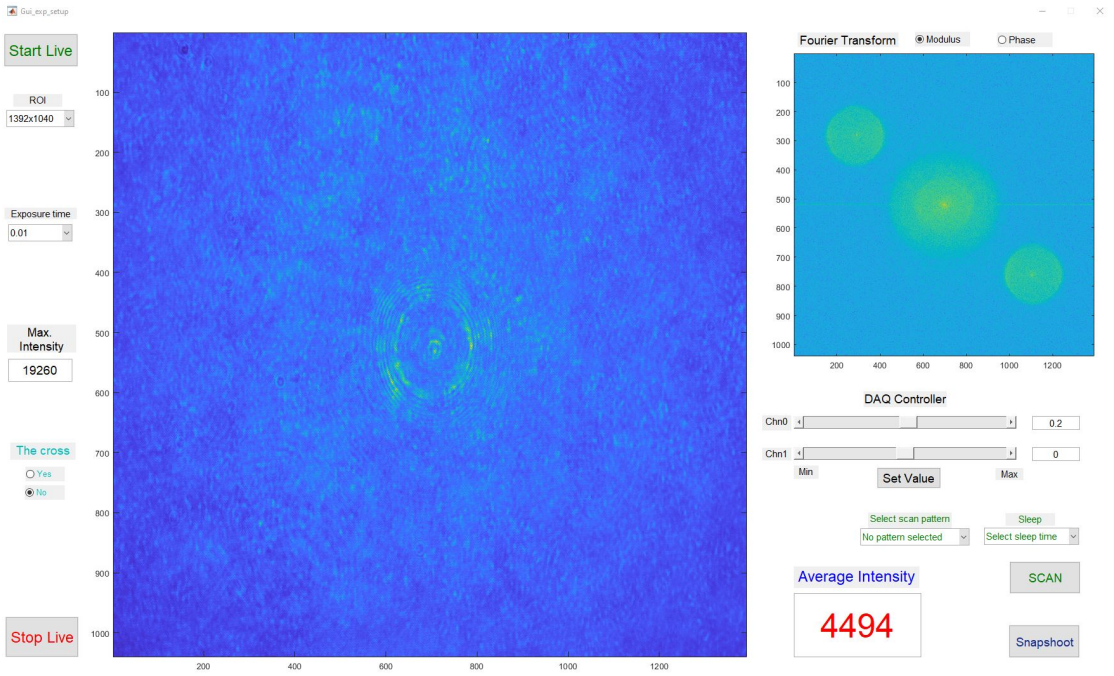

Figure 2.6 – MATLAB GUI for driving the TDM experimental setup.

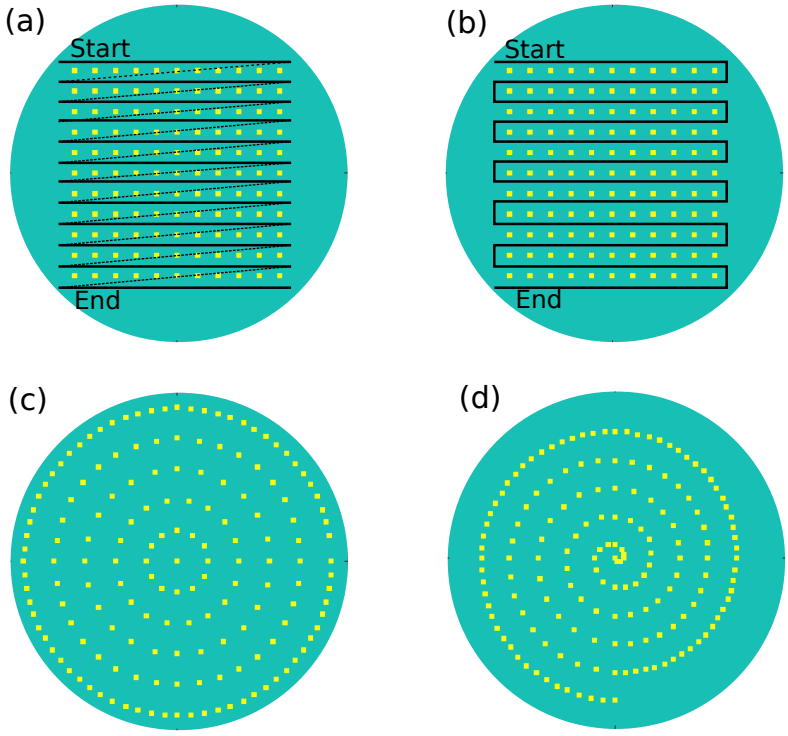

Figure 2.7 – Different scanning pattern within the numerical aperture (Fourier space): (a) Raster scan type (b) Snake movement type (c) Concentric circular type and (d) Spiral

2.2 Principles of synthetic confocal microscopy (SyCM)

In the previous chapter we have established (under Born approximation) the link between the measured scattered field and the object function, i.e the premittivity contrast as

$$\tilde{\Delta\epsilon}(\vec{k}-\vec{k_i}) \propto U_s(\vec{k},\vec{k_i}) \tag{2.2}$$

where $\tilde{\Delta\epsilon}$ is the 3D Fourier transform of the permittivity contrast of the sample (equivalent of to object function). The reconstructed permittivity contrast can directly be obtained form the 3D inverse Fourier transform of the measured data at far field, i.e.

$$\Delta\epsilon(\vec{r}) = \sum_{\vec{k_i}}\sum_{\vec{k}} U_s(\vec{k},\vec{k_i}) exp(i(\vec{k}-\vec{k_i})\cdot\vec{r}) \tag{2.3}$$

Eq. 2.3 tells that if we combine the scattered field for all the illumination angles we obtain the permittivity contrast of the sample. In TDM, the sample is illuminated by plane wave incident with various illumination angles and the reflected scattered signals are collected. Each illumination angle provides access to the detection of different regions of the spatial frequencies in k space.

In fact Eq. 2.3 can also be seen as the scattered field provided by a confocal microscope. When the idea of synthetic aperture as discussed in section 2.2 is combined with the principle of confocal microscopy, the resulting imaging modality we call it the synthetic confocal microscopy (SyCM) or 3D synthetic aperture confocal microscopy. The combined modality is further described in section 2.3. In the conventional confocal microscopy, either the sample or the beam itself is moved in xyz direction to scan the sample point by point. These point wise images are combined by computer and therefore we obtain the 3D image of the sample with finer details. But in our case, we scan the illumination angle during the measurement, they are combined numerically to perform the 3D position scan during the reconstruction process, this is possible because in our measurement at the focal plane we have access to both the amplitude and phase of the scattered field.

This synthetic confocal imaging is based on the fact that scattering is a linear process. The field scattered by a sample illuminated by a beam made of a sum of plane waves is equal to the sum of the scattered fields for each plane wave. Hence, assuming that the phase of all the incident plane waves is zero at the focal point of the objective, corresponding to the origin of the coordinate system, i.e $\vec{r}=0$

$$\tilde{u}(\vec{k},\vec{r}) = \sum_{\vec{k_i}} U_s(\vec{k},\vec{k_i}) exp(-i\vec{k_i}\cdot\vec{r}) \tag{2.4}$$

represents the scattered far-field along the direction of $\vec{k}$ as obtained while the sample is illuminated by a beam composed of plane waves interfering constructively at $\vec{r}$. Then the field at the image domain of the microscope obtained from far field $\tilde{u}$ [99]

can be written as

$$U(\vec{r}) = \sum_{\vec{k}} \tilde{u}(\vec{k}, \vec{r}) exp(i\vec{k} \cdot \vec{r}) \tag{2.5}$$

The field as indicated in Eq. 2.5 corresponds to the complex field that would be measured at the center of the pin-hole of a confocal microscope.

Combining Eq. 2.4 and Eq. 2.5 we can say that the complex field, U is proportional to the permittivity contrast under Born approximation,

$$U(\vec{r}) = \sum_{\vec{k_i}} \sum_{\vec{k}} U_s(\vec{k}, \vec{k_i}) exp(i(\vec{k} - \vec{k_i}) \cdot \vec{r}) \propto \Delta\epsilon(\vec{r}) \tag{2.6}$$

Eq. 2.6 is equivalent to 3D synthetic aperture for obtaining the refractive index and absorption maps of the samples. In fact, calculating its intensity and phase is also meaningful, as they represent the squared modulus and the argument of the reflectance (or transmittance) of a focused beam scanned through the sample. Moreover this SyCM provides flexibility for optimizing the phase or amplitude terms as seen in Eq. 2.4 and Eq. 2.5 numerically in order to reshape the illumination and detection of the microscope, as is done with spatial light modulator (SLM) in adaptive optics and smart OCT [100]. In particular, this computational approach allows an easy correction of the focus aberrations induced by the index mismatch at the glass–water interface of our experimental configuration, where an oil-immersion microscope objective of NA = 1.49 is used for maximizing the axial and transverse resolution, which will be discussed later.

2.3 3D image reconstruction

In the context of experiment, we obtain a set of scattered field $U_s(\vec{k}, \vec{k_i})$ inside numerical aperture for different illumination angles.The 2D Fourier transform of $U_s(\vec{k}, \vec{k_i})$ gives field in measurement plane $z = z_0$. Field can now be propagated numerically to another plane $z = z_0 + dz$ by multiplying with $exp(ik_z \cdot dz)$ before doing the 2D inverse Fourier transform.

Now in the next section we will explain two different ways to reconstruct the sample from the 3D stack of data. These are called Incoherent reconstruction and SyCM (also known as coherent reconstruction) reconstruction. In both incoherent and SyCM procedure of image reconstruction, if we mask the specular, we obtain dark field images otherwise we will obtain bright field images.

2.3.1 Incoherent reconstruction

Here fields for each illumination are propagated to different z planes chosen for the 3D reconstruction, and in each plane their intensities are added. Assume that $U_s(\vec{k}, \vec{k_i})$ be the scattered field in Fourier space for different illumination angles, from which we want to reconstruct the sample. If we now consider the propagation step, dz alog the

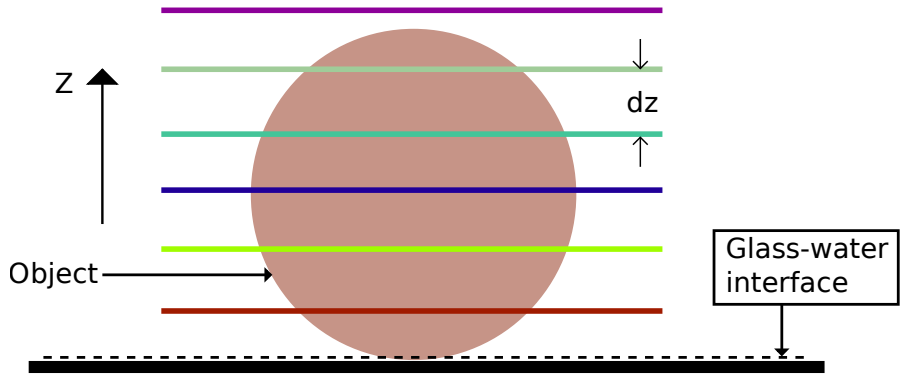

Figure 2.8 – Schematic of image reconstruction model: the colored line indicates different layer to which we numerically propagate the measured data along z axis.

axial direction then we can write, $m = (0,1,2.....N_0) \cdot dz$ for different layer to which the scattered field will be propagated as in the schematic shown in Fig. 2.8.

Then we can write

$$IM(m) = \sum_{\vec{k_i}} |IFT2D(U_s(k,k_i)exp(ik_z \cdot mdz))|^2 \tag{2.7}$$

where IM(m) is the intensity image obtained at m^{th} layer and IFT2D is the 2D inverse Fourier transform.

The field U_s is first propagated to a discrete step, mdz, then we perform 2D inverse Fourier transform of the field and sum up the intensities for all illumination angles. This method of image reconstruction is known as incoherent reconstruction. This process is equivalent to 3D microscopy under Köhler illumination [28]. The algorithm of the incoherent reconstruction process is summarized in the flow diagram as shown in Fig. 2.9.

2.3.2 SyCM reconstruction

According to Fourier diffraction theory of tomographic diffractive theory [43], we can construct 3D synthetic aperture as discussed in section 1.3) by placing cap of spheres in 3D Fourier space, where each cap corresponds to one particular illumination direction. After doing 3D Fourier transform of the 3D synthetic aperture as indicated in Eq. 2.6, we obtain the reconstruction of the object and this procedure is named as coherent reconstruction. But there is another method for obtaing the similar result but in more convenient and straightforward way which relies on 2D synthetic aperture as shown in Fig. 2.10(i) and 2D inverse Fourier transform. This process can be easily understood if we rewrite the Eq. 2.6 where the contribution of axial spatial frequency and the transverse spatial frequencies are separated.

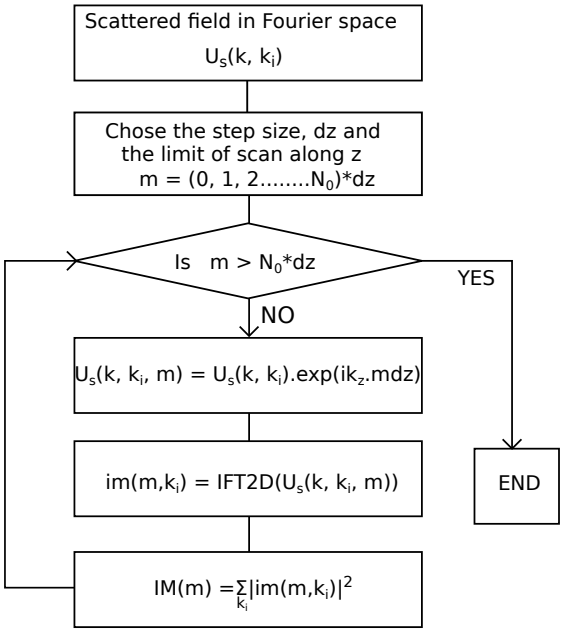

Figure 2.9 – The flow diagram of incoherent image reconstruction process

$$U(\vec{r}) = \sum_{\vec{k_i}} \sum_{\vec{k}} U_s(k, k_i) exp(i(\vec{k_z} - \vec{k_{iz}})z) exp(i(\vec{k_\parallel} - \vec{k_{i\parallel}}) \cdot \vec{r_\parallel}) \tag{2.8}$$

Here according to Eq. 2.8, we perform 2D inverse Fourier transform on 2D synthetic aperture to obtain the synthetic confocal field scattered from a particular z plane. The same process is repeated for all z planes where we want the reconstruction, after having multiplied $U_s(k, k_i)$ by $exp(i(k_z - k_{iz})dz)$ to focus the illumination and detect the scattered field from another plane. This approach permits to choose more freely the z positions of the reconstruction compared to the 3D FT approach : both the range of reconstruction along axial direction and the step size, dz can be chosen independently. From computational point of view, the SyCM image reconstruction procedure can better be understood from the flow diagram is indicated in Fig. 2.11.

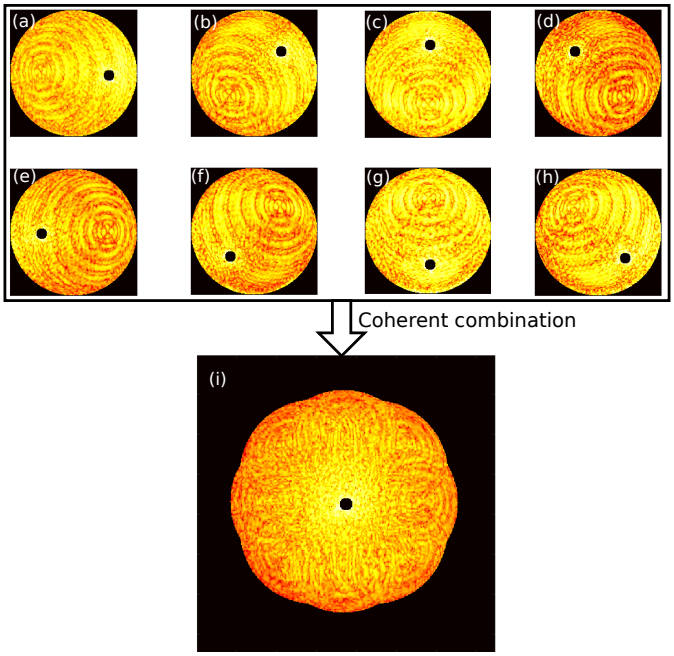

Figure 2.10 – The formation of 2D synthetic aperture for the scattered field from a 5 µm glass bead: (a-h) The modulus of numerical aperture in the Fourier domain shown in log scale for eight different incident angles. The incidences angles were defined by a fixed polar angle of 30° with a regularly spaced azimuthal angle of 45° within 2π radian. Specular position is marked by small black circle. (i) The modulus of the resultant 2D synthetic aperture as obtained by combining all the individual numerical apertures (figures, a-h).

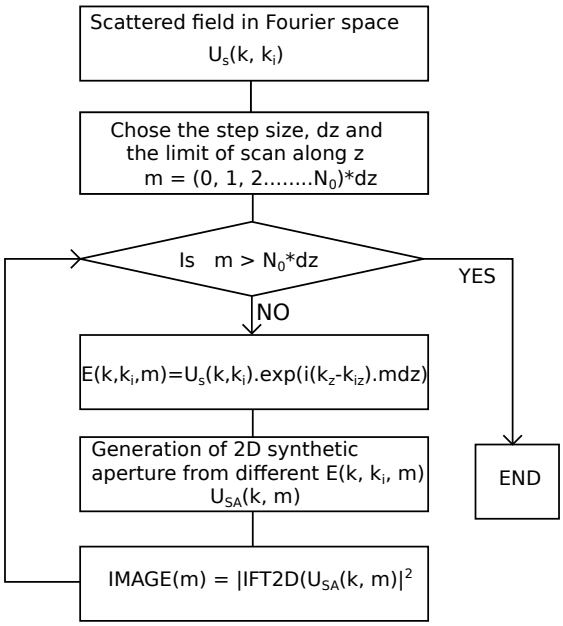

Figure 2.11 – The flow diagram of SyCM image reconstruction process

2.4 Application of the reconstruction techniques to synthetic data

The formation of immunological synapse is crucial for immune response to commence. If a marker free imaging tool can detect the synapse instantly, it could be valuable tools for medical diagnosis. A sketch of the two possible states non-synpase(motile T cell) and synapse (non-motile T cell) of the monocyte and lymphocyte interaction is presented in Fig. 2.12(a-b). It is seen from the Fig. 2.12(b) that the the immune synapse is more likely to occur on the top-membrane of the monocyte(i.e Antigen presenting cell, APC) and the thickness of the synpase is around 300 nm [82, 101, 102]. The detailed view of the synapse and the different protein is shown in the confocal image Fig.2.12(c). The inner circle, or central supramolecular activation cluster (cSMAC, concentrates most of the TCR and CD28, and it is surrounded by the peripheral SMAC (pSMAC) that is formed by integrins. Finally, the most external ring or distal SMAC (dSMAC) is where proteins with large ectodomains are located, such as CD43 and CD45, far from the cSMAC. From the confocal fluorescence image of the synapse we see that the immunological synapse has a characteristic shape with different protein and it could be optically detected. When the synapse occurs we say that the T cell is activated. If the synapse could be detected optically it will also be possible to discriminate cell-cell interface with or without activation of the immune synapse providing the statistical distribution on the quantification of T-cell activation.

We have consider a simplified model to mimic the immunological synapse for the simulation as shown in Fig. 2.13. Here the blue background corresponds to the water medium and the yellow part represents the biological cell.

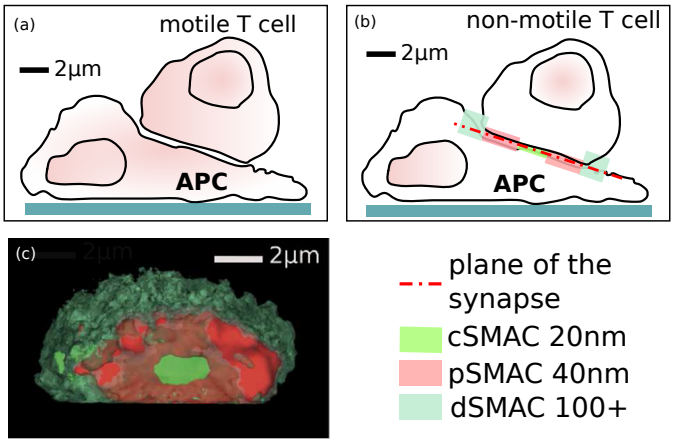

Figure 2.12 – The immunological synapse (a) Non synapse condition (b)Synapse formation: the interface. (c) The confocal fluorescence image of the synapse.

In true sens biological cell is normally transparent and have a small fluctuation of index values inside the cell, here for simplicity we assumed that the refractive index is uniform everywhere which is $n_{cell} = 1.38$. In Fig. 2.13(a), the circular cell is considered

as the T-cell while the bottom big cell represents the antigen presenting cell (APC). In this particular configuration both the cells are in contact and it is assumed that they do not from any synapse. Whereas in Fig. 2.13(b), the T-cell approaches closer to the APC and form the immunological synapse at the interfaces. In both the situation the total optical volume remains the same. The synapses manifests specific protein structure which is shown in fluorescent con-focal images and have certain optical properties. Our target is to identify this interface by using tomographic diffraction microscope. In the first step we do the simulation to identify which type of TDM (either reflection type TDM or transmission type TDM) might serve our purpose and then accordingly perform the experiment towards identifying the synapse experimentally. The underlying mathematical basis for the simulation is discussed in section 2.4.1.

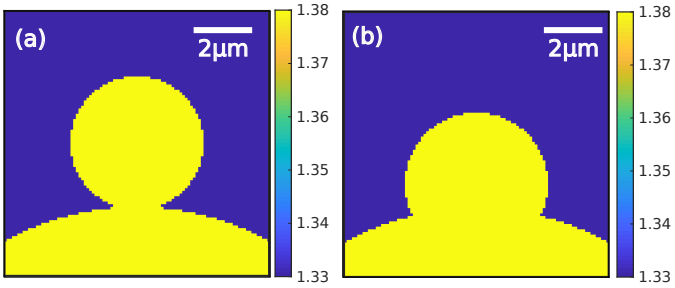

Figure 2.13 – The axial cut of the phantom cell (a) Non synapse condition (b)Synapse formation.

2.4.1 Mathematical basis of the simulation

We have seen that the integral equation for the scattering problem in Eq. 1.21 does not provide analytic solution for the scattered field. Either we have relied on approximated methods or we can solve it rigorously by numerical techniques. Here we have used the discrete dipole approximation (DDA) method for finding the scattered field. Discrete dipole approximation (DDA) first proposed by Purcell and Pennypacker [103], also known as coupled dipole methods (CDM), is a generalized method for computing scattering of radiation by particles or object of arbitrary shape. The theoretical foundation of the CDM relies on the fact that when an object interacts with an electromagnetic field it develops a polarization. If one considers a small enough volume inside the object, the induced polarization is uniform within this volume, and hence that small region can be represented by an electric dipole with the appropriate polarizability. Therefore, any arbitrary object can be discretized as a collection of dipolar small cubical sub-volumes [104–107] as in Fig. 2.14. These dipoles interact with each other and a system of linear equations can be constructed for each dipole and is solved for dipole polarization which then used to find the total scattered field.

From the calculation of scattered field as calculated in Eq. 1.21, if we can write in terms of total field

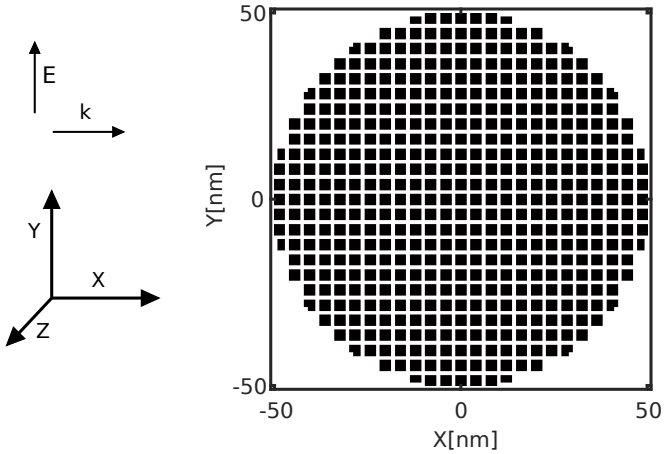

Figure 2.14 – Discretization of the object (transverse section)

$$U(\vec{r}) = U_o(\vec{r}) + \int g(\vec{r} - \vec{r}')f(\vec{r}')U(\vec{r}')d\vec{r}' \tag{2.9}$$

where $U_o(\vec{r})$ is the incident field, i.e the field in the absence of the object. $f(\vec{r}')$ is the susceptibility of the object which is equivalent to the object function. In DDA we solve the integral equation (Eq. 2.9) for the total macroscopic field inside the object. In doing so the first step is to discretize the object in N cubical small subunits with size d, then Eq. 2.9 can be written in as a summation of N integrals.

$$U(\vec{r_i}) = U_o(\vec{r_i}) + \sum_{j=1}^{N} \int_{V_j} g(\vec{r_i} - \vec{r}')f(\vec{r}')U(\vec{r}')d\vec{r}' \tag{2.10}$$

with $V_j = d^3$ being the volume of the cubic subunits.

The Green function and the susceptibilty are assumed to be constant over a single cubic subunit, we can write

$$U(\vec{r_i}) = U_o(\vec{r_i}) + \sum_{j=1}^{N} G(\vec{r_i}, \vec{r_j})f(\vec{r_j})U(\vec{r_j})d^3 \tag{2.11}$$

We can write it in the generalized matrix form as

$$\mathbf{U} = \mathbf{U_o} + \mathbf{GFU} \tag{2.12}$$

with

$$\mathbf{U} = \begin{pmatrix} u_1 \\ u_2 \\ \vdots \\ u_N \end{pmatrix}$$

$$\mathbf{U_o} = \begin{pmatrix} u_{o1} \\ u_{o2} \\ \vdots \\ u_{oN} \end{pmatrix}$$

$$\mathbf{G} = \begin{pmatrix} g(\vec{r_1} - \vec{r_1}) & g(\vec{r_1} - \vec{r_2}) & \dots & g(\vec{r_1} - \vec{r_N}) \\ g(\vec{r_2} - \vec{r_1}) & g(\vec{r_2} - \vec{r_2}) & \dots & g(\vec{r_2} - \vec{r_N}) \\ \vdots & \vdots & \ddots & \vdots \\ g(\vec{r_N} - \vec{r_1}) & g(\vec{r_N} - \vec{r_2}) & \dots & g(\vec{r_N} - \vec{r_N}) \end{pmatrix}$$

$$\mathbf{F} = \begin{pmatrix} f(\vec{r_1})\delta_{11} & f(\vec{r_1})\delta_{12} & \dots & f(\vec{r_1})\delta_{1N} \\ f(\vec{r_2})\delta_{21} & f(\vec{r_2})\delta_{22} & \dots & f(\vec{r_2})\delta_{2N} \\ \vdots & \vdots & \ddots & \vdots \\ f(\vec{r_N})\delta_{N1} & f(\vec{r_N})\delta_{N2} & \dots & f(\vec{r_N})\delta_{NN} \end{pmatrix}$$

δ_{ij} in matrix F is the Kronecker symbol : $\delta_{ij} = 1$ for $i = j$ and 0 otherwise. Using identity matrix **I** we can now write

$$\mathbf{U} = (\mathbf{I} - \mathbf{GF})^{-1}\mathbf{U_o} \tag{2.13}$$

Therefore the calculation of U can be done through the inversion of the matrix (I - GF). This inversion is done iteratively using a conjugate gradient method [108]

2.4.2 Formation of the object

The scattered field is calculated using a home made program, IFDDA (for Institut Fresnel DDA) [105]. The object is created with Matlab in a text file sent to this program. First a cubic box of uniform refractive index is created. Inside the box the target specimen is constructed. Then the entire domain,(i.e the entire box) is discretized. The discretization step is chosen in such a way that the condition as indicated in Eq. 2.14 is satisfied.

$$\Delta x \ll \frac{\lambda}{4} \tag{2.14}$$

Where Δx distance between two cubic subunit, λ being the wavelength of the incident field. Once the discretization is done properly, the permittivity value of each point $\vec{r}(x, y, z)$ of the cubic box is written in a text file. The first line of the text file contains the dimension of the box (i.e. the number of dipoles) and the separation of dipole as shown in Table 2.1.

As we have considered a cubic box, the number of discrete point dipoles is the same along x, y and z axis. In the text file, from second line onward, each line corresponds to $\vec{r}(x, y, z) = \epsilon$. A segment of this is shown in Table 2.2. The true dimension of the cubic box containing our simulation object is (side, width, height) = (80 µm, 80 µm, 80 µm). Therefore the first coordinated points, (1, 1, 1) corresponds to (80 nm, 80 nm,

Table 2.1 – The first line of the object text file

No of points			Step size (nm)
Nx	Ny	Nz	Δx
100	100	100	80

Table 2.2 – The coordinate and permittivity of discretized object

Cartesian coordinate(nm, nm, nm)			Permittivity	
x	y	z	ϵ_r	ϵ_{im}
8.000e+01	8.000e+01	8.000e+01	1.7689	0
1.600e+02	8.000e+01	8.000e+01	1.7689	0
–	–	–	–	–
6.400e-06	3.200e-04	6.400e-06	1.9044	0
6.400e-06	5.760e-04	6.400e-06	1.9044	0
–	–	–	–	–
–	–	–	–	–
7.920e+03	8.000e+3	8.000e+3	1.7689	0
8.000e+3	8.000e+3	8.000e+3	1.7689	0

80 nm) and last dipole is at the location (100, 100, 100) corresponds to (80 µm, 80 µm, 80 µm) which is indicated in Table 2.2.

2.4.3 Simulation for multiple angles

In order to obtain TDM image from the simulated data, we need to perform the simulation for different incident wave vector $\vec{k_i} = (k_{ix}, k_{iy}, k_{iz})$. As shown in Fig. 2.15(a), each pair of (θ, ϕ) , i.e, polar angle and azimuth angle respectively indicates different orientation of the incident plane wave. These (θ, ϕ) are chosen on a regular square grid in Fourier space for simplicity. The scan path of the yellow dots following the purple line is shown in Fig. 2.15(b). Here the yellow dot at the center of the numerical aperture indicates the normal incident of the object beam giving the value $(\theta, \phi) = (0°, 0°)$. Basically each scan position is controlled by a pair of (θ, ϕ) values. From these value we calculate the incident wave vector $\vec{k_i}$ and according the the convention as shown in Fig. 2.15(a) is given by

$$k_{ix} = k_o sin(\theta) cos(\phi), k_{iy} = k_o sin(\theta) sin(\phi), k_{iz} = k_o cos(\theta) \tag{2.15}$$

where $k_o = \frac{2\pi}{\lambda}$ angular spatial frequency in free space.

All the pairs of (θ, ϕ) for all the scan points are written in a text file. Finally this text file containing the angles and object text file as described in section 2.4.2 are fed to the DDA program to calculate the scattered field rigorously.

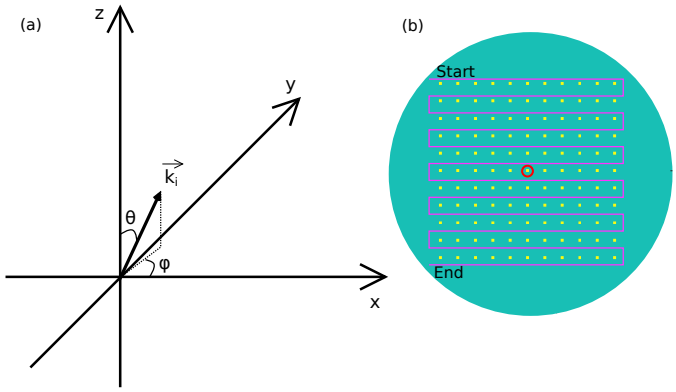

Figure 2.15 – (a) Axis convention of incident wave vector k_i the target object is placed in xy plane and the optical axis is along z axis (b) The scan pattern: the path of the object beam in xy plane. Each yellow dot indicates the tip of the incident wavevector.

2.4.4 Comparison of IFDDA with experiments

In this section, we compare the microscope images given by IFDDA to that obtained experimentally with the microscope in reflection configuration described in [109–111] and illustrated in Fig. 2.3.

The sample is placed on a coverslip with index 1.5 that matches that of the oil objective of Numerical Aperture 1.45. They are illuminated by a collimated beam of wavelength 475 nm, assimilated to a plane wave, that comes from the glass substrate and makes an angle θ with respect to the optical axis. The plane of incidence is (x, z). An off-axis holographic system allows us to measure the complex field at the image plane. The first sample on the coverslip is a sphere of index 1.608 and diameter 5 µm surrounded by water (index 1.33). The microscope is tuned so that the object focal plane cuts the middle of the sphere, at 2500 nm above the glass substrate. The magnification of the microscope, which should not be overlooked when dealing with polarized waves [99], is 200. Fig. 2.16 displays the experimental and simulated intensities when the incident beam illuminates the sample at an angle $\theta = 30°$ with TE and TM polarizations. We observe a good agreement between the experimental and numerical results. The differences may be explained by the fact that the focal plane and the angle of incidence are not known with accuracy, ± 300 nm and ±2° respectively. The non-absorbing glass sphere being a resonant object (as its optical volume is larger than one wavelength cube) a slight change in the illumination conditions may affect significantly the image pattern. The second sample on the coverslip consists of a resin star made of 12 branches of width of 90 nm, length of 400 nm and height 160 nm of refractive index 1.5 in air. The inner diameter of the star is 800 nm. A TE polarized collimated beam illuminates the sample at an angle of $\theta = 68°$ so that it is totally reflected at the glass-air interface. The microscope is tuned so that the object focal plane is placed in air at 350 nm above the substrate and its magnification is 290. Fig. 2.17 shows the experimental and numerical images obtained at the image focal

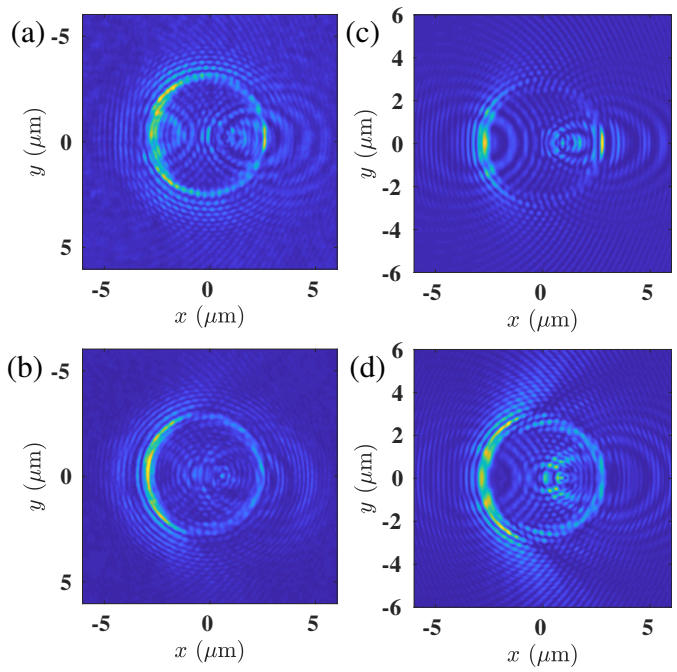

Figure 2.16 – Intensity measured and simulated at the image plane of a microscope in reflection configuration, NA = 1.45 and magnification factor, M = 200, when the sample is a sphere of radius 2500 nm and relative permittivity of 2.5857, placed in water and deposited on a coverslip. The sphere is illuminated by a TE or TM polarized collimated beam with $\theta = 30°$. The left (right) column displays the experimental (numerical) intensities. (a,c) TE polarization, (b,d) TM polarization.

plane and at the Fourier plane. We observe a very good agreement between the simulation and the experiment [112].

2.4.5 3D reconstruction of the phantom cell

The simulation program, IFDDA as presented in section. 2.4 gives the flexibility for obtaining TDM dataset both in transmission and reflection configuration. For the object as presented in Fig. 2.13, we perform the simulation for both transmission and reflection type TDM. Here we will present the reconstruction as obtained from the scattered signal by the phantom cell for both the incoherent and coherent (synthetic confocal) procedures as discussed in section 2.3.

In Fig. 2.18, the reconstructed images in transmission as obtained from both coherent and incoherent procedures do not give any information regarding the interface of the objects. They also do not permit to discriminate between the two object configurations of Fig. 2.13(a) and Fig. 2.13(b).

In reflection type TDM, the images as obtained from incoherent reconstruction procedure, we again do not see the contour of the object as shown in Fig. 2.19(a) and Fig. 2.19(c). Whereas images from SyCM reconstruction as shown in Fig. 2.19(b) and

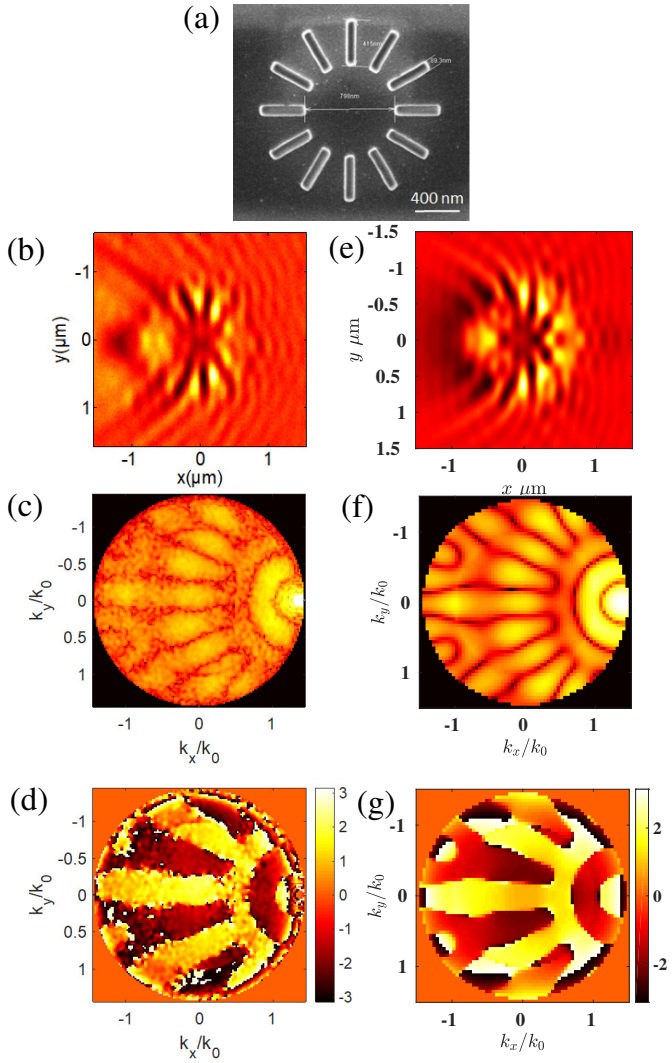

Figure 2.17 – A resin star in air deposited on a coverslip and illuminated by a TE polarized collimated beam (the incident field is directed along y) with $\theta = 68°$ that is totally reflected at the glass-air interface. (a) Electron microscope image of the sample. The left (right) column corresponds to experimental (numerical) data. (b,e) Field intensity at the image plane. (c,f) Modulus of the y component of the diffracted field at the Fourier plane. (d,g) Phase of the y component of the diffracted field at the Fourier plane.

Fig. 2.19(d), shows the interface of both the objects. Therefore the simulation suggests us that TDM in reflection configuration along with coherent reconstruction method as described in sec. 2.3.2 might be a good candidate for studying the contour of biological cell and also cell-cell interface as for example the immunological synapse.

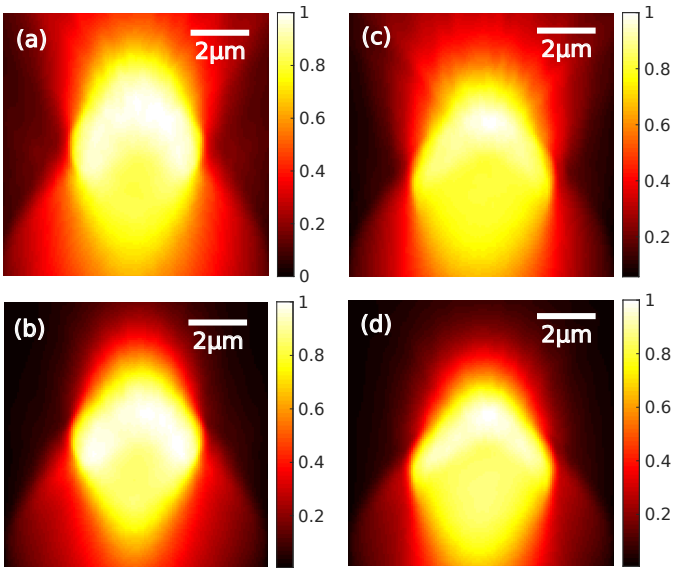

Figure 2.18 – TDM in transmission: The axial cut of reconstructed phantom cells (a) Non synapse object(incoherent reconstruction), (b) Non synapse object(SyCM reconstruction), (c) Synapse object (incoherent reconstruction), (d) Synapse object(SyCM reconstruction).

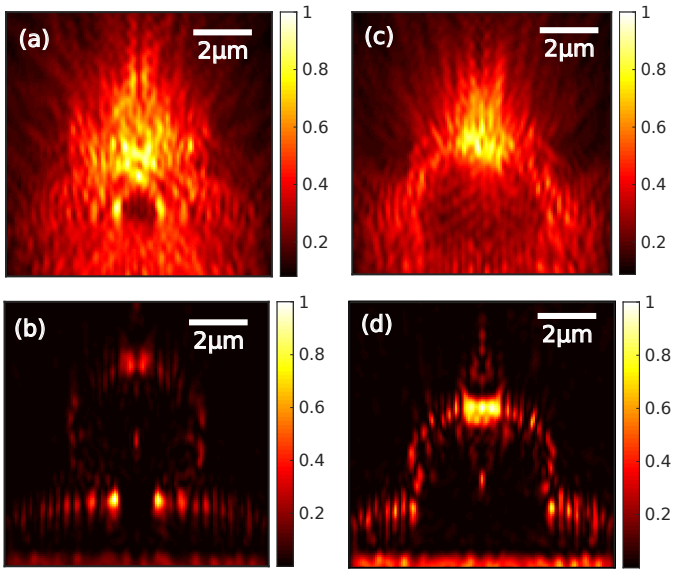

Figure 2.19 – TDM in reflection: Axial cut of reconstructed phantom cells (a) Non synapse object(incoherent reconstruction), (b) Non synapse object(SyCM reconstruction), (c) Synapse object (incoherent reconstruction), (d) Synapse object(SyCM reconstruction).

2.5 Experimental reconstruction on a reference sample

As we have seen from the reconstruction of the phantom cell, the SyCM procedure would be a good choice to detect the contour of the cell or cell-cell interface. These results were obtained from simulated data-set. Now we consider a reference sample: a reference silica bead as shown in Fig. 2.21 to compare simulated and experimental results. The beads have mean diameter 4,98 µm and refractive index 1.46 (Cat: SS05003, Bangs laboratories, Inc.) [113] are deposited on a glass lamella and is immersed in water. To have the bead fixed on the substrate, a thin Polylysine layer was used whose refractive index is similar to that of water.

2.5.1 Experimental dataset

We now launch the acquisition program as seen in Fig. 2.6 and set the laser with wavelength of $\lambda = 475$ nm. We also optimize the power ratio between the reference beam and the object beam to obtain the best contrasted fringes in the hologram. From the measurement we obtain a 3D matrix where the third dimension indicates the different illumination angles and each layer is the field scattered in far field within the numerical aperture. In this case we have used the scanning pattern as shown in Fig. 2.7(a) with 121 illumination angles arranged in a 11×11 square matrix. The data set can be used to perform a reconstruction in bright field or dark field mode as seen in Fig. 2.20. The bright spot comes from the specular reflection indicated in Fig. 2.20(A) on the interface between glass and water. It can be blocked in Fourier space as shown in Fig. 2.20(B) to obtain a dark field reconstruction with better contrast.

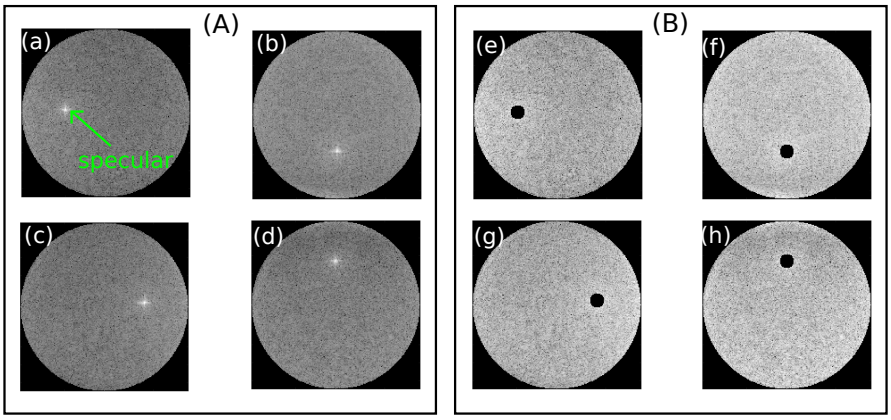

Figure 2.20 – (A) Scattered field inside the numerical aperture showing specular reflection. (B) Scattered field inside the numerical aperture showing the specular is blocked. Out of 121 illumination angles, here we have shown only 4 illumination to represent the data-set used for bright field and dark field reconstruction respectively

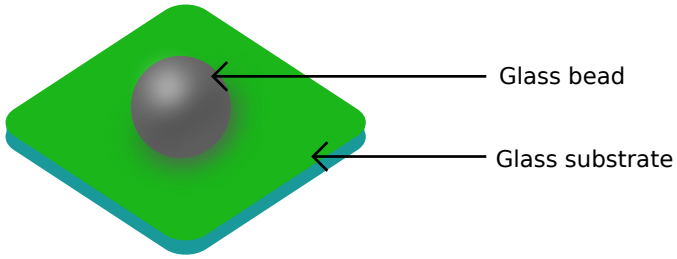

Figure 2.21 – A glass bead fixed on a glass slide and is surrounded by water: Our reference sample.

2.5.2 Synthetic dataset

With keeping the same bead as discussed in section 2.5 and with the same experimental parameters as described in subsection 2.5.1, we launch the IF-DDA program and obtain the similar holographic data-set as in subsection 2.5.1. We call this data-set as synthetic data-set.

2.5.3 Phase normalization of experimental data set

All the reconstruction procedures in Tomographic diffractive microscopy (TDM) consider that the different incident plane waves used to illuminate the sample have the same zero phase at the chosen origin of the coordinate system. This origin is usually taken at the focal point of the objective. But the mechanical and thermal drifts between successive illuminations introduce random phase shifts to each incident plane wave. A phase normalization procedure is therefore crucial to correct the data so that the phases of each illumination plane wave can be considered null at the origin. Then, forming a synthetic beam that focuses at any position is simple algebra. This normalization is based on the complex amplitude of the far-field in the specular reflected direction for each hologram. It corresponds to the reflection of the incident beam at the glass–water interface and appears as a Dirac-like peak in the Fourier plane of the microscope. We assume that this reflection is not affected by the sample. The whole signal is corrected so that the experimental specular reflection corresponds to its theoretical value. Contrarily to the transmission coefficient, which is generally always close to unity, the theoretical reflection coefficient can easily be calculated only if the glass–water interface is placed at the object focal plane (conjugated to the camera plane): it will then be equal to the Fresnel formula. However, it is seldom the case, especially if the sample is thick. In this case, the optical path of the specular reflection toward the camera, and therefore the phase of the theoretical reflection coefficient, will strongly depend on the unknown distance d between the plane of measurement and the glass–water interface and also on the illumination angle. To avoid this issue, we numerically propagate the fields to reach the glass–water interface, in this case we consider the bright field incoherent reconstruction scheme as given in

Eq.2.16. and this reconstruction is insensitive to illumination phase errors

$$I(\vec{r}) = \sum_{\vec{k_i}} \left| \sum_{\vec{k}} U_s(\vec{k}, \vec{k_i}) e^{i\vec{k}\cdot\vec{r}} \right|^2 \tag{2.16}$$

At the plane of measurement the incoherent bright field image of the bead is shown in Fig. 2.22(a). After propagating $1.1\mu m$ away from the plane of measurement we observe some sharp features that are due to some scratches or dust as shown in Fin. 2.22(b). This plane is essentially be the glass–water interface. In this way we estimate the distance, d between the plane of measurement and the glass–water interface. With this d value the measured field is propagated back to the interface and then we shift the phase of the field so that it is equal to the argument of the reflection coefficient at the specular position.

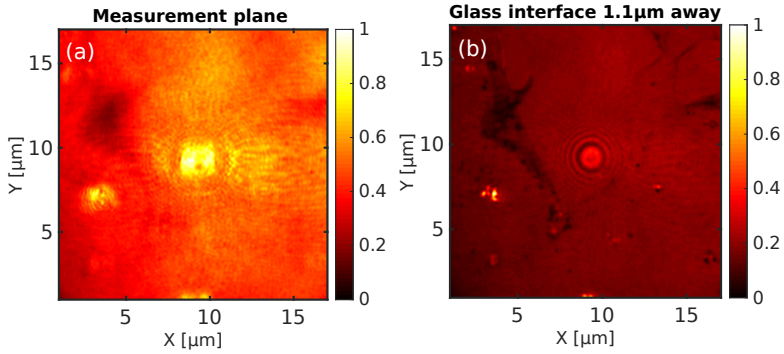

Figure 2.22 – Estimation of the distance between plane of measurement and glass-water interface: (a) Bright field incoherent reconstruction of the bead at the plane of measurement, (b) Bright field incoherent reconstruction of the bead at the glass-water interface

2.5.4 Reconstruction of the bead

From the dataset as obtained from the experiment as discussed in subsection 2.5.1 and the simulation as discussed in subsection 2.5.2, we apply the image reconstruction method as discussed in section 2.3. The bright field and dark field incoherent reconstructions of the glass microsphere are shown in Fig. 2.23. They mainly retrieve the sides of the sphere, but not the top and bottom parts.

Now, we have considered the coherent dark field reconstruction method as our standard reconstruction method as this methods shows good potential in the reconstruction of the contour of the phantom cell from the synthetic dataset 2.4.5.

The reconstructed images are shown in Fig. 2.24(a) and Fig. 2.24(b) as obtained from the simulated and experimental data set respectively. The reconstructed bead from the experimental data set does not corresponds to that of as obtained from the synthetic data set. There might be a problem to the experimental data-set. It has been shown that the phase normalization to the experimental data is very important

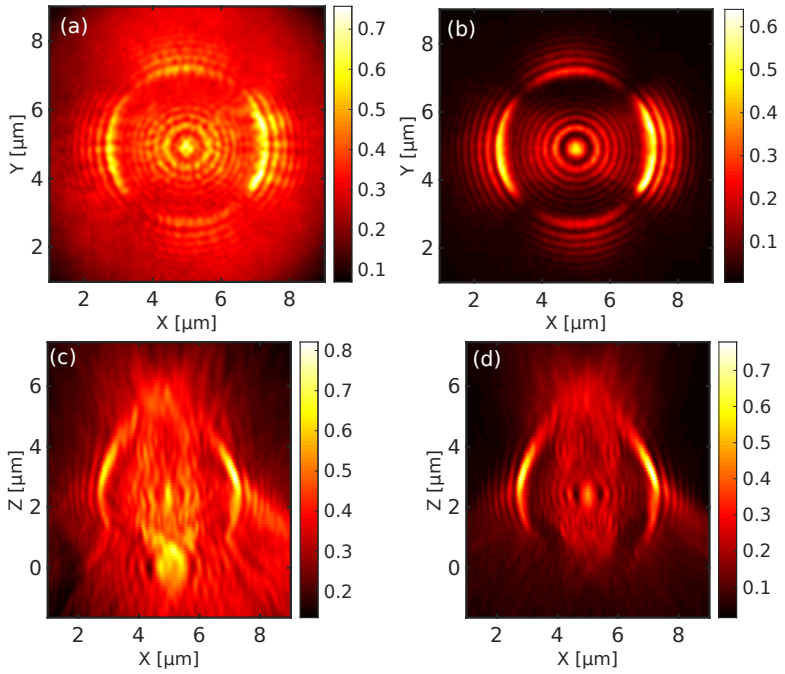

Figure 2.23 – (a-b) Transverse cuts of incoherent reconstructions for a glass bead immersed in water (c-d) Axial cuts (xz cut), (a,c) Corresponds to the incoherent bright field reconstruction; (b,d) Corresponds to incoherent dark field reconstruction.

which permits to focus inside the water without being disturbed by the aberrations at the glass-water interface, contrarily to a standard confocal microscope. Once the phase normalization is done in the experimental data-set of the reference bead, we again perform the image reconstruction and the reconstructed bead is now shown in Fig. 2.24(c). This image now corresponds better to the image as obtained form the synthetic data (see Fig. 2.24(a)).

From the above discussion we can infer few things (1): The TDM in reflection is capable of detecting the contour of object in micrometer range, (2) We have to perform phase normalization to the experimental data set by finding proper distance between the plane of measurement and the glass–water interface.(3) The reconstructions are performed in dark-field mode, by filtering out the specular reflection in the Fourier space for each hologram. As a result, the glass–water interface cannot be seen. This is an important advantage over classical confocal microscopy, as this interface produces a strong signal that masks that scattered by the sample and corrupts the 3D reconstruction(see Fig. 2.24(d)). Another advantage is that the 2D angular scans in SyCM (121 illumination angles here) can be performed in a quicker way than the 3D position scans of standard confocal microscopy (typically more than 10^5 positions required).

Here, our concern was to obtain similar SyCM reconstructions between theory and experiment on a reference sample. The fidelity of the reconstructed contour is not the

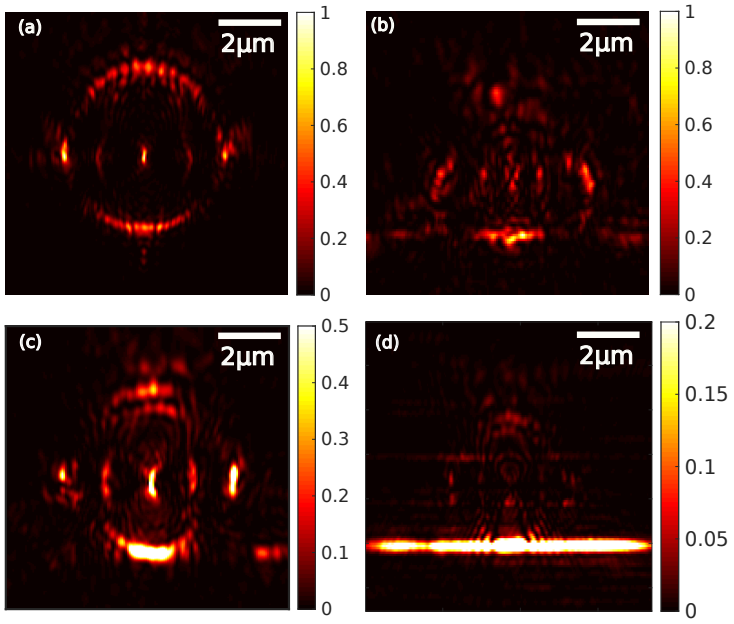

Figure 2.24 – (a) Axial cuts of SyCM intensity reconstructions for a glass bead immersed in water: (a) simulated data, (b) experimental data without the correct phase normalization, (c) experimental data with the correct phase normalization. Color scale has been readjusted on (c) for visualization purpose and (d) Bright field SyCM reconstruction of the bead: here we only see the bright interface, not the bead

issue, as the glass bead contrast is far higher than for cells, making Born approximation not adapted. We will now move on for doing experiment on true biological cells, which is the subject of the next chapter.

3 Experimental results obtained with our reflection TDM set-up

In this chapter, we are going to present the coherent image reconstruction (as described in section 2.3.2) of biological sample from the experimental data set as obtained by reflection TDM. First, we have considered a single effector T cell [114] as our sample. Then we will study with reflection TDM, two important steps of immune response namely phagocytosis and the immunological synapse. And finally the preliminary result of the reconstruction of a glass bead will be presented from mirror assisted TDM where the data from both reflection and transmission type of TDM were combined targeting to include the low spatial frequencies from the transmission TDM and thereby hoping for better reconstruction.

3.1 Sample preparation

In all our experiment, glass slide having dimension (24 mm × 24 mm) (CS-S24-100, Microscope central) was used. Glass slides were cleaned in a piranha bath (70% H_2SO_4, Sigma aldrich, France, and 30% H_2O_2 50% solution, Sigman Aldrich, France) for 10 minutes then rinced with 5 liters of deionized water. Poly-L-Lysin (100 µg/mL) in PBS) was deposited and incubated for 20 minutes, then rinsed in PBS. Glutardaldehyde solution (2.5% in 0.1M borate buffer at pH=9.5) was deposited then incubated for 20 minutes, then rinsed in PBS. A mix of Fc-ICAM (10 µg/mL) and SDF-alpha (4 µg/mL) (both from R&D Systems, USA) in PBS was deposited and incubated for 30 minutes then rinsed in PBS. A blocking solution of 1% BSA in PBS was added up to the slide. The slide was then mounted and sealed on a reusable metal petri dish and filled with cell culture medium. All the samples used in the experiment were prepared by Philippe Robert from Laboratoire Adhésion et Inflammation(LAI), Hôpital de la Conception, Marseille.

3.2 Synthetic confocal microscopy applied to biological samples

3.2.1 Reconstruction of an effector lymphocyte

We have examined the ability of SyCM to image a biological cell. We considered human effector T lymphocytes, deposited on a glass lamella coated with adhesion

molecules ICAM-1, and then fixed by a treatment with paraformaldehyde at 4%. Effector T cells migrate on ICAM-1 substrates with a strongly polarized shape. Their central and front parts are strongly adherent and spread, while their rear part forms a partially detached tail, called uropod [115].

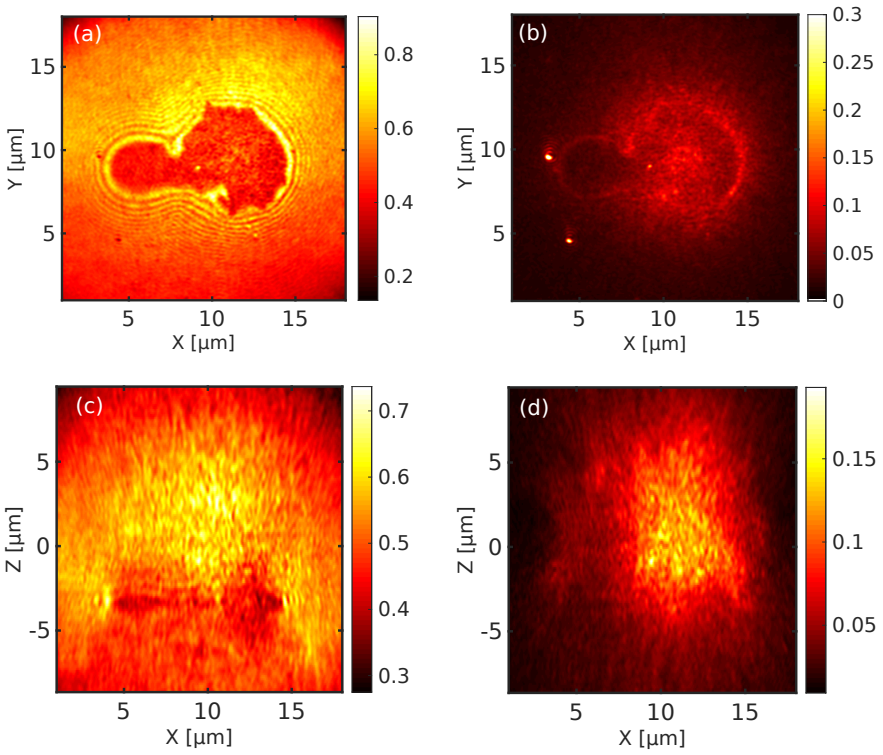

Figure 3.1 – Reflection intensity incoherent reconstruction of a human effector T lymphocyte: (a) Transverse cut (bright field). (b) Transverse cut (dark field), (c) Axial cut (bright field) and (d) Axial cut (dark field). Along the axial direction, the glass-water interface is at (z axis), z = −3 µm.

The transverse and axial cut of the bright field and dark field incoherent reconstruction of the T cell is shown in Fig. 3.1. As discussed in section 2.3.1 and as expected from Fig. 2.19(a) and (c), here also the incoherent modality of reconstruction fails to reconstruct in 3D the effector cell. Fig. 3.2 shows the coherent 3D reconstruction obtained on one of such T cells: the central body on the right and the uropod on the left can be clearly identified [111]. The central body appears filled with numerous inhomogeneities in comparison with the uropod. This can be explained by the fact that the central body contains the nucleus where highly compacted DNA is bound to produce refractive index changes stronger than anywhere else in the cell. The bottom and top membranes of the cell are also clearly retrieved on the axial cut Fig. 3.2(a), showing the high sectioning capability of reflection SyCM. An axial resolution about 400 nm can be evaluated from the full width at half-maximum of the signal profile Fig. 3.2(b) when crossing these membranes, close to the effective wavelength of illumination of 357 nm in water.

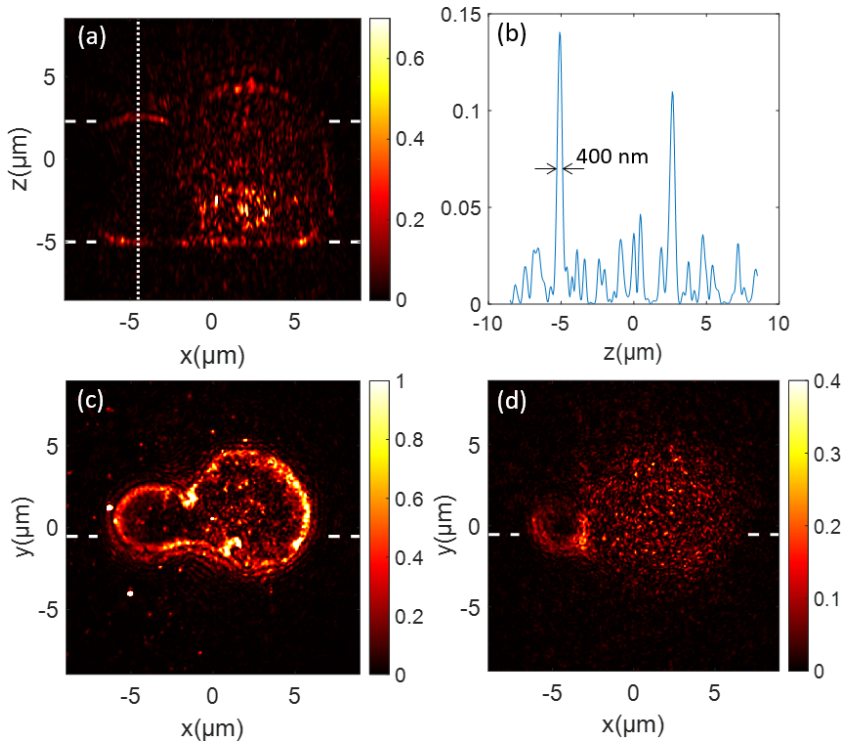

Figure 3.2 – Reflection SyCM intensity reconstruction of a human effector T lymphocyte: (a) axial cut along dashed white segments of (c); (b) intensity profile along vertical dotted white line of (a); (c) and (d) transverse cuts along white dashed segments of (a) at z = −5 µm (glass interface position), and at z = −2,3 µm , respectively. Color scale has been readjusted on (a) and (d) for visualization purpose.

3.2.2 Application of SyCM to detect phagocytosis

3.2.2.1 Reconstruction of phagocyted beads

From the result of effector T-cell, we have seen that the boundary of the cell is clearly visible in the transverse image (Fig. 3.2(c) and also the top and bottom boundary of the cell are seems to be detectable. In the next step towards the study of T-cell activation is to distinguish the phagocytosis process and finally the detection of immunological synapse. Phagocytose is one of the key process of natural immune response. In brief we can say that the pathogen is first eaten by the phagocyte and then presented to T-cell for initiating immune response. In order to identify this phenomenon of phagocytose, we have considered antigen coated microspheres as a model of pathogen. The reason for this is that the bead is highly contrasted and might be easier to identify inside the cell if the bead is phagocyted.
Microspheres were made of glass and having diameter of 5 µm (Bangs Laboratoreis, USA), cleaned by sonication in 2% Hellmanex-III (an alkaline soap) solution for 30 minutes at 50 °C then three cycles of centrifugation and resuspension in ultrapure

water for rinsing. Coating was done by incubation in a 1 mg/mL solution of human IgG (Tegellines, courtesy of Pharmacie Centrale, Hôpital de la Conception, Marseille). IgG are recognized by activating antibodies Fc fragment receptors natively present on monocyte such as CD16 and CD32, triggering phagocytosis. As a model of human monocyte, THP-1 ware used. THP-1 cell line are a lineage of cells from a leukemia with monocytic differenciation. These cells were obtained from Sigma-Aldrich [116] and were cultivated in RPMI-1640 medium supplemented with glutamine, penicillin and streptomycin.

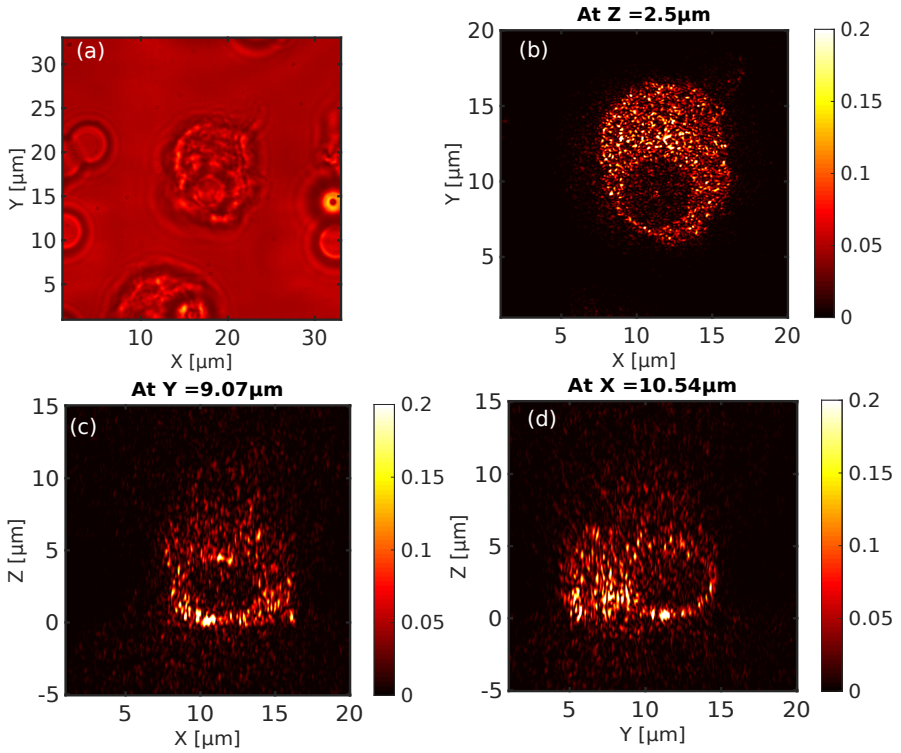

Figure 3.3 – Reflection SyCM intensity reconstruction of a bead phagocyted cell: (a) Bright field transmission intensity image as reference, (b) Transverse cut of the reconstruction (c) xz axial cut, (d) yz axial cut. z = 0 µm corresponds to the glass-water interface

A standard bright field image in transmission of the cell is shown in Fig. 3.3(a). The bright field transmission image was obtained in our TDM setup by illuminating the sample from top by while light with a Halogen lamp light source(Illuminators)(Fort imaging system, GLI-154). In the image, a round shape object is visible suggesting the possible location of the bead. Even though this is the bead, from the bright field image, we can not say whether the bead is inside the cell or just sitting on top of the cell. Now if we look the transverse section of the SyCM reconstruction as in Fig. 3.3(b), we see a round shape void space of around 5 µm which indicates that this is clearly the bead. When we look the axial cut as shown in Fig. 3.3(c) and Fig. 3.3(d) in xz plane and yz plane respectively, the void space is also present which confirms

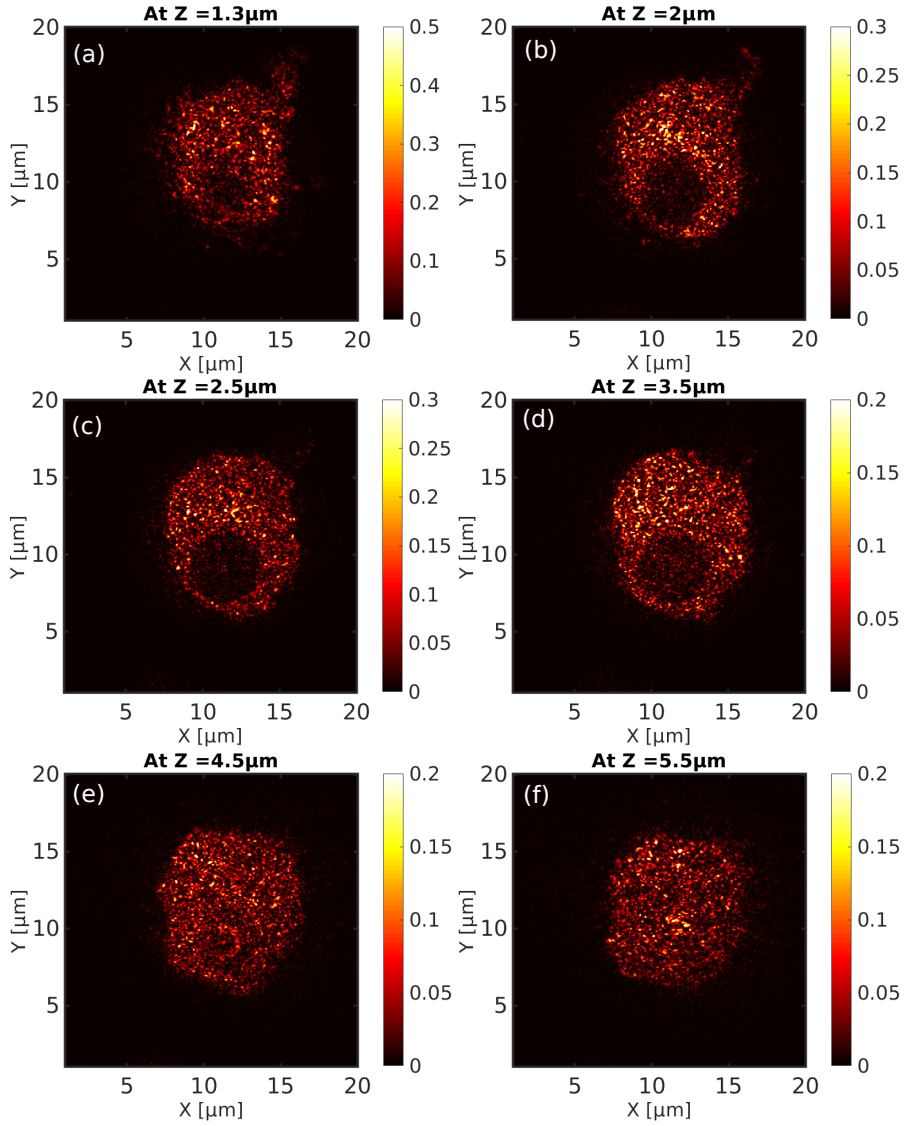

Figure 3.4 – Reflection SyCM intensity reconstruction of a bead phagocyted cell at different z positions. The global intensity gradually decreases as we go further away from the interface (z = 0 µm being the glass-water interface). For this reason, the color scale of the images are adjusted for better visualization.

that the bead has truly been phagocyted by the cell. It becomes more visible, if we observe the images in transverse cut as obtained in different z-position as shown in Fig. 3.4. Close to the glass-water interface (i.e z = 0 being the interface) we begin to see the void space as in Fig. 3.4(a) and this void space becomes more prominent as we progress from z = 2 µm to z = 2,5 µm. As we progress even more the vacancy is being to diminished and is completely absent if the diameter if the bead is crossed which is indicated is Fig. 3.4(f).

We carried out similar experiment on another phagocyte of the sample. Here in the

bright field transmission image in Fig. 3.5(a), we clearly see a bright hot spot on top of the cell which is a bead since the bead has higher refractive index than the biological cell. But again this bright field image does not give any indication if the bead is inside the cell. If we now look the TDM 3D reconstruction of the bead we see the void space in both transverse as in Fig. 3.5(b) and axial cuts as shown in Fig. 3.5(c-d).

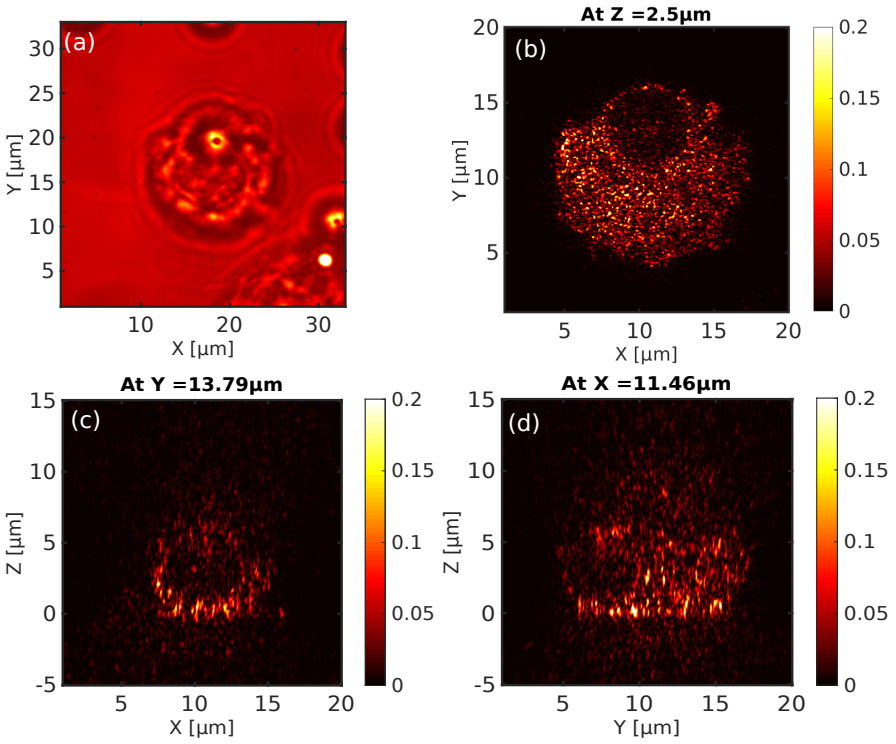

Figure 3.5 – Reflection SyCM intensity reconstruction of a bead phagocyted cell: (a) Bright field transmission intensity image as reference, (b) Transverse cut of the reconstruction (c) xz axial cut, (d) yz axial cut. z = 0 µm corresponds to the glass-water interface position

Again if we observe the transverse images as shown in Fig. 3.6 at different axial position as obtained from the 3D reconstruction of the cell , close to the glass-water interface (i.e z = 0 µm being the interface) we do not see any void space as in Fig. 3.6(a) but with increasing z value the void space appears and with even higer value of z it is completely disappeared as in Fig. 3.6(f). This confirms that the bead is indeed inside the cell.

By using the above discussed method, it is possible to study the phagocytosis process for different combinations of antigens and phagocytes. The only added steps in this method is we need to label the glass bead with proper antigen to be studied, and then we look the location of the bead inside the cell from the 3D reconstruction. If the bead is found inside the cell we say that particular antigen was phagocyted. This method is already interesting to test if a specific antigen is prone to launch an immune response. We have checked that if no antigen is coated on the glass beads, they are

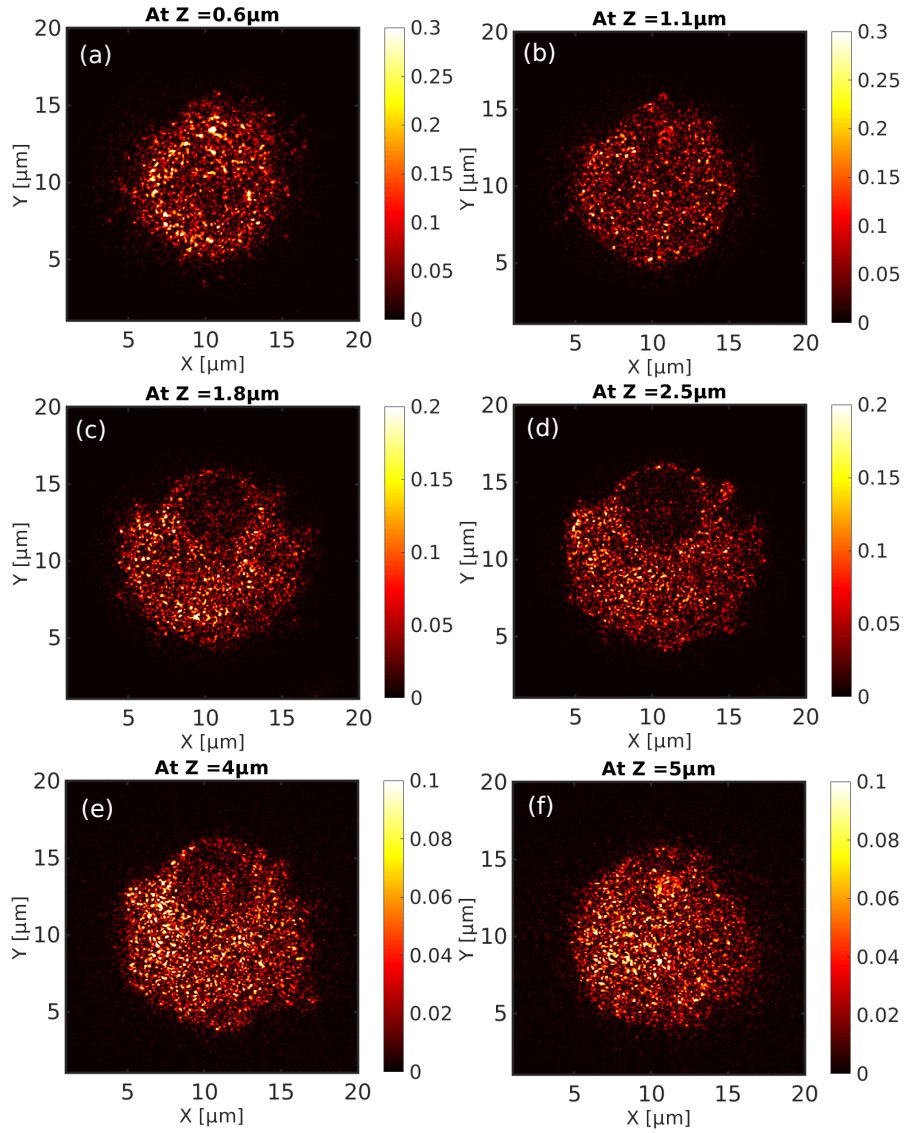

Figure 3.6 – Reflection SyCM intensity reconstruction of a bead phagocyted cell at different z positions. The global intensity gradually decreases as we go further away from the interface (z = 0 µm being the glass-water interface). For this reason, the color scale of the images are adjusted for better visualization.

not phagocyted. The method remains however an indirect method, as in practice phagocytosis is performed on a foreign cell, such as bacteria. In the next section we will explore if our experimental approach can be used to a phagocyted bacteria.

3.2.2.2 Phagocytosis of bacteria

We have conducted experiment on two different combination of samples to study phagocytosis namely monocyte-bacteria and monocyte-yeast where monocyte acts

as phagocyte. Here we focus on bacteria, which are typical cells concerned by phagocytosis. The reconstructed images of monocyte-bacteria sample is shown in Fig. 3.7. The sample was prepared with Escherichia coli bacteria which are known to launch the phagocytosis process. From the bright field image, Fig. 3.7(a), the monocyte is clearly visible. The shape of the monocyte is round and nearly 10 µm of diameter. From the bright field image, we do not clearly see the bacteria. While the coherent dark field reconstruction, we see the rod like structure which are effectively the bacteria as shown in Fig. 3.7(b-c). Further away from the interface (at 5 µm) as shown in Fig. 3.7(d), only the monocyte is visible while the bacteria are not. There might be some bacteria inside the cell but from our reconstruction we do not see them properly due to fact that the contrast is almost similar for both the bacteria and the monocyte. The axial cut of the reconstruction as in Fig. 3.7(e-f) shows dimension of the monocyte and bacteria along the axial direction. The bacteria is enclosed with white. The axial cut also does not give us any information whether a bacteria is inside or not.

3.2.2.3 Reconstruction of monocyte and yeast

As the bacteria are quite small and with similar contrast as the monocyte, we have tried the monocyte-yeast combination. Saccharomyces cerevisiae were used as a model for yeasts(courtesy of Patrick Chames, CRCM). Saccharomyces cerevisiae is a species of yeast (single-celled fungus microorganisms). The species is very common and used in baking and brewing for long and also most common type of fermentation is caused by this microorganism. It is one of the most intensively studied eukaryotic model organisms in molecular and cell biology, much like Escherichia coli as the model bacterium. S. cerevisiae cells are round to ovoid and the diameter is around 5 µm to 10 µm [117]. Yeasts were cultivated on agar coated plates at 4 °C for long term conservation, and in medium at 30 °C under agitation for expansion.
This particular sample is chosen as reference to image the different type of biological cells side by side, and see their contrast and size (here the monocytes are not activated and phagocytosis cannot be launched). The bright field transmission image of the sample is shown in Fig. 3.8(a). The monocyte is approximately three times larger in size as compared to the yeast. The yeast is round shape and looks like glass bead as in Fig. 3.3(a). This particular site was chosen because all the cells are quite isolated. The transverse cut of the coherent reconstruction at the interface (z = 0 µm) is shown in Fig. 3.8(b). Here we see that the monocyte is flat and two bright spots enclosed in white circle, close by to the monocyte. As we go to different axial position (z = 1 µm), the contrast of the monocyte is higher than the yeast giving us the indication that there is a difference of contrast between different biological cells. Further away from the glass interface (Fig. 3.8(d) we only see the monocyte. This confirms that the thickness of the monocyte is higher than the yeast. In the axial cut of the reconstruction as in Fig. 3.8(e) and in Fig. 3.8(f) we can easily see the round yeast cells close to the monocyte. From this measurement, it is seen that yeasts have a smaller contrast and are more homogeneous than monocytes, which indicates phagocytosis might be visible with SyCM.

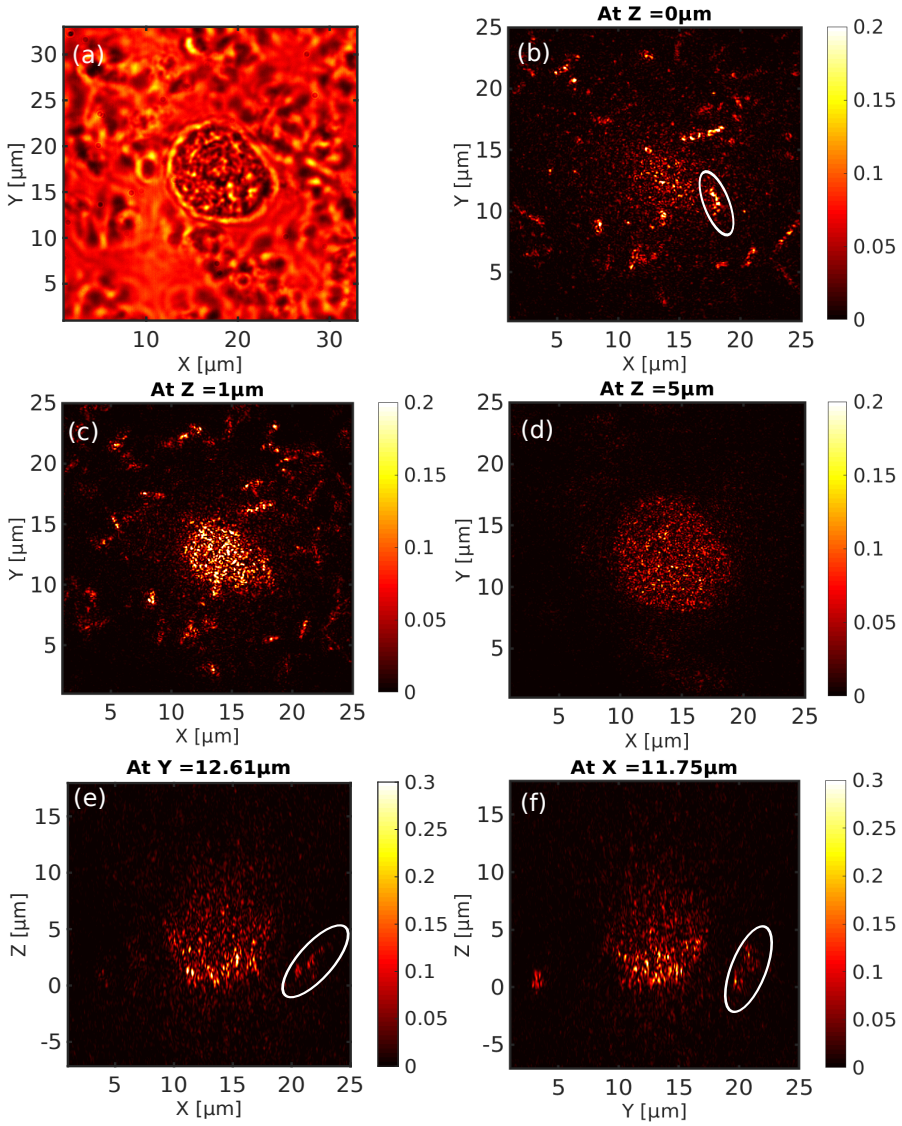

Figure 3.7 – Reflection SyCM intensity reconstruction of a monocyte and bacteria: (a) Bright field transmission intensity image as reference, (b-d) Transverse cut of the reconstruction at different axial position (e) xz axial cut, (f) yz axial cut. z = 0 µm corresponds to the glass-water interface.

3.2.3 Characterization of the immunological synapse

Preparation of immunological sample

For synapses assays, peripheral blood mononuclear cells (PBMC) were harvested from donor blood obtained from etablissement Français du Sang following french bioethic laws by centrifugation gradient followed by freezing at −80 °C in Dimethyl sulfoxide (DMSO). Prior to each experiement, a vial of PBMC was thawed, then cells were cultured for 24h in RPMI 1640 medium suplemented with 10% foetal calf serum,

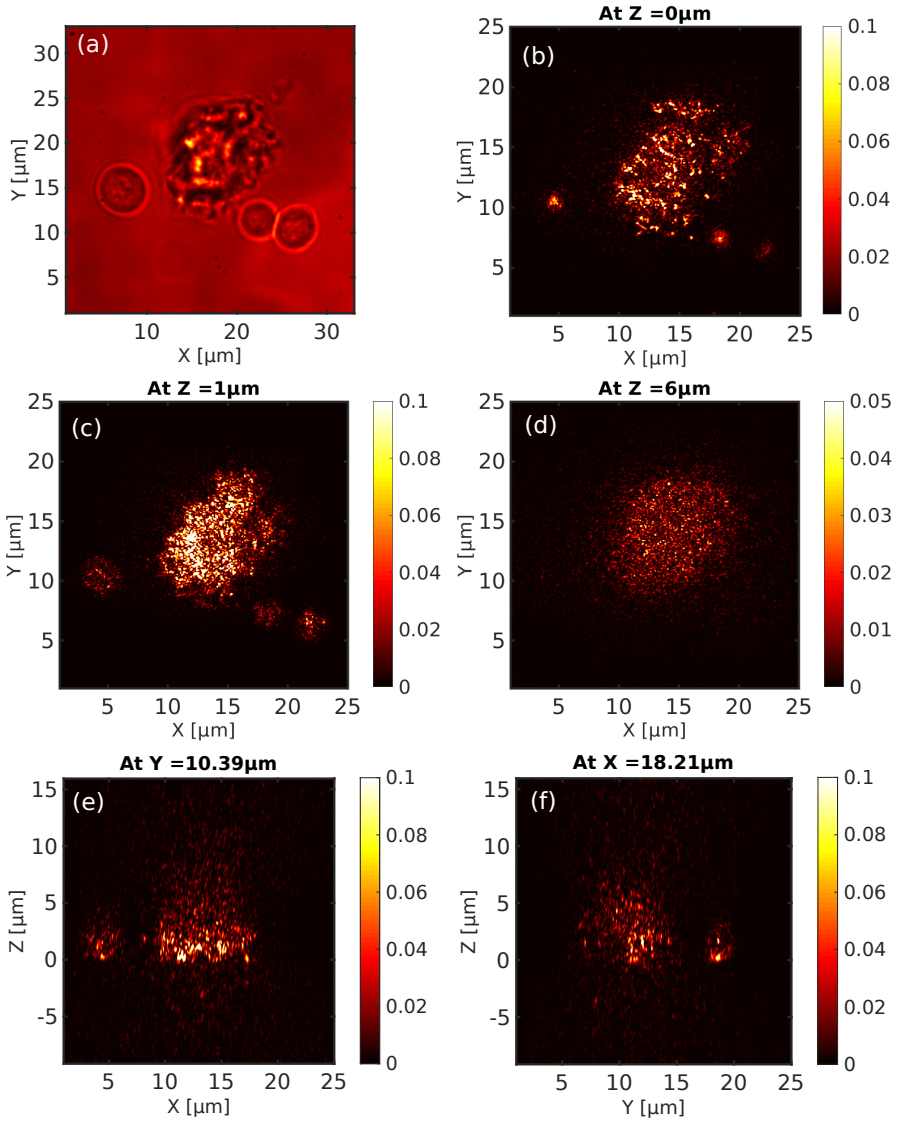

Figure 3.8 – Reflection SyCM intensity reconstruction of a monocyte and yeast cell: (a) Bright field transmission intensity image as reference, (b-d) Transverse cut of the reconstruction at different axial position (e) xz axial cut, (f) yz axial cut. z = 0 µm corresponds to the glass-water interface. The color scale in the images are adjusted for better visualization.

penicillin, streptomycin and glutamine (all chemicals and culture products are from Sigma Aldrich, Germany). Surfaces allowing leukocyte migration were prepared as follows: 24 mm × 24 mm coverslides were cleaned in a piranha solution, as described above, then 200 µL of a solution of poly-L-Lysin at 100 µg/mL in phosphate buffer (0.02M, pH7.4) was deposited for 20 minutes, under agitation. Coverslides were rinsed thouroughly in PBS then 200 µL of glutardaldehyde solution (2.5% in borate buffer, pH 9.5, 0.1M) was deposited for 20 minutes; then glass slides were rinsed thoroughly in PBS, then incubeted in a solution of Fc-ICAM (10 µg/mL) and SDF-alpha (2 µg/mL)

(both R&D systems, USA) for 30 minutes under agitation. After a last thorough rinsing with PBS, a blocking solution of 0.1% BSA and 0.2M glycin in PBS was deposited for 20 minutes. Coverslides were mounted in individual open chambers, the one million of PBMC in a volume of 500 µL of culture medium was deposited on each chamber. For controls, cells were incubated in 5% CO_2 at 37 °C for 2 hours prior to fixation; for assays enterotoxin A from Staphylococcyus aureus (Sigma Aldrich) was added to reach 2 µg/mL, cells being incubated in the same conditions. For fixations, formaledhyde solution in water was added to reach 4%. Chambers were closed with tape then kept at 4 °C. Cell migration was observed for 5 minutes every 30 minutes during the 2 hours incubation on an Olympus CK40 inverted microscope (Olympus, Japan) in a home-made thermoregulated box equipped with a CCD camera (IDS, Germany).

SyCM reconstructions

We have carried out experiment on two sets of samples in order to study the immunological synapse. In the control sample, the T-cell(leucocyte) is placed on top of the antigen presenting cell (APC). Here no synapse was formed as in the sketch shown in Fig. 2.12(a). The TDM reconstruction of the sample is shown in Fig. 3.9(b-f). In the bright field image, we can not distinguish the T-cell and the APC as in Fig. 3.9(a), whereas we clearly see the APC in the trasverse image at the interface (Fig. 3.9(b)). As we move further away from the interface we see a small round shap T-cell with encircled with white on top of APC shown in Fig. 3.9(c-d). From the axial cut (Fig. 3.9(e-f)) we clearly see the top and bottom membrane of the APC and on top of APC the T-cell is also seen even though the boundary of the T-cell is not clearly reconstructed.

In the assay sample, in which the necessary conditions were applied during the sample preparation so that the T-cell and antigen presenting cell (APC) should form the immunological synapse at their interface as in the schematic shown in Fig. 2.12(b). The target location for the experiment is shown in the bright field image (Fig. 3.9(a)). At the interface, the APC is clearly seen from the 3D coherent reconstruction. At z = 1 µm, we lose the contour of the APC but begin to see the T-cell enclosed by white circle. Further away from the glass interface as in Fig. 3.10(d), we still see the T-cell on top of APC and also another two T-cells are visible in the top left corner of the image. If we see the axial cut to the location of the T-cell which is on top of the APC as shown in Fig. 3.10(f), we see the bottom and top membrane of the APC and also the T-cell is clearly seen. We also see higher contrast at the interface between APC and T-cell. This could be the immunological synapse. But again due to over speckled 3D reconstruction of the specimen, it is not conclusive that this is an immunological synapse. After this reconstruction two questions arise. Is there an immunological synapse has formed where we performed the measurement? Is our reconstruction technique sensitive enough to detect it?

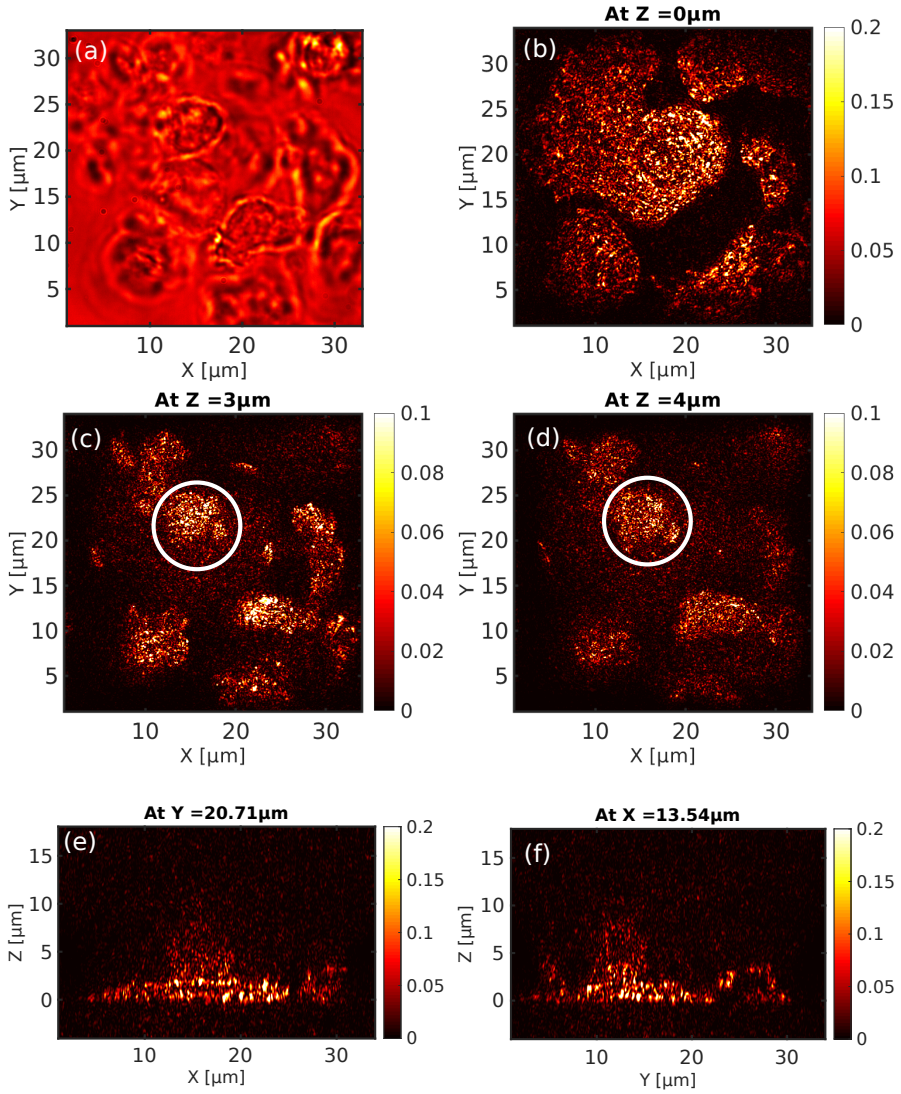

Figure 3.9 – Reflection SyCM intensity reconstruction of Antigen presenting cell and T-cell: (a) Bright field transmission intensity image as reference, (b-d) Transverse cut of the reconstruction at different axial position (e) xz axial cut, (f) yz axial cut. z = 0 µm corresponds to the glass-water interface. The color scale in the images are adjusted for better visualization.

3.2.4 Fluorescence measurement of immunological synapse

As posed in the previous section, to answer the first question, new samples were prepared where the cells were tagged with Alexa fluorophores (excitation wavelength at 488 nm). If the synapse was formed then the fluorophores concentrate to the synapse site otherwise they are uniformly distributed to the cell. We have carried out the bright field transmission and fluorescence measurements on a separate epi-fluorescence microscopy set-up where the source has a sufficient power for fluores-

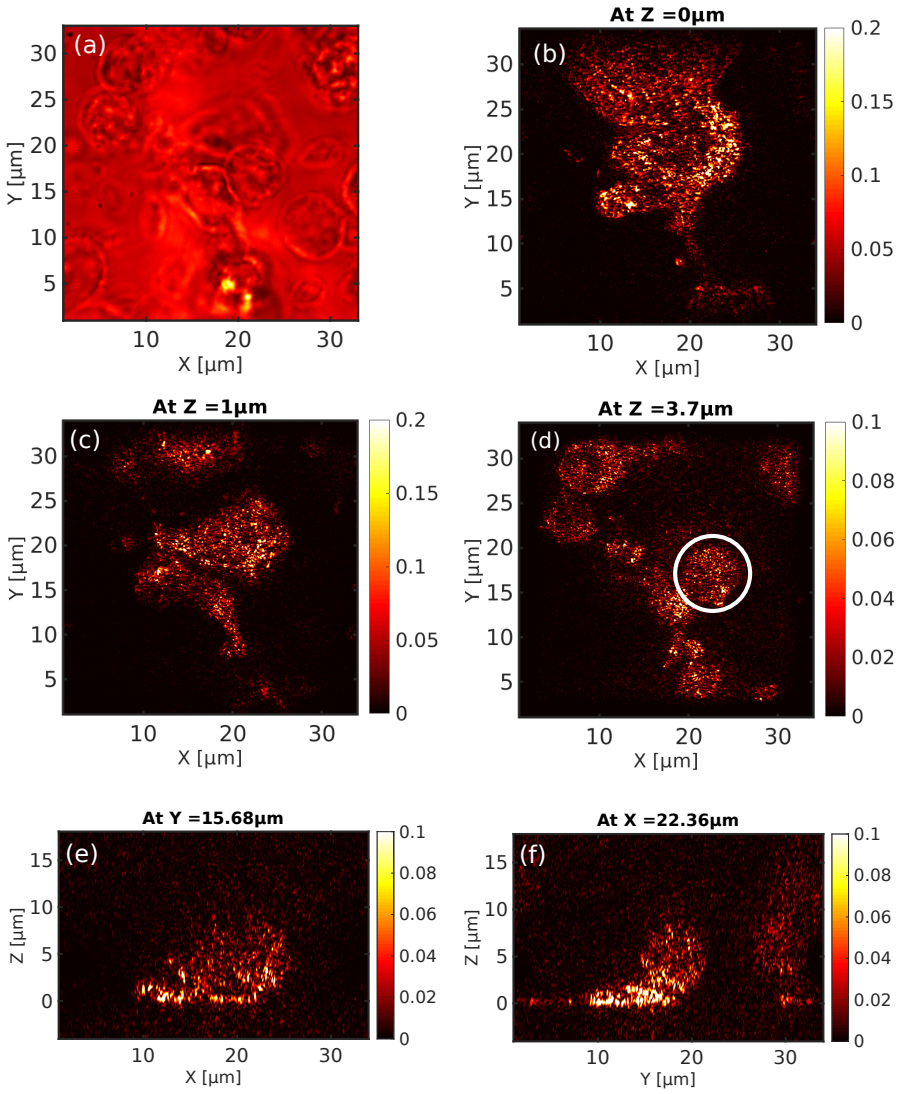

Figure 3.10 – Reflection SyCM intensity reconstruction of Antigen presenting cell and T-cell: (a) Bright field transmission intensity image as reference, (b-d) Transverse cut of the reconstruction at different axial position (e) xz axial cut, (f) yz axial cut. z = 0 µm corresponds to the glass-water interface. The color-map in the images are adjusted for better visualization.

cence detection (Oxxius laser diode, 50 mW power at 488 nm). On the assay sample we have selected several locations from bright field transmission measurements where the immunological synapse could appear (one or several T cells in close vicinity to an antigen presenting Cell). The resulting images are presented in Fig. 3.11 where the images in the first column Fig. 3.11(a,c,e) are the bright field transmission images and the corresponding fluorescent measurement is shown in Fig. 3.11(b,d,f) respectively. Out of this three measurements only one measurement shown in Fig. 3.11(f) is compatible with the gathering of the fluorophores due to the formation of the immunological

synapse which is appearing as a bright strip. This shows that on the assay sample not all cell locations lead to the formation of the synapse.

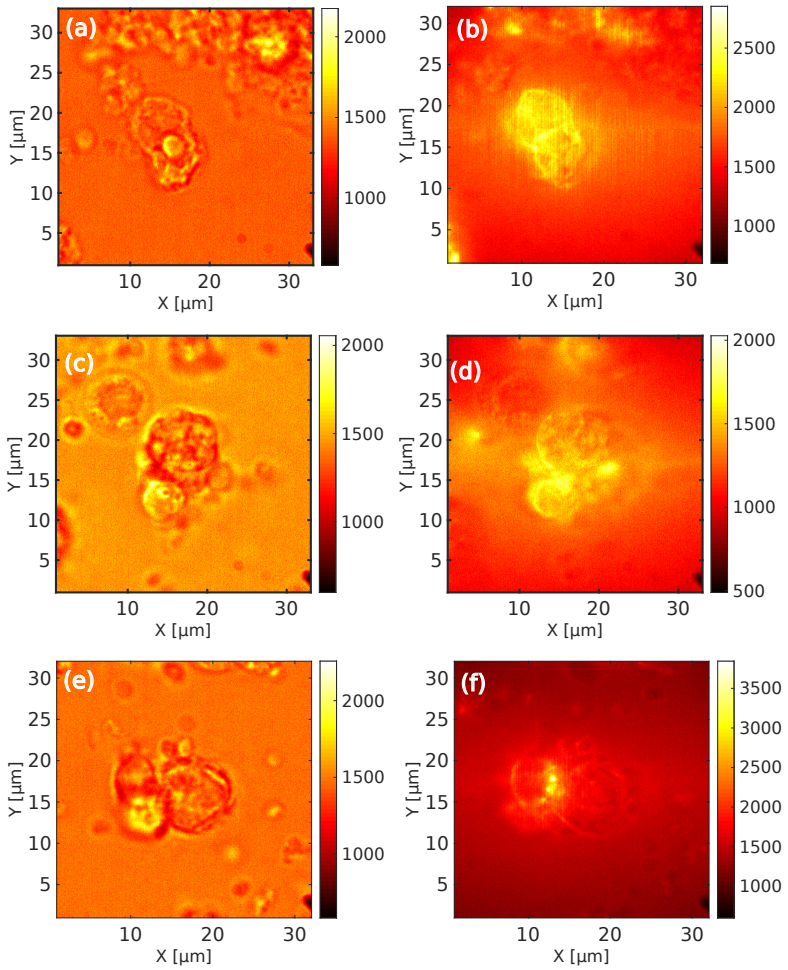

Figure 3.11 – Images of different cell aggregates on the synapse assay sample: (a, c, e) Bright field transmission; (b, d, f) the respective epifluorescence images; Only the fluorescence image (f) is compatible with the presence of a synapse.

Therefore a TDM measurement on a random cell might not guarantee that the measurement was conducted on the proper location. It would be more efficient to conduct the fluorescent and TDM measurements with the same setup. If the fluorescent measurement shows the indication of synapse then a subsequent TDM measurement can be carried out to make sure that we have obtained good data for the further reconstruction of the immunological synapse. Proper working conditions have now been found on our TDM set-up to be compatible with fluorescence detection, and new synapse samples are expected to test the combination of fluorescence and tomographic measurements.

3.3 Mirror assisted TDM

3.3.1 Principle

In the previous section, we have seen that our reflection TDM is capable of identifying the contour of a T cell and a phagocyted bead within a cell. But as we try to identify phagocyted bacteria or the immunological synapse our approach does not presently seem concluding. This can be due to the severely speckled reconstructed reconstruction of the sample resulting from the lack of the contribution from the lower spatial frequencies. As we already know that the TDM in transmission provides the access to the lower spatial frequencies and contributes to the volume reconstruction of the object, by combining both TDM in reflection and TDM in transmission might be an approach from experimental point of view for obtaining less speckled images and thereby helping to identify the phagocyted cell or the immunological synapse. A potential method in line of combining both TDM in reflection and transmission is mirror assisted TDM. The theoretical foundation of mirror assisted tomography is found at E. Murdy et al. [118] and with numerical simulation it has shown that the isotropic resolution[58] is better for the mirror assisted TDM setup in comparison to either reflection TDM and transmission TDM when considered individually[118]. A rigorous study both in theory and experiment on mirror assisted TDM is done by L. Foucault et al. [119], where the sample is deposited on a specially prepared glass slide, coated with aluminum and a 6 µm polystyrene passivation layer. Here aluminum the mirror plays the role of second objective lens and this mirror assisted TDM is equivalent to 4Pi microscopy. In the work of mirror assisted tomography by L. Foucault et al. [119], the object was reconstructed by considering only the transmitted signal from both sides of the sample while the back scattered signals was neglected.

In our case, we put the sample on a standard transparent glass slide (CS-S24-100, Microscope central) which is inserted in a specific home-made metallic chamber as shown in Fig. 3.12 housing a mirror (PF10-03-P01, Thorlab). It is placed at around 50 µm to 60 µm away from the glass slide and the chamber is filled with water. The cross section of the metallic chamber is shown in Fig. 3.13.

3.3.2 Synthetic results

We first show with synthetic data what is the best theoretical attainable gain permitted by mirror-assisted TDM compared to transmission TDM for volume reconstruction. We present in Fig. 3.14 the OTF obtained for transmission TDM and mirror assisted TDM. In mirror assisted TDM we basically combine both reflection TDM and transmission TDM while using a reflection TDM experimental setup. The OTF is generated by considering an objective lens with numerical aperture of 0.95 and the wavelength is λ = 475 nm and 317 illumination directions are considered. As we see in the combined OTF (Fig. 3.14(b), the accessible axial frequency response is improved. The improvement is clearly visible if we consider the SyCM intensity reconstructions for these two configurations (reconstruction of a perfect point object). For TDM in

Figure 3.12 – Metal housing of the sample for mirror assisted TDM: (a) Top view, (b) Bottom view

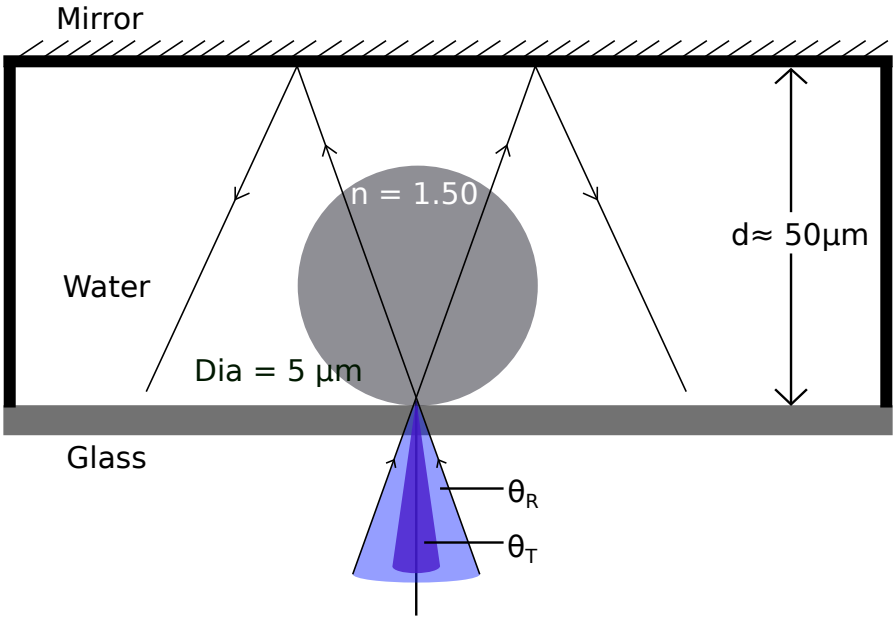

Figure 3.13 – The model of mirror assisted tomography: A way to combine both the reflection and transmission TDM

transmission only, the axial cut of the reconstruction as in Fig. 3.15(b) is elongated along Z-axis which causes image blurring and potentially reduces the axial resolution. Whereas the axial cut of the reconstruction for mirror assisted TDM is more symmetric. In this case both the transverse cut and the axial cut are similar. (Fig. 3.15(c) and Fig. 3.15(d)) suggest that quasi-isotropic resolution could be achieved. The mirror assisted TDM will surely contribute to the volume reconstruction of sample with improved axial resolution.

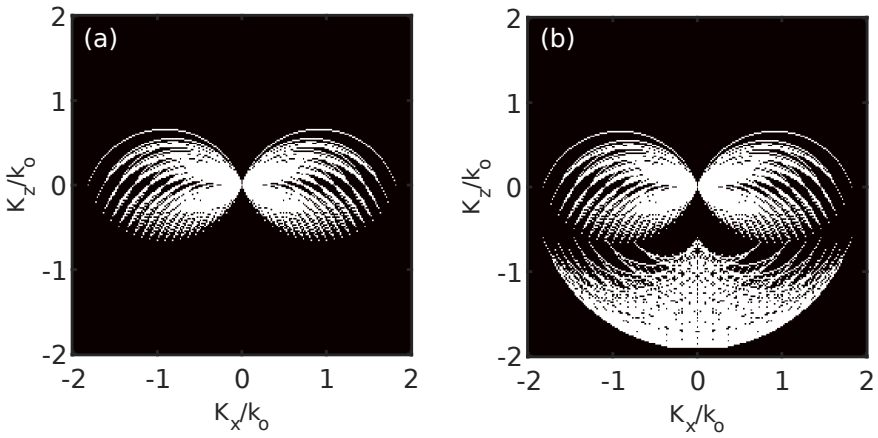

Figure 3.14 – The axial section of the 3D OTF for (a) Reflection TDM (b) Combined trasmission and reflection TDM. The wavelength $\lambda = 475$ nm, numerical aperture, NA = 0.95 with 317 illumination angles were used

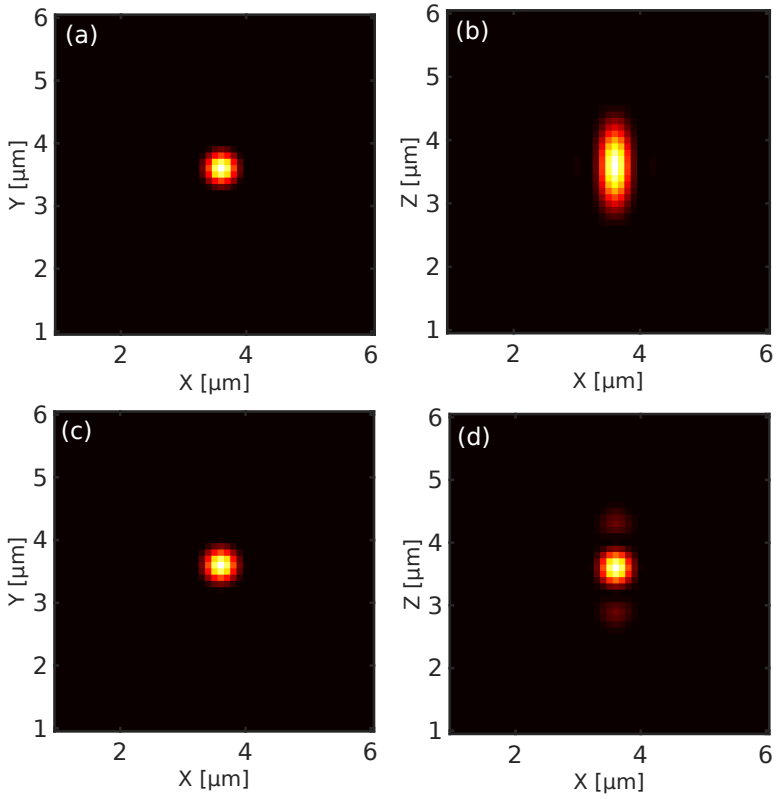

Figure 3.15 – SyCM intensity reconstructions for a perfect point object (a) Transverse cut for TDM in transmission (b) Axial cut for TDM in transmission; (c,d) Same when the transmission and reflection TDM are combined

3.3.3 Preliminary experimental results

As the sample is now covered with mirror, the light reflected back from the mirror also illuminate the sample mimicking the implementation of transmission TDM. The data acquisition is performed in two steps. The first step is the usual reflection TDM which we already have discussed in the previous chapter. In the second step, we record the contribution from the transmission TDM. Here the optical path length of the reference beam is gradually increased and at some point the scattered light from the sample due to the reflection from the mirror interfere with the reference beam. The incident illumination with higher polar angle do not make their way back to the objective lens once reflected back by the mirror. Only the incident light within the solid cone indicated in dark color as in Fig. 3.13 contributes to the formation of hologram. In our particular setup and sample holder, it is found nearly $\theta_T = 10°$, half of the solid angle.

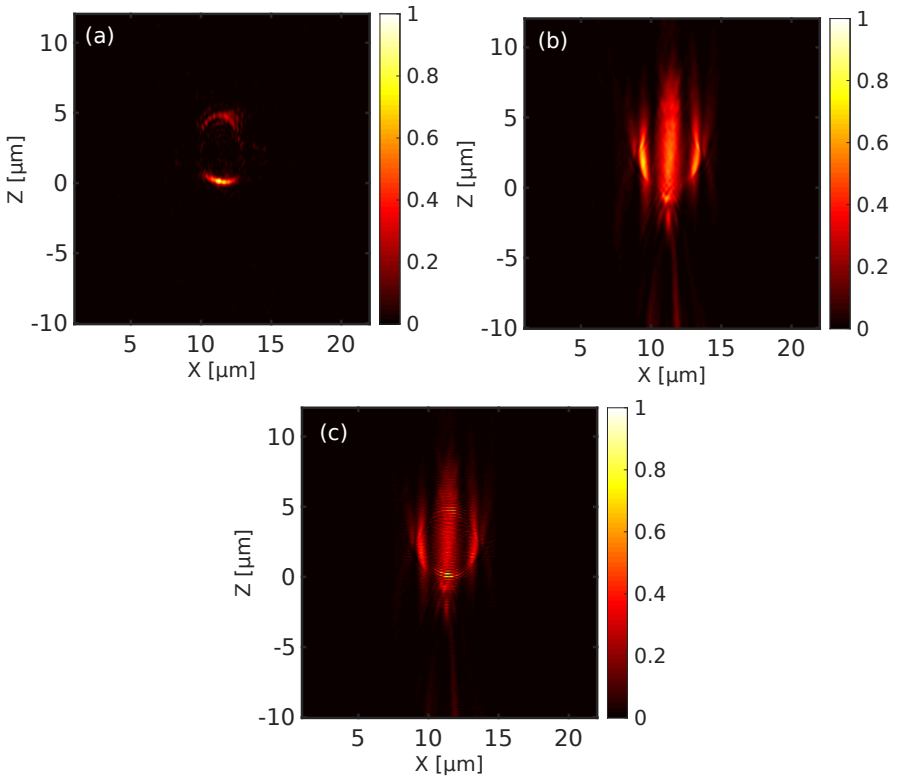

Figure 3.16 – Preliminary experimental results of mirror assisted tomography:(a) Reconstruction of a glass bead with reflection TDM only (b) with transmission TDM only (c) With combined data

The axial section of SyCM intensity reconstructions of the bead for both reflection TDM and transmission TDM is shown in Fig. 3.16(a) and Fig. 3.16(b) respectively. We clearly see the top and bottom interface of the bead from the reflection TDM, this result to which we are already familiar with from the experimental reconstruction of the reference bead sample in the previous chapter. Whereas the image as obtained

from transmission TDM, gives the side view of the bead and a beginning of its volume. When these two dataset are combined, the round shape of the bead appears more visible as shown in Fig. 3.16(c) despite the fact that only few illumination angles (only 12 illumination in this case) are used in transmission TDM. It is sufficient to obtain an improvement in the reconstruction. While adding these two images, we add the complex reconstructions (field) directly in image space and after taking the square of absolute value we obtained the combined SyCM intensity reconstruction as in Fig. 3.16(c).

3.3.4 Further improvement of mirror assisted TDM

Here we have explored a limited configuration of mirror assisted TDM. In this case the angle coverage(θ_T) for transmission TDM is small. The value of θ_T could be increased by placing the mirror closer to the sample. There is another possibility for increasing θ_T by changing the conjugation plane of the beam steering mirror on the object path. Generally the galvano mirror is conjugated to the glass-water interface at the sample irrespective to the illumination direction. If the conjugation plane could be shifted closer to the mirror, the overall transmission angle will be increased.

Conclusion

The discovery of x-rays and subsequent development of computed tomography revolutionized the medical diagnosis. In computed tomography (CT) image a 3D view of the organ is reconstructed from the x ray absorption profile of the organ by the help of computer with appropriate inversion algorithm. In line to this, efforts are ongoing for developing faster, efficient and risk free imaging tools intended to find applications in bio-medical diagnosis. As for example in immunology, a lot of diseases signatures can be detected by looking the presence of immunological synapse between two different type of immune cells known as antigen presenting cell and T -cell. A faster and marker free detection of this immunological synapse could mean saving lives. From optical point of view, the synapse is an interface between two different biological cells and since the synapse has a unique morphology with the presence of certain type of proteins, it also might pose a difference of refractive index between the native cells and the interface and could be detected optically.

In this thesis the applicability of tomographic diffractive microscopy (TDM) in reflection configuration on finding the contour or cell-cell interface has been explored for immunological applications. As we know that the interface or contour/edge information of an object is encoded to the high spatial frequency, therefore a suitable imaging system having high spatial axial frequency response is necessary to reconstruct the boundary of the object or the interface between two different objects. TDM in reflection configuration has this feature of providing high axial frequency response. Experimentally, TDM is like a off-axis digital holography and computationally it is like the well known computed tomography (CT). In TDM, the object is illuminated by plane wave with varying the angle of incidence and the diffracted field from the sample is measured. For the 3D reconstruction from the scattered field, the TDM set-up is used as a synthetic confocal microscope (SyCM). It permits to obtain a 3D confocal intensity reconstruction in dark field mode and without any aberrations produced at the glass-water interface. In this work all the reconstructions are intensity profile of the sample which are presented in all the figures. Here the purpose is not to reconstruct different organelles inside the cell rather finding the boundary of the cell or the interface between two cells.

As all of the samples that we have used are in water medium, it was necessary to put the sample holder (see the schematic of the setup) in vertical orientation and due to this, mechanical vibration was increased. This instability is not good for holographic measurement. The optimization of the sample holder was then carried out by reducing the mechanical path lenght between the sample holder and the objective lens to ameliorate the vibration effect. Before going to the experiment on biological cells, the TDM setup was calibrated by considering a reference sample, i.e

a glass bead with diameter of 5 µm. The reconstruction of a glass micro-sphere was carried out from the experimental data and synthetic data. Both reconstructions were then compared and found satisfactorily congruent. The synthetic scattered field of the bead was obtained from a home made discrete dipole approximation (DDA) program where TDM in reflection was implemented.

After optimization and calibration of the experimental setup, several immunological cells and immunological phenomenon were studied. In the first step, the contour of a single effector human T cell was reconstructed with proper identification of the cell in transverse direction. The top and bottom boundary of the cell was also recognized. Then, the phagocytosis process was studied. Antigen coated glass bead was conditioned to be phagocted by a monocyte. The bead location was identified and confirmed by TDM reflection measurement that the bead was inside the monocyte. Cell inside cell, bacteria are allowed to be phagocyted by monocyte, this time the result from the reconstitution was not conclusive that the bacteria was indeed phagocyted. New samples allowing to observe the phagocytosis of yeast cells are expected to validate the interest of TDM to detect this process on cells.

Identifying immunological synapse with TDM in reflection raised some concern. Did we have a sample with fully developed immunological synapse? To convince ourselves a new batch of samples are being prepared where a fluorescent dye will be added and if the synapse is formed properly then the dye will migrate to the synapse location. Our TDM setup has already showed the capability to measure fluorescent signals with considerable efficiency. Once confirmed the existence of the immunological synapse from the fluorescent measurement, the TDM in reflection measurement will be carried out on that particular location and see what the reconstruction provides.

In the end, for the first time to the best of our knowledge biological cells in solution were successfully explored in this work by TDM in reflection. It has permitted the reconstruction of the contour of cells with a higher axial resolution than TDM in transmission. However,The 3D reconstructions obtained so far relied on Born approximation. It does not take into account the distortion induced by the sample on the incident waves (the multiple scattering), which can corrupt the reconstructions and degrade the resolution. The sizes and contrasts of the cells we have studied in this work are not well adapted to Born approximation. Future work will therefore focus on using rigorous iterative inversion algorithm that take into account multiple scattering to improve the reconstructions [111].

Besides, the volume reconstruction of TDM in reflection is not good as compared to TDM in transmission. A combination of TDM in reflection and TDM in transmission has been explored by placing a mirror on top of the sample. With this preliminary configuration, only limited number of illumination makes their way back to the objective after reflected from the mirror. Here the target sample was a bead and the contribution from transmission data improved the reconstruction when compared with the reflection data only. This combined scheme could also be implemented for biological sample to ameliorate the reconstruction with an improved configuration.

Bibliography

[1] Adam J M Wollman et al. “IX. An account of Mr. Leeuwenhoek’s microscopes”. In: *Open Biol.* 5.4 (2015). ISSN: 0261-0523. DOI: 10.1098/rstl.1739.0085 (cit. on p. 27).

[2] Gerd Binnig and Heinrich Rohrer. “Scanning Tunneling Microscopy—from Birth to Adolescence”. In: *Rev. Mod. Phys.* 59.3 (1987), pp. 615–625. ISSN: 15213773. DOI: 10.1002/anie.198706061 (cit. on p. 27).

[3] Paul K. Hansma and Jerry Tersoff. “Scanning tunneling microscopy”. In: *J. Appl. Phys.* 61.2 (1987). ISSN: 00218979. DOI: 10.1063/1.338189 (cit. on p. 27).

[4] D. McMullan. “Scanning electron microscopy 1928–1965”. In: *Scanning* 17.3 (1995), pp. 175–185. ISSN: 19328745. DOI: 10.1002/sca.4950170309 (cit. on p. 27).

[5] G Binnig, C. F Quate, and Ch. Gerber. “Atomic Force Microscope”. In: *Phys. Rev. Lett.* 56.9 (1986), pp. 930–933. DOI: 10.1201/9781420075250 (cit. on p. 27).

[6] Bonnie O. Leung and Keng C. Chou. “Review of super - Resolution fluorescence microscopy for biology”. In: *Appl. Spectrosc.* 65.9 (2011), pp. 967–980. ISSN: 00037028. DOI: 10.1366/11-06398 (cit. on p. 27).

[7] Samuel T. Hess, Thanu P.K. Girirajan, and Michael D. Mason. “Ultra-high resolution imaging by fluorescence photoactivation localization microscopy”. In: *Biophys. J.* 91.11 (2006), pp. 4258–4272. ISSN: 00063495. DOI: 10.1529/biophysj.106.091116 (cit. on p. 27).

[8] Travis J. Gould, Vladislav V. Verkhusha, and Samuel T. Hess. “Imaging biological structures with fluorescence photoactivation localization microscopy”. In: *Nat. Protoc.* 4.3 (2009), pp. 291–308. ISSN: 17542189. DOI: 10.1038/nprot.2008.246 (cit. on p. 27).

[9] Bo Huang et al. “Whole-cell 3D STORM reveals interactions between cellular structures with nanometer-scale resolution”. In: *Nat. Methods* 5.12 (2008), pp. 1047–1052. ISSN: 15487091. DOI: 10.1038/nmeth.1274 (cit. on p. 27).

[10] Xiaowei Zhuang. “Nano-imaging with STORM”. In: *Nat. Photonics* 3.7 (2009), pp. 365–367. ISSN: 17494885. DOI: 10.1038/nphoton.2009.101 (cit. on p. 27).

[11] Rainer Heintzmann and Thomas Huser. “Super-Resolution Structured Illumination Microscopy”. In: *Chem. Rev.* 117.23 (2017), pp. 13890–13908. ISSN: 15206890. DOI: 10.1021/acs.chemrev.7b00218 (cit. on p. 27).

[12] Stefan W. Hell and Jan Wichmann. "Breaking the diffraction resolution limit by stimulated emission: stimulated-emission-depletion fluorescence microscopy". In: *Opt. Lett.* 19.11 (1994), p. 780. ISSN: 0146-9592. DOI: 10.1364/ol.19.000780 (cit. on p. 27).

[13] Thomas A. Klar et al. "Fluorescence microscopy with diffraction resolution barrier broken by stimulated emission". In: *Proc. Natl. Acad. Sci.* 97.15 (2000), pp. 8206–8210. ISSN: 00278424. DOI: 10.1073/pnas.97.15.8206 (cit. on p. 27).

[14] Birka Hein, Katrin I Willig, and Stefan W Hell. "Stimulated emission depletion (STED) nanoscopy of a fluorescent protein-labeled organelle inside a living cell". In: *Proc. Natl. Acad. Sci.* 105.38 (2008), pp. 14271–14276. ISSN: 0386-2151. DOI: 10.1007/978-3-540-72993-8_29 (cit. on p. 27).

[15] David Huang et al. "Optical Coherence Tomography". In: *Science (80-.).* 254.5035 (1991), pp. 1178–1181. ISSN: 1522726X (cit. on p. 27).

[16] Arnaud Dubois et al. "Ultrahigh resolution full field OC tomography". In: *Appl. Opt.* 43.14 (2004), pp. 2874–2883 (cit. on p. 27).

[17] Arnaud Dubois. *Handbook of full-field optical coherence microscopy, technology and applications.* 1st. Singapore: Pan Stanford Publishing Pte. Ltd, 2016, pp. 1–51. ISBN: 9789814669160 (cit. on p. 27).

[18] Wolfgang Drexler et al. "Ultrahigh-resolution ophthalmic optical coherence tomography". In: *Nat. Med.* 7.4 (2001), pp. 502–506. ISSN: 10788956. DOI: 10.1038/86589 (cit. on p. 27).

[19] M. Weinigel et al. "In vivo histology: Optical biopsies with chemical contrast using clinical multiphoton/coherent anti-Stokes Raman scattering tomography". In: *Laser Phys. Lett.* 11.5 (2014). ISSN: 1612202X. DOI: 10.1088/1612-2011/11/5/055601 (cit. on p. 27).

[20] John K.C. Chan. "The wonderful colors of the hematoxylin-eosin stain in diagnostic surgical pathology". In: *Int. J. Surg. Pathol.* 22.1 (2014), pp. 12–32. ISSN: 10668969. DOI: 10.1177/1066896913517939 (cit. on p. 27).

[21] Michael Titford. "The long history of hematoxylin". In: *Biotech. Histochem.* 80.2 (2005), pp. 73–78. ISSN: 10520295. DOI: 10.1080/10520290500138372 (cit. on p. 27).

[22] Emil Wolf. "Three-dimensional structure determination of semi-transparent objects from holographic data". In: *Opt. Commun.* 1.4 (1969), pp. 153–156. ISSN: 00304018. DOI: 10.1016/0030-4018(69)90052-2 (cit. on pp. 28, 39, 43).

[23] V. Lauer. "New approach to optical diffraction tomography yielding a vector equation of diffraction tomography and a novel tomographic microscope". In: *J. Microsc.* 205.2 (2002), pp. 165–176. ISSN: 00222720. DOI: 10.1046/j.0022-2720.2001.00980.x (cit. on pp. 28, 49, 54).

[24] O. Haeberlé et al. “Tomographic diffractive microscopy: Basics, techniques and perspectives”. In: *J. Mod. Opt.* 57.9 (2010), pp. 686–699. ISSN: 09500340. DOI: 10.1080/09500340.2010.493622 (cit. on pp. 28, 43).

[25] Wonshik Choi et al. “Tomographic phase microscopy”. In: *Nat. Methods* 4.9 (2007), pp. 717–719. ISSN: 15487091. DOI: 10.1038/nmeth1078 (cit. on p. 28).

[26] Myung K. Kim. “Principles and techniques of digital holographic microscopy”. In: *SPIE Rev.* 1.1 (2010), p. 018005. ISSN: 1947-7988. DOI: https://doi.org/10.1117/6.0000006. URL: http://photonicsforenergy.spiedigitallibrary.org/article.aspx?doi=10.1117/6.0000006 (cit. on pp. 28, 54).

[27] Ichirou Yamaguchi. “Phase-shifting digital holography”. In: *Opt. Lett.* 22.16 (1997), pp. 1268–1270 (cit. on p. 28).

[28] August Köhler. “New Method of Illumination for Photomicrographical Purposes”. In: *J. R. Microsc. Soc.* 14 (1894), pp. 261–262 (cit. on pp. 30, 64).

[29] Christoph Cremer and Barry R. Masters. “Resolution enhancement techniques in microscopy”. In: *Eur. Phys. J. H* 38.3 (2013), pp. 281–344. ISSN: 21026459. DOI: 10.1140/epjh/e2012-20060-1 (cit. on p. 31).

[30] George Biddell Airy. “On the Diffraction of an Object-glass with a Circular Aperture”. In: *Trans. Cambridge Philos. Soc.* 5.August (1834), pp. 283–291. ISSN: 1050-0529. URL: http://adsabs.harvard.edu/abs/1835TCaPS...5..283A (cit. on p. 32).

[31] Colin J. R. Sheppard et al. “Interpretation of the optical transfer function: Significance for image scanning microscopy”. In: *Opt. Express* 24.24 (2016), p. 27280. ISSN: 1094-4087. DOI: 10.1364/oe.24.027280 (cit. on p. 37).

[32] D. A. Tichenor and J. W. Goodman. “Coherent Transfer Function*”. In: *J. Opt. Soc. Am.* 62.2 (1972), p. 293. ISSN: 0030-3941. DOI: 10.1364/josa.62.000293 (cit. on p. 37).

[33] Joseph W Goodman. *Introduction to Fourier Optics*. 2nd editio. New York: The McGraw-Hill Companies, Inc., 1996, p. 441. ISBN: 0974707724. DOI: 10.1088/1355-5111/8/5/014. arXiv: 0070242542. URL: http://stacks.iop.org/1355-5111/8/i=5/a=014?key=crossref.ad20ea108e8f625cb0486bf680f74198 (cit. on p. 38).

[34] Ulrich Kubitscheck. *Fluorescence Microscopy: From Principles to Biological Applications*. Weinheim: Wiley-Blackwell, 2013. ISBN: 9783527329229. DOI: 10.1002/9783527671595.ch5 (cit. on p. 38).

[35] K. R. Spring and M. W. Davidson. *Nikon Microscopy*. https://www.microscopyu.com/techniques/fluorescence/introduction-to-fluorescence-microscopy. June 2021 (cit. on p. 38).

[36] Malte Renz. “Fluorescence microscopy-A historical and technical perspective”. In: *Cytom. Part A* 83.9 (2013), pp. 767–779. ISSN: 15524930. DOI: 10.1002/cyto.a.22295 (cit. on p. 38).

[37] Lothar Schermelleh, Rainer Heintzmann, and Heinrich Leonhardt. "A guide to super-resolution fluorescence microscopy". In: *J. Cell Biol.* 190.2 (2010), pp. 165–175. ISSN: 00219525. DOI: 10.1083/jcb.201002018 (cit. on p. 38).

[38] L. Song et al. "Photobleaching kinetics of fluorescein in quantitative fluorescence microscopy". In: *Biophys. J.* 68.6 (1995), pp. 2588–2600. ISSN: 00063495. DOI: 10.1016/S0006-3495(95)80442-X. URL: http://dx.doi.org/10.1016/S0006-3495(95)80442-X (cit. on p. 38).

[39] Richard Kasprowicz, Rakesh Suman, and Peter O'Toole. "Characterising live cell behaviour: Traditional label-free and quantitative phase imaging approaches". In: *Int. J. Biochem. Cell Biol.* 84 (2017), pp. 89–95. ISSN: 18785875. DOI: 10.1016/j.biocel.2017.01.004. URL: http://dx.doi.org/10.1016/j.biocel.2017.01.004 (cit. on p. 39).

[40] F. Zernike. "Phase contrast, a new method for the microscopic observation of transparent objects". In: *Physica* 9.7 (1942), pp. 686–698. ISSN: 00318914. DOI: 10.1016/S0031-8914(42)80035-X (cit. on p. 39).

[41] Lang Walter. "Nomarski differential interference-contrast microscopy". In: *Zeiss Inf.* 70 (1968), pp. 114–120. ISSN: 15214141. DOI: 10.1002/eji.1830111014 (cit. on p. 39).

[42] Pierre Marquet et al. "Digital holographic microscopy: a noninvasive contrast imaging technique allowing quantitative visualization of living cells with subwavelength axial accuracy". In: *Opt. Lett.* 30.5 (2005), pp. 468–470. ISSN: 0146-9592. DOI: 10.1364/ol.30.000468 (cit. on p. 39).

[43] Avinash C. Kak and Malcom Slaney. *Principles of Computerized Tomographic Imaging*. IEEE Press, 1988, p. 327 (cit. on pp. 41–43, 49, 64).

[44] Tyler S. Ralston et al. "Interferometric synthetic aperture microscopy". In: *Nat. Phys.* 3.2 (2007), pp. 129–134. ISSN: 17452481. DOI: 10.1038/nphys514 (cit. on p. 42).

[45] C. W. McCutchen. "Generalized Aperture and the Three-Dimensional Diffraction Image". In: *J. Opt. Soc. Am. A* 54.2 (1964), pp. 240–244. ISSN: 1084-7529. DOI: 10.1364/josaa.19.001721 (cit. on p. 43).

[46] Max Born and Emil Wolf. *Principles of Optics*. 7th. Cambridge University Press, 1999 (cit. on p. 43).

[47] L. Cutrona et al. "Synthetic aperture radars: A paradigm for technology evolution". In: *IRE Trans. Mil. Electron.* 5 (1961), pp. 127–131 (cit. on p. 43).

[48] Didier Massonnet and Jean-Claude Souyris. *Imaging with Synthetic Aperture Radar*. First edit. EPFL Press, 2008. ISBN: 9782940222155. DOI: 10.1117/3.2186106.ch49 (cit. on p. 43).

[49] Alberto Moreira et al. "A tutorial on synthetic aperture radar". In: *IEEE Geosci. Remote Sens. Mag.* 1.1 (2013), pp. 6–43. ISSN: 21686831. DOI: 10.1109/MGRS.2013.2248301 (cit. on p. 43).

[50] Arkadiusz Kuś et al. “Tomographic phase microscopy of living three-dimensional cell cultures”. In: *J. Biomed. Opt.* 19.04 (2014), p. 046009. ISSN: 1083-3668. DOI: 10.1117/1.jbo.19.4.046009 (cit. on pp. 46, 51).

[51] Yu Chih Lin and Chau Jern Cheng. “Sectional imaging of spatially refractive index distribution using coaxial rotation digital holographic microtomography”. In: *J. Opt.* 16.6 (2014), p. 8. ISSN: 20408986. DOI: 10.1088/2040-8978/16/6/065401 (cit. on p. 46).

[52] Yu-chih Lin et al. “Optically driven full-angle sample rotation for tomographic imaging in digital holographic microscopy”. In: *Opt. Lett.* 42.7 (2017), pp. 1321–1324. ISSN: 0146-9592. DOI: 10.1364/ol.42.001321 (cit. on pp. 46, 48).

[53] Seungwoo Shin et al. “Active illumination using a digital micromirror device for quantitative phase imaging”. In: *Opt. Lett.* 40.22 (2015), pp. 5407–5410. ISSN: 0146-9592. DOI: 10.1364/ol.40.005407 (cit. on p. 46).

[54] Julianna Kostencka et al. “Holographic tomography with scanning of illumination: space-domain reconstruction for spatially invariant accuracy”. In: *Biomed. Opt. Express* 7.10 (2016), pp. 4086–4101. ISSN: 2156-7085. DOI: 10.1364/boe.7.004086 (cit. on p. 46).

[55] Yongjin Sung et al. “Optical diffraction tomography for high resolution live cell imaging”. In: *Opt. Express* 17.1 (2009), p. 266. ISSN: 1094-4087. DOI: 10.1364/OE.17.000266. URL: https://www.osapublishing.org/oe/abstract.cfm?uri=oe-17-1-266 (cit. on p. 46).

[56] M. Debailleul et al. “High-resolution three-dimensional tomographic diffractive microscopy of transparent inorganic and biological samples”. In: *Opt. Lett.* 34.1 (2009), pp. 79–81. ISSN: 0146-9592. DOI: 10.1364/ol.34.000079 (cit. on pp. 46, 49, 54).

[57] Bertrand Simon et al. “High-resolution tomographic diffractive microscopy of biological samples”. In: *J. Biophotonics* 3.7 (2010), pp. 462–467. ISSN: 1864063X. DOI: 10.1002/jbio.200900094 (cit. on p. 46).

[58] Bertrand Simon et al. “Tomographic diffractive microscopy with isotropic resolution”. In: *Optica* 4.4 (2017), pp. 460–463. ISSN: 2334-2536. DOI: 10.1364/optica.4.000460 (cit. on pp. 46, 95).

[59] Ulugbek S. Kamilov et al. “Learning approach to optical tomography”. In: *Optica* 2.6 (2015), pp. 517–522. ISSN: 2334-2536. DOI: 10.1364/optica.2.000517. arXiv: 1502.01914 (cit. on pp. 49, 54).

[60] Matthieu Debailleul et al. “Holographic microscopy and diffractive microtomography of transparent samples”. In: *Meas. Sci. Technol.* 19.7 (2008), p. 074009. ISSN: 13616501. DOI: 10.1088/0957-0233/19/7/074009 (cit. on pp. 50, 54).

[61] Guillaume Maire et al. “Experimental demonstration of quantitative imaging beyond Abbe’s limit with optical diffraction tomography”. In: *Phys. Rev. Lett.* 102.21 (2009), pp. 1–4. ISSN: 00319007. DOI: 10.1103/PhysRevLett.102.213905 (cit. on pp. 49, 51).

[62] Charankumar Godavarthi et al. “Superresolution with full-polarized tomographic diffractive microscopy”. In: *J. Opt. Soc. Am. A* 32.2 (2015), p. 287. ISSN: 1084-7529. DOI: 10.1364/JOSAA.32.000287. URL: https://www.osapublishing.org/abstract.cfm?URI=josaa-32-2-287 (cit. on pp. 49, 51).

[63] A J OK-Devaney. “Inverse-scattering theory within the Rytov approximation”. In: *Opt. Lett.* 6.8 (1981), pp. 374–376. ISSN: 0146-9592. URL: http://www.ncbi.nlm.nih.gov/pubmed/19701437 (cit. on p. 49).

[64] Kyoohyun Kim et al. “ High-resolution three-dimensional imaging of red blood cells parasitized by Plasmodium falciparum and in situ hemozoin crystals using optical diffraction tomography ”. In: *J. Biomed. Opt.* 19.1 (2013), p. 011005. ISSN: 1083-3668. DOI: 10.1117/1.jbo.19.1.011005 (cit. on p. 49).

[65] Ulugbek S. Kamilov et al. “Optical Tomographic Image Reconstruction Based on Beam Propagation and Sparse Regularization”. In: *IEEE Trans. Comput. Imaging* 2.1 (2016), pp. 59–70. ISSN: 2333-9403. DOI: 10.1109/tci.2016.2519261 (cit. on p. 49).

[66] THANH-AN PHAM EMMANUEL SOUBIES, MICHAEL UNSER, and Ulugbek S. Kamilov. “Efficient inversion of multiple-scattering model for optical diffraction tomography”. In: *Opt. express* 25.18 (2017), p. 21786. ISSN: 2333-9403. DOI: 10.1109/tci.2017.2764461. arXiv: 1705.04281 (cit. on p. 49).

[67] Thanh-an Pham et al. “Three-Dimensional Optical Diffraction Tomography With Lippmann-Schwinger Model”. In: *IEEE Trans. Comput. Imaging* 6 (2020), pp. 727–738. ISSN: 2573-0436. DOI: 10.1109/tci.2020.2969070. arXiv: 1910.13844 (cit. on p. 49).

[68] Vinoth Balasubramani et al. “Holographic tomography: Techniques and biomedical applications [Invited]”. In: *Appl. Opt.* 60.10 (2021), B65–B80. ISSN: 21553165. DOI: 10.1364/AO.416902 (cit. on p. 49).

[69] Jonghee Yoon et al. “Identification of non-activated lymphocytes using three-dimensional refractive index tomography and machine learning”. In: *Sci. Rep.* 7.1 (2017), pp. 1–10. ISSN: 20452322. DOI: 10.1038/s41598-017-06311-y. URL: http://dx.doi.org/10.1038/s41598-017-06311-y (cit. on p. 49).

[70] Mirjam Schürmann et al. “Three-dimensional correlative single-cell imaging utilizing fluorescence and refractive index tomography”. In: *J. Biophotonics* 11.3 (2018), pp. 1–11. ISSN: 18640648. DOI: 10.1002/jbio.201700145 (cit. on p. 50).

[71] Kim et al. “Physicochemical Properties of Nucleoli in Live Cells Analyzed by Label-Free Optical Diffraction Tomography”. In: *Cells* 8.7 (2019), p. 699. ISSN: 2073-4409. DOI: 10.3390/cells8070699 (cit. on p. 50).

[72] Yann Cotte et al. “Marker-free phase nanoscopy”. In: *Nat. Photonics* 7.2 (2013), pp. 113–117. ISSN: 17494885. DOI: 10.1038/nphoton.2012.329. URL: http://dx.doi.org/10.1038/nphoton.2012.329 (cit. on p. 50).

[73] Mark Fauver et al. “Three-dimensional imaging of single isolated cell nuclei using optical projection tomography”. In: *Opt. Express* 13.11 (2005), pp. 4210–4223. ISSN: 1094-4087. DOI: 10.1364/opex.13.004210 (cit. on p. 51).

[74] *Nanolive*. https://www.nanolive.ch/. June 2021 (cit. on p. 51).

[75] *Tomocube Inc.* http://www.tomocube.com/. June 2021 (cit. on p. 51).

[76] Lisa Pollaro et al. “Stain-free 3D Nanoscopy of Living Cells”. In: *Opt. Photonik* 11.1 (2016), pp. 38–42. DOI: 10.1002/opph.201600008 (cit. on p. 51).

[77] Lisa Pollaro, Bastien Dalla Piazza, and Yann Cotte. “Digital Staining: Microscopy of Live Cells Without Invasive Chemicals”. In: *Micros. Today* 23.4 (2015), pp. 12–17. ISSN: 1551-9295. DOI: 10.1017/s1551929515000590 (cit. on p. 51).

[78] Juan Elezgaray, Lotfi Berguiga, and Françoise Argoul. “Plasmon-based tomographic microscopy”. In: *J. Opt. Soc. Am. A* 31.1 (2014), p. 155. ISSN: 1084-7529. DOI: 10.1364/josaa.31.000155 (cit. on p. 51).

[79] Ting Zhang et al. “Far-field diffraction microscopy at $\lambda/10$ resolution”. In: *Optica* 3.6 (2016), pp. 609–612. ISSN: 2334-2536. DOI: 10.1364/OPTICA.3.000609. URL: https://www.osapublishing.org/abstract.cfm?URI=optica-3-6-609 (cit. on pp. 51, 52).

[80] Sergey A. Alexandrov et al. “Synthetic aperture fourier holographic optical microscopy”. In: *Phys. Rev. Lett.* 97.16 (2006), pp. 1–4. ISSN: 00319007. DOI: 10.1103/PhysRevLett.97.168102 (cit. on p. 51).

[81] M. Sarmis et al. “High resolution reflection tomographic diffractive microscopy”. In: *J. Mod. Opt.* 57.9 (2010), pp. 740–745. ISSN: 09500340. DOI: 10.1080/09500341003624743 (cit. on p. 51).

[82] Philippe Robert et al. “Kinetics and mechanics of two-dimensional interactions between T cell receptors and different activating ligands”. In: *Biophys. J.* 102.2 (2012), pp. 248–257. ISSN: 00063495. DOI: 10.1016/j.bpj.2011.11.4018. URL: http://dx.doi.org/10.1016/j.bpj.2011.11.4018 (cit. on pp. 51, 67).

[83] Kyoohyun Kim et al. “Real-time visualization of 3-D dynamic microscopic objects using optical diffraction tomography”. In: *Opt. Express* 21.26 (2013), pp. 32269–32278. ISSN: 1094-4087. DOI: 10.1364/oe.21.032269 (cit. on p. 54).

[84] KyeoReh Lee et al. “Time-multiplexed structured illumination using a DMD for optical diffraction tomography”. In: *Opt. Lett.* 42.5 (2017), pp. 999–1002. ISSN: 0146-9592. DOI: 10.1364/ol.42.000999. arXiv: 1612.00044 (cit. on p. 54).

[85] Joowon Lim et al. “High-fidelity optical diffraction tomography of multiple scattering samples”. In: *Light Sci. Appl.* 8.1 (2019), pp. 1–12. ISSN: 2047-7538. DOI: 10.1038/s41377-019-0195-1. URL: http://dx.doi.org/10.1038/s41377-019-0195-1 (cit. on p. 54).

[86] Dennis Gabor. “A New Microscopic Principle”. In: *Nature* 161 (1948), pp. 777–778. ISSN: 00280836. DOI: 10.1038/161981a0 (cit. on p. 54).

[87] Markus Testorf and Adolf W. Lohmann. "Holography in phase space". In: *Appl. Opt.* 47.4 (2008). ISSN: 15394522. DOI: 10.1364/AO.47.000A70 (cit. on p. 54).

[88] Jorge Garcia-Sucerquia et al. "Digital in-line holographic microscopy". In: *Appl. Opt.* 45.5 (2006), pp. 836–850. ISSN: 15394522. DOI: 10.1364/AO.45.000836 (cit. on p. 54).

[89] Emmett N. Leith and Juris Upatnieks. "Reconstructed Wavefronts and Communication Theory*". In: *J. Opt. Soc. Am.* 52.10 (1962), pp. 1123–1130. ISSN: 0030-3941. DOI: 10.1364/josa.52.001123 (cit. on p. 54).

[90] Emmett N. Leith and Juris Upatnieks. "Wavefront Reconstruction with Continuous-Tone Objects*". In: *J. Opt. Soc. Am.* 53.12 (1963), pp. 1377–1381. ISSN: 0030-3941. DOI: 10.1364/josa.53.001377 (cit. on p. 54).

[91] Emmett N. Leith and Juris Upatnieks. "Wavefront Reconstruction with Diffused Illumination and Three-Dimensional Objects*". In: *J. Opt. Soc. Am.* 54.11 (1964), pp. 1295–1301. ISSN: 0030-3941. DOI: 10.1364/josa.54.001295 (cit. on p. 54).

[92] Christopher J. Mann et al. "High-resolution quantitative phase-contrast microscopy by digital holography". In: *Opt. Express* 13.22 (2005), pp. 8693–8698. ISSN: 1094-4087. DOI: 10.1364/opex.13.008693 (cit. on p. 54).

[93] Etienne Cuche, Pierre Marquet, and Christian Depeursinge. "Simultaneous amplitude-contrast and quantitative phase-contrast microscopy by numerical reconstruction of Fresnel off-axis holograms". In: *Appl. Opt.* 38.34 (1999), pp. 6994–7001. ISSN: 0003-6935. DOI: 10.1364/ao.38.006994 (cit. on p. 54).

[94] *NKT Photonics*. https://www.nktphotonics.com/lasers-fibers/product-category/supercontinuum-lasers/. Feb. 2021 (cit. on p. 57).

[95] *NKT Photonics*. https://www.nktphotonics.com/lasers-fibers/product/superk-varia-tunable-single-line-filter/. Feb. 2021 (cit. on p. 57).

[96] *Nikon*. https://www.microscope.healthcare.nikon.com/en_EU/selectors/objective-comparison/-5993. Feb. 2021 (cit. on p. 58).

[97] Frank Dubois, Luc Joannes, and Jean-Claude Legros. "Improved three-dimensional imaging with a digital holography microscope with a source of partial spatial coherence". In: *Appl. Opt.* 38.34 (1999), pp. 7085–7094. ISSN: 0003-6935. DOI: 10.1364/ao.38.007085 (cit. on p. 58).

[98] Ashley R. Carter et al. "Stabilization of an optical microscope to 0.1 nm in three dimensions". In: *Appl. Opt.* 46.3 (2007), pp. 421–427. ISSN: 15394522. DOI: 10.1364/AO.46.000421 (cit. on p. 58).

[99] Samira Khadir et al. "Quantitative model of the image of a radiating dipole through a microscope". In: *J. Opt. Soc. Am. A* 36.4 (2019), pp. 478–484. ISSN: 1084-7529. DOI: 10.1364/josaa.36.000478 (cit. on pp. 62, 72).

[100] Amaury Badon et al. “Smart optical coherence tomography for ultra-deep imaging through highly scattering media”. In: *Sci. Adv.* 2.11 (2016), e1600370. DOI: 10.1364/MATH.2017.MW3C.1 (cit. on p. 63).

[101] Balbino Alarcón, David Mestre, and Nuria Martínez-Martín. “The immunological synapse: A cause or consequence of T-cell receptor triggering?” In: *Immunology* 133.4 (2011), pp. 420–425. ISSN: 00192805. DOI: 10.1111/j.1365-2567.2011.03458.x (cit. on p. 67).

[102] Kenneth Murphy and Casey Weaver. *Janeway ' S immunobiology*. 9th. New York and London: Taylor & Francis Group, LLC, 2017. ISBN: 9780815345053 (cit. on p. 67).

[103] Edward. M Purcell and Carlton. R. Pennypacker. “Scattering and Absorption of Light by Nonspherical Dielectric Grains”. In: *J. Astorphysics* 186 (1973), pp. 705–714 (cit. on p. 68).

[104] M. A. Yurkin and A. G. Hoekstra. “The discrete dipole approximation: An overview and recent developments”. In: *J. Quant. Spectrosc. Radiat. Transf.* 106.1-3 (2007), pp. 558–589. ISSN: 00224073. DOI: 10.1016/j.jqsrt.2007.01.034 (cit. on p. 68).

[105] Patrick C Chaumet, Anne Sentenac, and Adel Rahmani. “Coupled dipole method for scatterers with large permittivity”. In: *Phys. Rev. E* 70.036606 (2004). DOI: 10.1103/PhysRevE.70.036606 (cit. on pp. 68, 70).

[106] A. Lakhtakia and G.W. Mulholland. “On two numerical techniques for light scattering by dielectric agglomerated structures”. In: *J. Res. Natl. Inst. Stand. Technol.* 98.6 (1993), p. 699. ISSN: 1044-677X. DOI: 10.6028/jres.098.046 (cit. on p. 68).

[107] F. Michael Kahnert. “Numerical methods in electromagnetic scattering theory”. In: *J. Quant. Spectrosc. Radiat. Transf.* 79-80 (2003), pp. 775–824. ISSN: 00224073. DOI: 10.1016/S0022-4073(02)00321-7 (cit. on p. 68).

[108] Patrick C. Chaumet and Adel Rahmani. “Efficient iterative solution of the discrete dipole approximation for magnetodielectric scatterers”. In: *Opt. Lett.* 34.7 (2009), p. 917. ISSN: 0146-9592. DOI: 10.1364/ol.34.000917 (cit. on p. 70).

[109] Guillaume Maire et al. “High-resolution tomographic diffractive microscopy in reflection configuration”. In: *J. Opt. Soc. Am. A* 30.10 (2013), pp. 2133–2139. ISSN: 1084-7529. DOI: 10.1364/JOSAA.30.002133. URL: https://www.osapublishing.org/abstract.cfm?URI=josaa-30-10-2133 (cit. on p. 72).

[110] Guillaume Maire et al. “Phase imaging and synthetic aperture super-resolution via total internal reflection microscopy”. In: *Opt. Lett., OL* 43.9 (2018), pp. 2173–2176. ISSN: 1539-4794. DOI: 10.1364/OL.43.002173. URL: https://www.osapublishing.org/ol/abstract.cfm?uri=ol-43-9-2173%7B%5C%%7D0Ahttp://dx.doi.org/10.1364/OL.43.002173 (cit. on p. 72).

[111] Md Rasedujjaman et al. “Three-dimensional imaging with reflection synthetic confocal microscopy”. In: *Opt. Lett.* 45.13 (2020), pp. 3721–3724. ISSN: 0146-9592. DOI: 10.1364/ol.397364 (cit. on pp. 72, 82, 101).

[112] Patrick C Chaumet et al. “Tutorial on IFDDA, an easy to use code for simulating the field scattered by 3D inhomogeneous objects in a stratified medium”. In: *J. Opt. Soc. Am. A* Accepted () (cit. on p. 73).

[113] *Bangslabs*. https://www.bangslabs.com/applications/test-assay-development/silica-microspheres. June 2020 (cit. on p. 76).

[114] Weiguo Cui and Susan M. Kaech. “Generation of effector CD8+ T cells and their conversion to memory T cells”. In: *Immunol. Rev.* 236.1 (2010), pp. 151–166. ISSN: 01052896. DOI: 10.1111/j.1600-065X.2010.00926.x (cit. on p. 81).

[115] Marie Pierre Valignat et al. “Lymphocytes can self-steer passively with wind vane uropods”. In: *Nat. Commun.* 5.5213 (2014). ISSN: 20411723. DOI: 10.1038/ncomms6213 (cit. on p. 82).

[116] *Sigma-aldrich*. https://www.sigmaaldrich.com/FR/en/life-science/sigma-aldrich. May 2021 (cit. on p. 84).

[117] Horst Feldmann. *Yeast: Molecular and Cell Biology*. 2nd. John Wiley & Sons, 2011 (cit. on p. 88).

[118] E Murdy et al. “Tomographic diffractive microscopy with isotropic resolution”. In: *Opt. Lett.* 35.11 (2010), pp. 1857–1860. ISSN: 2334-2536. DOI: 10.1364/optica.4.000460 (cit. on p. 95).

[119] Ludovic Foucault et al. “Versatile transmission / reflection tomographic diffractive microscopy approach”. In: *J. Opt. Soc. Am. A* 36.11 (2019), pp. 18–27 (cit. on p. 95).

Acronyms

APC
Antigen Presenting Cell. 32, 53

CARS
Coherent Anti-Stokes Raman Scattering. 1

CD
Cluster of Differentiation. 32, 47

CDM
Coupled Dipole Method. 33

CFI
Chomatic Aberration Free Infinity. 25

CRS
Coherent Raman Scattering. 1

cSMAC
Central Supramolecular Activation Cluster. 32

CT
Computed Tomography. 62

DAQ
Data Acquisition. 25

DDA
Discrete Dipole Approximation. 33–35, 62

DHM
Digital Holographic Microscopy. 1

DIC
Differential Interference Contrast. 11

dSMAC
Distal Supramolecular Activation Cluster. 32

FSM
Fast Steering Mirrors. 25

FT
Fourier Transform. 30

ICAM
Intercellular Adhesion Molecule. 45

IFDDA
Institute Fresnel-Discrete Dipole Approximation. 34, 35, 38

MTF
Modulation Transfer Function. 9, 10

NA
Numerical Aperture. v, 5, 23, 29, 36

OCT
Optical Coherence Tomography. 1, 29

ODT
Optical Diffraction Tomography. 11

OTF
Optical Transfer Function. vii, 9, 10, 15, 57, 58

PALM
Photo Activated Localization Microscopy. 1

PBS
Polarizing Beam Splitter. 23

PSF
Point Spread Function. iv, 8–10

pSMAC
Peripheral Supramolecular Activation Cluster. 32

PTF
Phase Transfer Function. 9

RI
Refractive Index. 17

ROI
Region of Interest. 25

SAR
Synthetic Aperture Radar. 15

sCMOS
Scientific Complementary Metal–Oxide–Semiconductor. 23

SIM
Structured Illumination Microscopy. 1

SLM
Spatial Light Modulator. 29

SMAC
Supramolecular Activation Cluster. 32

SRS
Stimulated Raman Scattering. 1

STED
STimulated Emission Depletion. 1

STORM
STochastic Optical Reconstruction Microscopy. 1

SyCM
Synthetic Confocal Microscopy. v–vii, 28–31, 38–40, 42, 43, 45–55, 58, 59, 62

TCR
T-cell Receptor. 32

TDM
Tomographic Diffractive Microscopy. iv–vii, 1, 2, 10, 11, 15–17, 19, 21–23, 25, 26, 28, 32, 35, 38, 39, 41, 42, 45, 47, 49, 53, 56–60, 62, 63

TIRF
Total Internal Reflection Fluorescence. 23, 25

TPM
Tomographic Phase Microscopy. 11

WD
Working Distance. 25

Articles

Letter Vol. 45, No. 13 / 1 July 2020 / Optics Letters 3721

Optics Letters

Three-dimensional imaging with reflection synthetic confocal microscopy

Md Rasedujjaman,[1] Kévin Affannoukoué,[1] Nicolas Garcia-Seyda,[2] Philippe Robert,[2] Hugues Giovannini,[1] Patrick C. Chaumet,[1] Olivier Theodoly,[2] Marie-Pierre Valignat,[2] Kamal Belkebir,[1] Anne Sentenac,[1] and Guillaume Maire[1,*]

[1]Aix Marseille Univ., CNRS, Centrale Marseille, Institut Fresnel, Marseille, France
[2]Laboratoire Adhesion et Inflammation, UMR INSERM 1067, UMR CNRS 7333, Aix-Marseille Université, Assistance Publique–Hôpitaux de Marseille, Case 937, 13288 Marseille Cedex 09, France
*Corresponding author: guillaume.maire@fresnel.fr

Received 12 May 2020; revised 29 May 2020; accepted 30 May 2020; posted 1 June 2020 (Doc. ID 397364); published 30 June 2020

Biomedical imaging lacks label-free microscopy techniques able to reconstruct the contour of biological cells in solution, in 3D and with high resolution, as required for the fast diagnosis of numerous diseases. Inspired by computational optical coherence tomography techniques, we present a tomographic diffractive microscope in reflection geometry used as a synthetic confocal microscope, compatible with this goal and validated with the 3D reconstruction of a human effector T lymphocyte.

https://doi.org/10.1364/OL.397364

Optical diffraction microscopy is an important tool in biological and biomedical imaging as it can be used on live cells and does not require staining. Yet, its poor axial resolution compared to the transverse one limits its interest for three-dimensional (3D) imaging. Now, an increasing number of applications would benefit from highly resolved 3D images of cells. In particular, the ability to observe the contour deformation of two interacting cells is of major interest as conformational changes can be the precursor of important biological phenomena [1].

Presently, the best-resolved marker-free 3D images of cells have been obtained using computational tomographic diffraction microscopy (TDM). It consists in reconstructing digitally the sample contrast from a stack of holograms obtained by interferometry under different illuminations (usually provided by a monochromatic collimated beam with varying angles) [2]. With such a data set, it is possible to form a 3D image with a resolution typically twice better than the standard microscopy techniques.

However, most of the studies in TDM have been performed with setups in transmission [2–8], which eases the volume reconstruction of the sample, but ends up with an axial resolution remaining at least 3 times worse than the transverse one. As a result, 3D conformation changes at cell membranes or interfaces in the wavelength range cannot be resolved.

To image the cell contour in 3D, the reflection geometry, which is highly sensitive to reflections from interfaces but not to slowly varying volume inhomogeneities, may be more appropriate [9]. In biomedical imaging, this geometry is mainly encountered in optical coherence tomography (OCT) [10], where the axial resolution, of at best one micron, remains insufficient to detect sub-micrometer axial deformation such as those encountered in lymphocyte activation [1]. In this context, reflection TDM, with its theoretical twice better resolution [11], seems an interesting solution.

So far, this computational approach has been applied to image thin structures deposited or etched on a reflective substrate [12–16], and to obtain 2D reflectance images of cells [17]. Combined with broadband illumination, it was also used to image reflective targets under a thick diffusive layer [18,19] and biological tissues at different depths [20,21], the digital reconstruction allowing an efficient removal of the multiple scattering and aberrations deteriorating the images of standard OCT.

In this Letter, we apply reflection TDM to the 3D imaging of cells. We show how a TDM setup can be used as a synthetic confocal microscope, and we take advantage of this computational approach to correct the focus aberrations induced by the use of a high numerical aperture oil-immersion objective (NA = 1.49). We compare reflection and transmission TDM on simulated data and provide experimental images of calibrated and biological samples.

TDM permits one to retrieve the 3D map of refractive index of a sample from the measurement of its scattered field under various illumination angles, using a numerical reconstruction procedure. A sensitivity to refractive index contrasts below 0.01 is typically attained [5–8]. Usually the field is measured in a plane conjugated to the sample, and then transferred to the far-field (Fourier space) with a 2D discrete Fourier transform to ease the data treatment steps.

The simplest link between the sample refractive index map and the scattered field is obtained under the Born approximation, typically valid for samples with weak refractive index contrast [2]. In this case, in the scalar approximation, the field scattered in far-field along wave vector $\mathbf{k}_s$ for an illumination plane wave along wave vector $\mathbf{k}_i$ is given by

$$E_s(\mathbf{k}_s, \mathbf{k}_i) \propto \tilde{\Delta\varepsilon}(\mathbf{k}_s - \mathbf{k}_i), \quad (1)$$

0146-9592/20/133721-04 Journal © 2020 Optical Society of America

3722 Vol. 45, No. 13 / 1 July 2020 / Optics Letters Letter

where $\tilde{\Delta}\varepsilon$ is the 3D Fourier transform of the permittivity contrast $\Delta\varepsilon$ of the sample (the permittivity being the refractive index squared). The reconstructed permittivity contrast $\Delta\varepsilon_{\text{rec}}$ at position $\mathbf{r}$ is thus directly obtained by a 3D discrete inverse Fourier transform,

$$\Delta\varepsilon_{\text{rec}}(\mathbf{r}) \propto \sum_{\mathbf{k}_i}\sum_{\mathbf{k}_s} E_s(\mathbf{k}_s, \mathbf{k}_i) e^{i(\mathbf{k}_s - \mathbf{k}_i)\cdot\mathbf{r}}. \tag{2}$$

Such a procedure is also known as synthetic aperture generation: each illumination angle permits one to access different Fourier components of the object, and combining them enlarges the accessible domain and improves the resolution.

Synthetic aperture generation is in fact equivalent to phase confocal imaging in which a beam is focused inside the sample and the scattered field is detected (with an interferometric setup, as in OCT) at the conjugated position, in the image plane, of the focus position [19].

This equivalence can be understood by recalling that scattering is a linear process, and the field scattered by a sample illuminated by a beam made of a sum of plane waves is equal to the sum of the scattered fields for each plane wave. Hence, assuming that the phase of all the incident plane waves is 0 at the focal point of the objective, corresponding to the origin of the coordinate system $\mathbf{r} = \mathbf{0}$,

$$\tilde{e}(\mathbf{k}_s, \mathbf{r}) = \sum_{\mathbf{k}_i} E_s(\mathbf{k}_s, \mathbf{k}_i) e^{-i\mathbf{k}_i\cdot\mathbf{r}} \tag{3}$$

represents the far-field scattered in the $\mathbf{k}_s$ direction obtained when the sample is illuminated by a beam made of a sum of plane waves interfering constructively at $\mathbf{r}$. Then,

$$E(\mathbf{r}) = \sum_{\mathbf{k}_s} \tilde{e}(\mathbf{k}_s, \mathbf{r}) e^{i\mathbf{k}_s\cdot\mathbf{r}} \tag{4}$$

represents the field at $\mathbf{r}$ in the image domain of the microscope (with magnification 1) obtained from the far-field $\tilde{e}$ [22]. It corresponds to the complex field that would be measured at the center of the pinhole of a confocal microscope. Introducing Eq. (3) in Eq. (4), one observes that the complex field E is proportional to $\Delta\varepsilon_{\text{rec}}$ under Born approximation,

$$E(\mathbf{r}) = \sum_{\mathbf{k}_i}\sum_{\mathbf{k}_s} E_s(\mathbf{k}_s, \mathbf{k}_i) e^{i(\mathbf{k}_s - \mathbf{k}_i)\cdot\mathbf{r}} \propto \Delta\varepsilon_{\text{rec}}(\mathbf{r}). \tag{5}$$

Works in optical imaging based on synthetic aperture usually calculate the real and imaginary parts of Eq. (5) to obtain the refractive index and absorption maps of their samples. In fact, calculating its intensity and phase is also meaningful, as they represent the squared modulus and the argument of the reflectance (or transmittance) of a focused beam scanned through the sample. We call this approach synthetic confocal microscopy (SyCM), which we consider more general than synthetic aperture generation, since optimized phase or amplitude terms can be inserted in Eqs. (3) and (4) to reshape numerically the illumination and detection of the microscope, as is done with spatial light modulators in adaptive optics, and proposed in smart-OCT [19]. In particular, this computational approach allows an easy correction of the focus aberrations induced by the index mismatch at the glass–water interface of our experimental configuration, where an oil-immersion microscope objective of NA = 1.49 is used for maximizing the axial and transverse resolution. This procedure will be detailed later with the phase normalization of the data set.

To show the interest of reflection SyCM, we first apply it to synthetic 3D objects: two portions of spheres of refractive index 1.38 in water. The axial cuts of the samples are depicted in Figs. 1(a) and 1(b). In Fig. 1(a) the top sphere touches the bottom one, whereas in Fig. 1(b), it enters the bottom one. These two configurations illustrate, with simple geometries, a T cell (top sphere) interacting with an antigen presenting cell (bottom sphere): in Fig. 1(a), the T cell is not activated, whereas in Fig. 1(b), it is activated [1].

A homemade program based on the coupled dipole method (CDM) [23] estimated the scattered fields $E_s(\mathbf{k}_s, \mathbf{k}_i)$ of these two configurations by solving rigorously Maxwell equations. 121 linearly polarized plane waves were used for the illumination, with maximal polar angle of 55°, and a numerical aperture of 1.2 in water was assumed for detection. We chose an imaging configuration in which the incident and scattered transverse wave vectors laid on a regular two-dimensional (2D) grid. Calculations were performed in transmission and reflection.

The 3D intensity $|E(\mathbf{r})|^2$, Eq. (5), was estimated plane by plane using 2D inverse Fourier transforms, as in [24]. In Figs. 1(c) and 1(d), the reconstructions obtained in transmission show no difference between the two cell–cell configurations. In contrast, the contour of the objects can be retrieved with high fidelity with data in reflection [Figs. 1(e) and 1(f)]. This highlights the great potential of reflection SyCM to probe the surfaces and interfaces of biological cells.

We built a TDM setup in reflection geometry sketched in Fig. 2. Detailed description can be found elsewhere [15].

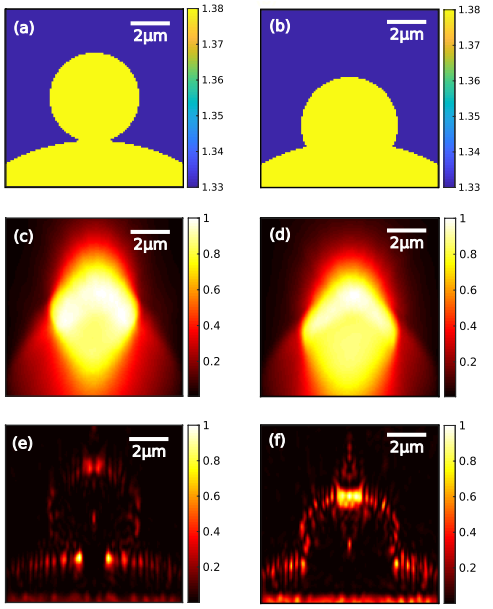

Fig. 1. (a) and (b) Axial cuts of two configurations mimicking two interacting cells (refractive index in colorbar). (c) and (d) Respective SyCM intensity reconstructions in transmission geometry; (e) and (f) in reflection geometry. Reconstructions are normalized to 1 at their maximal value.

Letter Vol. 45, No. 13 / 1 July 2020 / *Optics Letters* 3723

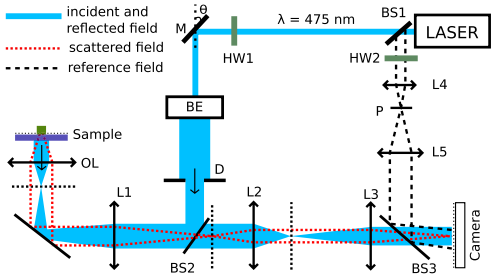

Fig. 2. Reflection TDM setup: M, rotating mirror; BE, beam expander; D, diaphragm; OL, objective lens; L_1, tube lens; L_{2-5}, lenses; BS_{1-3}, beam splitters; HW_{1-2}, half-wave plates; P, pinhole.

The light source is a supercontinuum laser (NKT Photonics SuperK Extreme EXW-12) filtered at 475 nm with a spectral width of 6 nm thanks to a variable bandpass filter (NKT Photonics SuperK Varia). The laser beam is linearly polarized, and its illumination angle is controlled by a fast steering mirror (M, Newport FSM–300). The scattered field is collected by an oil-immersion objective (Nikon-TIRF 100X, NA = 1.49) and imaged on a sCMOS camera (Andor Zyla) with a global magnification of about 200.

For samples like biological cells in water, the backscattered signal is very weak. Depending on the illumination angle, parasitic reflections from the tube lens and the objective can be of the same order as the useful signal. The use of a low coherence source for the off-axis holography permits us to wash away these parasitic reflections: here, the coherence length is about 40 µm, much shorter than the distance between the sample and the parasitic reflective surfaces.

All the reconstruction procedures in TDM consider that the different incident plane waves used to illuminate the sample have the same null phase at the chosen origin of the coordinate system. This origin is usually taken at the focal point of the objective. But the mechanical and thermal drifts between successive illuminations introduce random phase shifts to each incident plane wave. A phase normalization procedure is therefore crucial to correct the data so that the phases of each illumination plane wave can be considered null at the origin. Then, forming a synthetic beam that focuses at any position is simple algebra.

This normalization is based on the complex amplitude of the far-field in the specular reflected direction for each hologram. It corresponds to the reflection of the incident beam at the glass–water interface and appears as a Dirac-like peak in the Fourier plane of the microscope. We assume that this reflection is not affected by the sample. The whole signal is corrected so that the experimental specular reflection corresponds to its theoretical value. Contrarily to the transmission coefficient, which is generally always close to one, the theoretical reflection coefficient can be easily calculated only if the glass–water interface is placed at the object focal plane (conjugated to the camera plane): it will then be equal to the Fresnel formula. However, it is seldom the case, especially if the sample is thick. In this case, the optical path of the specular reflection toward the camera, and therefore the phase of the theoretical reflection coefficient, will strongly depend on the unknown distance d between these two planes

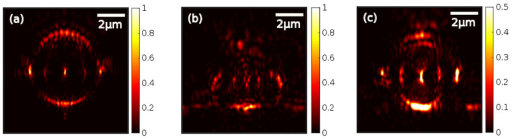

Fig. 3. (a) Axial cuts of SyCM intensity reconstructions for a glass bead immersed in water: (a) simulated data, (b) experimental data without the correct phase normalization, (c) experimental data with the correct phase normalization. Colorscale has been readjusted on (c) for visualization purpose.

and on the illumination angle. To avoid this issue, we numerically propagate the fields to reach the glass–water interface. d is estimated from a 3D image that is insensitive to illumination phase errors and corresponds to a 3D incoherent bright-field image,

$$I(\mathbf{r}) = \sum_{\mathbf{k}_i} \left| \sum_{\mathbf{k}_s} E_s(\mathbf{k}_s, \mathbf{k}_i) e^{i\mathbf{k}_s \cdot \mathbf{r}} \right|^2 . \quad (6)$$

Even though less resolved than the synthetic confocal reconstruction, the 3D brightfield image I permits to detect the interface with enough accuracy for the phase normalization to be satisfactory.

SyCM was tested experimentally on a calibrated sample made of a glass bead of diameter 5 µm and refractive index 1.46 (Bangs laboratories), deposited on a glass lamella and immersed in water. Figure 3 shows reconstructions obtained from simulated [Fig. 3(a)] and experimental [Fig. 3(c)] data. We observe that they are very similar, and the slight differences can be attributed to discrepancies between the optical transfer function of the objective and the ideal one assumed for the simulations. Figure 3(b) shows the distorted reconstruction obtained when the phase normalization is done without propagating the fields to the glass–water interface. It points out the importance of this procedure, even for small values of d (which, in this case, was estimated to 1.1 µm).

Note that the reconstructions are performed in dark-field mode, by filtering out the specular reflection in the Fourier space for each hologram. As a result, the glass–water interface cannot be seen. This is an important advantage over classical confocal microscopy, as this interface produces a strong signal that masks that scattered by the sample and corrupts the 3D reconstruction. Another advantage is that the 2D angular scans in SyCM (121 illumination angles here) can be performed in a quicker way than the 3D position scans of standard confocal microscopy (typically more than 10^5 positions required).

Next, we tested the ability of SyCM to image a biological cell. We considered human effector T lymphocytes, deposited on a glass lamella coated with adhesion molecules ICAM-1, and then fixed by a treatment with paraformaldehyde at 4%. Effector T cells migrate on ICAM-1 substrates with a strongly polarized shape. Their central and front parts are strongly adherent and spread, while their rear part forms a partially detached tail, called uropod [25].

Figure 4 shows the 3D reconstruction obtained on one of such T cells: the central body on the right and the uropod on the left can be clearly identified. The central body appears filled with numerous inhomogeneities in comparison with the uropod.

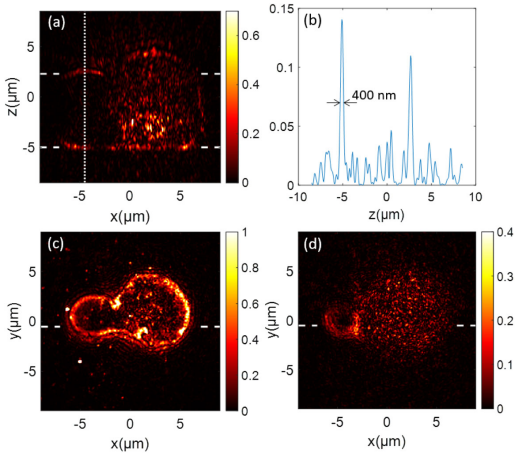

Fig. 4. Reflection SyCM intensity reconstruction of a human effector T lymphocyte: (a) axial cut along dashed white segments of (c); (b) intensity profile along vertical dotted white line of (a); (c) and (d) transverse cuts along white dashed segments of (a) at $z = -5$ μm (glass interface position), and at $z = 2.3$ μm, respectively. Colorscale has been readjusted on (a) and (d) for visualization purpose.

This can be explained by the fact that the central body contains the nucleus where highly compacted DNA is bound to produce refractive index changes stronger than anywhere else in the cell. The bottom and top membranes of the cell are also clearly retrieved on the axial cut Fig. 4(a), showing the high sectioning capability of reflection SyCM. An axial resolution about 400 nm can be evaluated from the full width at half-maximum of the signal profile Fig. 4(b) when crossing these membranes, close to the effective wavelength of illumination of 357 nm in water.

In conclusion, we have shown that tomographic diffractive microscopy in reflection can be used to provide 3D images of cells that are complementary to that obtained in the more classical transmission configuration. Our TDM setup was used as a synthetic confocal microscope, in which the incident plane waves are combined numerically to form a synthetic focused beam scanning the sample. This computational approach permitted to correct easily the focus aberrations induced by the index mismatch between the oil objective (NA = 1.49) and the mounting medium (water). It was able to image the top and bottom membrane of cells with an axial resolution about 400 nm. This result is promising for biomedical applications where contours of biological cells have to be monitored, like for T cells activation detection. As a next step, the quantitative iterative reconstruction scheme used in [15] will be adapted to cells to retrieve their permittivity maps.

Funding. H2020 Marie Skłodowska-Curie Actions (713750); Regional Council of Provence-Alpes-Côte d'Azur; Aix-Marseille University (ANR-11-IDEX-0001-02).

Disclosures. The authors declare no conflicts of interest.

REFERENCES

1. A. Grakoui, S. K. Bromley, C. Sumen, M. M. Davis, A. S. Shaw, P. M. Allen, and M. L. Dustin, Science **285**, 221 (1999).
2. V. Lauer, J. Microsc. **205**, 165 (2002).
3. M. Debailleul, B. Simon, V. Georges, O. Haeberlé, and V. Lauer, Meas. Sci. Technol. **19**, 074009 (2008).
4. M. Debailleul, V. Georges, B. Simon, R. Morin, and O. Haeberlé, Opt. Lett. **34**, 79 (2009).
5. K. Kim, K. S. Kim, H. Park, J. C. Ye, and Y. Park, Opt. Express **21**, 32269 (2013).
6. U. S. Kamilov, I. N. Papadopoulos, M. H. Shoreh, A. Goy, C. Vonesch, M. Unser, and D. Psaltis, Optica **2**, 517 (2015).
7. K. Lee, K. Kim, G. Kim, S. Shin, and Y. Park, Opt. Lett. **42**, 999 (2017).
8. J. Lim, A. B. Ayoub, E. E. Antoine, and D. Psaltis, Light Sci. Appl. **8**, 82 (2019).
9. A. Sentenac and J. Mertz, J. Opt. Soc. Am. A **35**, 748 (2018).
10. A. Dubois, K. Grieve, G. Moneron, R. Lecaque, L. Vabre, and C. Boccara, Appl. Opt. **43**, 2874 (2004).
11. O. Haeberlé, K. Belkebir, H. Giovaninni, and A. Sentenac, J. Mod. Opt. **57**, 686 (2010).
12. S. A. Alexandrov, T. R. Hillman, T. Gutzler, and D. D. Sampson, Phys. Rev. Lett. **97**, 168102 (2006).
13. V. Mico, Z. Zalevsky, P. García-Martínez, and J. García, J. Opt. Soc. Am. A **23**, 3162 (2006).
14. G. Maire, Y. Ruan, T. Zhang, P. C. Chaumet, H. Giovannini, D. Sentenac, A. Talneau, K. Belkebir, and A. Sentenac, J. Opt. Soc. Am. A **30**, 2133 (2013).
15. C. Godavarthi, T. Zhang, G. Maire, P. C. Chaumet, H. Giovannini, A. Talneau, K. Belkebir, and A. Sentenac, J. Opt. Soc. Am. A **32**, 287 (2015).
16. H. Liu, J. Bailleul, B. Simon, M. Debailleul, B. Colicchio, and O. Haeberlé, Appl. Opt. **53**, 748 (2014).
17. T. Gutzler, T. R. Hillman, S. A. Alexandrov, and D. D. Sampson, Opt. Lett. **35**, 1136 (2010).
18. S. Kang, S. Jeong, W. Choi, H. Ko, T. D. Yang, J. H. Joo, J.-S. Lee, Y.-S. Lim, Q.-H. Park, and W. Choi, Nat. Photonics **9**, 253 (2015).
19. A. Badon, D. Li, G. Lerosey, A. C. Boccara, M. Fink, and A. Aubry, Sci. Adv. **2**, e1600370 (2016).
20. Y.-Z. Liu, F. A. South, Y. Xu, P. S. Carney, and S. A. Boppart, Biomed. Opt. Express **8**, 1549 (2017).
21. M. Kim, Y. Jo, J. H. Hong, S. Kim, S. Yoon, K.-D. Song, S. Kang, B. Lee, G. H. Kim, H.-C. Park, and W. Choi, Nat. Commun. **10**, 3152 (2019).
22. S. Khadir, P. C. Chaumet, G. Baffou, and A. Sentenac, J. Opt. Soc. Am. A **36**, 478 (2019).
23. P. C. Chaumet, A. Sentenac, and A. Rahmani, Phys. Rev. E **70**, 036606 (2004).
24. P. C. Chaumet, A. Sentenac, and T. Zhang, J. Quant. Spectrosc. Radiat. Transfer **243**, 106816 (2020).
25. M.-P. Valignat, P. Nègre, S. Cadra, A. C. Lellouch, F. Gallet, S. Hénon, and O. Theodoly, Nat. Commun. **5**, 5213 (2014).